Additive Manufacturing on the Smallest Scale: Aligned Stacking of Nanopatterned 2D Materials

Dissertation
der Mathematisch-Naturwissenschaftlichen Fakultät
der Eberhard Karls Universität Tübingen
zur Erlangung des Grades eines
Doktors der Naturwissenschaften
(Dr. rer. nat.)

vorgelegt von
Jonas Haas
aus Schwäbisch Gmünd

Tübingen
2024

Gedruckt mit Genehmigung der Mathematisch-Naturwissenschaftlichen Fakultät der Eberhard Karls Universität Tübingen.

Tag der mündlichen Prüfung:	06.09.2024
Dekan:	Prof. Dr. Thilo Stehle
1. Berichterstatter	Prof. Dr. Jannik C. Meyer
2. Berichterstatter	Prof. Dr. Reinhold Kleiner

ABSTRACT

The family of two-dimensional (2D) materials is exciting not only because of their unique atomically thin layer structure, but also due to the remarkable properties found within the family, such as extremely high conductivity and strength and outstanding optoelectronic properties. In addition, the layers can be assembled into artificial composites, creating what are known as van der Waals heterostructures. This offers the ability to combine any 2D materials from the wide variety of layered materials and to specify the layer order as well as orientation. As a result, van der Waals heterostructures exhibit diverse properties such as superconductivity in bilayer graphene at a specific rotation angle or the twist angle dependent photoluminescence of transition metal dichalcogenide bilayers.

Modifications of the individual layers extend the possibilities even further. For example, doping or patterning at the nanometer level can affect the properties of 2D materials. Notably, electron microscopy is a powerful tool to introduce modifications on a very small scale, thus enabling techniques such as band-gap engineering.

However, current techniques for creating heterostructures can not be used in combination with nanopatterning of individual layers at high resolution. In particular, mechanical stacking methods using optical microscopes for assembling layers are well established. Restricted by the optical diffraction limit, precise stacking of patterned individual layers is not possible with these approaches.

In this thesis, a novel method for the assembly of nanopatterned, free-standing 2D materials is developed. The stacking is performed in a scanning electron microscope, allowing high-resolution observation during the process and precise alignment of the layers using piezo manipulators. The technique enables van der Waals heterostructures to be fabricated with a layer alignment precision of a few nanometers. Different patterning techniques for freestanding 2D materials are investigated and applied for heterostructure assembly.

The novel method allows for the creation of small three-dimensional structures. Nanometer sized holographic phase plates for electrons are fabricated, capable of generating diverse electron probes with controlled amplitudes and phases by

specifying the patterns introduced into the materials. Due to the small size of the phase plates, the resulting electron probe is also in the nanometer range without any additional electron optics.

The method developed for the precise stacking of nanopatterned, freestanding 2D materials enables the creation of structures in an additive manufacturing process at the nanometer scale, providing a new approach to nanofabrication techniques. The ability to modify each layer allows tailoring of the properties for potential applications such as solid-state nanopores or optoelectronic devices.

ZUSAMMENFASSUNG

Die Familie der zweidimensionalen (2D) Materialien ist nicht nur aufgrund ihrer einzigartigen, atomar dünnen Struktur von großem Interesse, sondern auch aufgrund der außergewöhnlichen Eigenschaften, die innerhalb der Familie zu finden sind. Dazu zählen insbesondere die extrem hohe Leitfähigkeit und Festigkeit sowie außergewöhnliche optische Eigenschaften der verschiedenen Materialien. Darüber hinaus können aus den einzelnen atomar dünnen Lagen Schichtmaterialien hergestellt werden, die so in der Natur nicht zu finden sind. Die unterschiedlichen 2D Materialien können in beliebiger Reihenfolge und Ausrichtung aufeinander gestapelt werden, wodurch eine nahezu unzählige Vielfalt an möglichen Kombinationen sogenannter van der Waals Heterostrukturen entsteht. Diese Heterostrukturen besitzen unterschiedlichste Eigenschaften, wie zum Beispiel Supraleitung in um einen bestimmten Winkel verdrehten Graphen-Bilagen oder die vom Ausrichtungswinkel abhängige Photoluminezenz zweilagiger Übergangsmetall-Dichalkogeniden.

Durch Modifikation der einzelnen Schichten eröffnen sich noch weitere Möglichkeiten. Mithilfe von Dotierung oder Strukturierung auf der Nanometer Skala lassen sich die Eigenschaften der 2D Materialien beeinflussen. Dabei stellt insbesondere die Elektronenmikroskopie ein wichtiges Hilfsmittel dar, um Modifikationen auf einer sehr kleinen Skala vorzunehmen und so beispielsweise eine gezielte Änderung der Bandlücke zu ermöglichen.

Die derzeitigen Methoden zur Herstellung von Heterostrukturen können jedoch nicht mit hochauflösender Nanostrukturierung einzelner Schichten kombiniert werden. Mechanische Stapelmethoden basieren auf der Verwendung eines Lichtmikroskops und sind daher aufgrund des Beugungslimits in ihrer Auflösung begrenzt. Eine präzise Ausrichtung von eingebrachten Nanostrukturen in den verschiedenen Lagen ist somit nicht möglich.

In dieser Dissertation wurde eine neue Methode zur Herstellung von van der Waals Heterostrukturen aus nanostrukturierten, freistehenden 2D Materialien entwickelt, die durch die Verwendung eines Elektronenmikroskops die Beobachtung der strukturierten Lagen erlaubt und so eine sinnvolle Kombination aus Nanostrukturierung und van der Waals Heterostrukturen ermöglicht. Mithilfe von Piezomanipulatoren lässt sich die Ausrichtung der einzelnen Lagen während des Stapelprozesses kontrollieren. Die mit dieser Methode hergestellten Strukturen weisen eine Genauigkeit von wenigen Nanometern auf. Verschiedene Techniken zur Nanostrukturierung von freistehenden 2D Materialien wurden untersucht und für die Herstellung von Heterostrukturen verwendet.

Die Methode erlaubt die Fabrikation von dreidimensionalen Strukturen auf der Nanometer Skala. Im Rahmen der Dissertation wurden damit holografische Phasenplatten für Elektronen hergestellt, die zur Erzeugung von fokussierten Elektronenstrahlen verwendet wurden. Durch Variation der eingebrachten Strukturen sowie der Dicke der resultierenden dreidimensionalen Form lassen sich verschiedenste Strahlformen mit kontrollierter Amplitude und Phase realisieren. Die geringe Größe der Phasenplatten erlaubt eine Fokussierung des Elektronenstrahls auf wenige Nanometer, ohne dass weitere Elektronenoptiken erforderlich sind.

Die für die präzise Stapelung von nanostrukturierten, freistehenden 2D Materialien entwickelte Methode ermöglicht die Herstellung von Strukturen im Nanometerbereich im Rahmen eines additiven Fertigungsprozesses und stellt damit einen neuartigen Ansatz im Bereich der Nanofabrikation dar. Die Eigenschaften des resultierenden Materials können durch Modifikation jeder einzelnen Schicht für potenzielle Anwendungen wie beispielsweise Festkörper-Nanoporen oder optoelektronische Geräte angepasst werden.

Contents

Chapter 1

Introduction

> *What could we do with layered structures with just the right layers? What would the properties of materials be if we could really arrange the atoms the way we want them? They would be very interesting to investigate theoretically. I can't see exactly what would happen, but I can hardly doubt that when we have some control of the arrangement of things on a small scale we will get an enormously greater range of possible properties that substances can have, and of different things that we can do.*

Richard Feynman, There's Plenty of Room at the Bottom, 1959

Scientific progress and breakthroughs are often based on previous theoretical considerations. Throughout the history of science, however, experiments and emerging technologies have revealed novelties that were previously considered to be impossible by existing opinions and theories.[1] At the time of Richard Feynman's lecture, the stability of single-layered, crystalline arranged atoms was not imaginable.

For many years, theoretical research led to the conclusion that these 2D materials are thermodynamically unstable and thus could not exist.[2–4] But then in 2003, defying the theoretical predictions, Andre Geim and Konstantin Novoselov succeeded in creating a thin film of graphite which could be identified as a single-atomic layer. The monolayer material attracted great attention due to its outstanding, and at the same time astonishing, electrical properties.[5–7] Already almost 20 years before, Hanns-Peter Boehm introduced the term *graphene* for this single-atomic carbon layer.[8] While Geim and Novoselov received the Nobel Prize in Physics in 2010[9] for their findings on graphene, there were many preceding experimental approaches on producing extremely thin carbon films and occasionally also monolayers.[10–15] However, they did not attract comparable attention as they either lacked a clear evidence of the single layer nature or reported only the observation itself. Geim and Novoselov were the first to surprise the scientific community with measurements of the unique electronic properties of graphene.[16] With the help of electron microscopy, the structural properties of graphene have been studied and an explanation for the stability of the material has been found: While the predicted instability for strictly flat 2D materials is valid, warping of graphene in the third dimension has been observed, explaining the intrinsic stability of 2D materials.[17]

The discovery of graphene triggered the search and investigation of other atomic 2D-crystals.[18] Calculations show that there are more than one thousand possible stable 2D materials with different electronic, optical and magnetic properties.[19] The 3D bulk structure of 2D materials consists of separated, stacked layers. While there are strong, covalent bonds between the atoms in the plane, only weak van der Waals interactions between adjacent layers occur.[20] For this reason, 2D materials can be created from their 3D form by simply disassembling the layer stack. Some of the most important and studied materials include hexagonal boron nitride (hBN)[21–23] and the group of different transition metal dichalcogenides, for example the semiconducting molybdenum disulfide (MoS_2)[24–26]. With a better understanding of the fundamental properties of the materials, the exploration of applications for 2D materials started. These range from electronics (e.g. integrated circuits for logic applications[27], high-speed electronics[28], field-effect transistors[25,29]) and optics (e.g. ultra-fast photodetectors[30], optical modulators[31]) to biological applications (e.g. biosensors[32] and DNA-sequencing[33]).

The idea of creating heterostructures with 2D materials emerged as another exciting breakthrough in the field of low-dimensional materials. The forces existing between the sheets in the naturally occurring 3D bulk material enable the stacking of various types of 2D layers on top of each other. In the resulting heterostructure, these layers are also held together by van der Waals forces. Hence, the family of 2D materials serves as a diverse library for stacking, a technique commonly referred to "Lego on the atomic level". Van der Waals heterostructures are artificial materials that do not naturally occur in this specific form.[34,35]

The newly created heterostructures are exciting and promising for research, especially with regard to possible applications. For example, bilayer graphene when orientated at the magic angle of about 1.1° exhibits superconducting properties.[36] In addition, the charge carrier mobility of graphene is significantly increased by stacking on hBN or by sandwiching it between two layers of hBN, compared to the use of silicon dioxide as substrate.[37–39] Thereby, the mobility reaches the theoretical phonon-scattering limit in these van der Waals heterostructures.[40]

The concept of van der Waals heterostructures together with the broad range of properties within the pool of 2D materials allows the fabrication of entire (opto-) electronic devices. The functional components can be completely created from different 2D materials. Only the substrate, supporting the atomic membranes, and large leads must be prepared from bulk or classic thin-film materials. Therefore, they are considered to be very promising for the semiconductor industry in terms of the demand for miniaturization.

Miniaturization and improved structural resolution is also an essential issue for new methods in 3D printing and additive manufacturing in general. While the structure sizes in typical 3D printers are in the order of several 100 µm, new techniques as for example microscale selective laser sintering (µ-SLS) processes can achieve resolutions down to 5 µm.[41] Two-photon polymerization even enables the fabrication of structures down to 100 nm.[42] Nevertheless, 3D printing on the scale of single-digit nanometer or even on the atomic level is still not possible with current techniques.

Following the definition of additive manufacturing, i.e. the process of producing a 3D structure by applying layer by layer, the fabrication of van der Waals heterostructures can also be classified into this category. The ultimate resolution in the Z-direction is already achieved as the individual layers (i.e. the 2D materials) are only one or few-atoms thick. In contrast, the x-y-resolution is significantly worse due to the expansion and continuity of the layers in these dimensions. Although, in-plane features could be introduced by patterning or manipulating the 2D materials. Electron microscopy allows modifying materials on the nanometer and even atomic scale.[43–48] Thus, patterning and manipulating enable high-resolution in the x-y-dimensions. However, this alone is not sufficient to achieve high-resolution in three dimensions: The introduced 2D patterns must be aligned to each other with similar precision during the assembly of the van der Waals heterostructures. In this respect, current methods for the fabrication of heterostructures have not yet sufficient precision in the control of the in-plane alignment of the layers. Growth methods have no control at all in this respect, except potentially through pre-patterning. Mechanical assembly methods use optical microscopes to control the alignment: So-called deterministic placement methods allow the assembly with approximately 1 µm precision. Nevertheless, these methods are limited due to diffraction and thus are far from being sufficient to assemble the individual layers with a precision in the low nanometer or even atomic range.

In order to make use of the high-resolution features that can be introduced in low-dimensional materials, the assembly of van der Waals heterostructures needs to be improved. Within this thesis, I developed a method that allows aligned stacking of nanostructured 2D materials with nanometer precision. Instead of using an optical microscope, the assembly is done in an scanning electron microscope (SEM). Due to the superior resolution of electron microscopes, it enables improved observation of the alignment of introduced features during the stacking. With the aid of a piezo manipulator, which operates similarly to a hand in the microscope, the layers can be precisely aligned with each other.

Combining nanopatterning, which can be used to tailor the properties of 2D materials, and precise stacking of these customized layers into heterostructures allows the creation of layered materials with exciting and novel properties. High-resolution electron beam patterning of transition metal dichalcogenide monolayers is investigated in this thesis with respect to potential band-gap engineering, which provides a route to optimize materials for functional electronic and optoelectronic devices. Furthermore, the fabrication technique developed is capable of creating nanometer scaled 3D structures that can be functional simply by virtue of their shape. The extremely small size of the resulting 3D shape is utilized to fabricate holographic phase plates by patterning and stacking 2D materials and thin graphite membranes in order to transform an electron wave into a desired nanometer sized probe shape.

In Richard Feynman's lecture in 1959 “There's Plenty of Room at the Bottom”, often considered as the birth of nanotechnology, he envisioned creating materials from atomically thin layers to achieve miniaturization, for example to improve computers. With this new method to assemble nanopatterned 2D materials, the prospect of additive manufacturing at the atomic scale has come a step closer to reality. Already as it stands, the new technique may enable novel nano-electronic, nano-optical or nano-fluidic devices and other tiny structures, which remain to be explored in follow-up projects.

Chapter 2

Background and Theory

This chapter introduces the theoretical background and the state of the art of both the materials and the methods used in this work. First, several two-dimensional materials (2D materials) are considered in more detail, followed by the history and fabrication methods of van der Waals heterostructures (vdWHs). Then, some applications of nanopatterned 2D materials and vdWHs are presented. Afterwards, an introduction to electron microscopy is given, which is the main tool used in this thesis. This includes a brief history and an explanation of the different microscopy techniques. Beam damage mechanisms are introduced and their potential for nanopatterning is described.

2.1 Two – Dimensional Materials

The properties of materials are not only determined by their chemical composition. Especially when entering the nanometer regime, typically below 100 nm, the size plays an important role as well. The use of colloidal gold in the ancient times is a famous example. Without knowing the physical background, gold particles of various sizes were used as colouring agents for glass and ceramics.[49,50]

The 3D bulk structure of a material can be confined in the spatial directions by reducing the size along certain axis.[51] For carbon, allotropes with all dimensionalities ranging from three-dimensional (3D) to zero-dimensional (0D) are known and shown in Fig. 2.1. Two-dimensional materials are restricted in their height (i.e. the z-dimension) and therefore represent thin sheets of the 3D bulk structure. However, the existence of the two-dimensional (2D) form requires the bulk to be

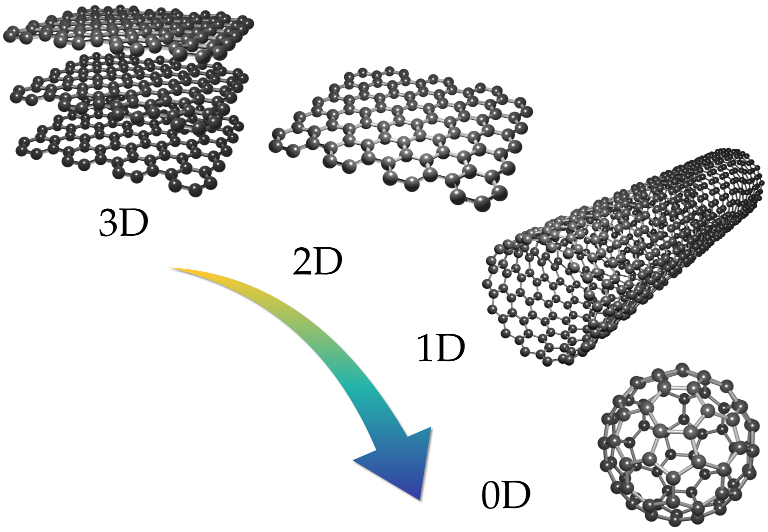

Figure 2.1: Carbon allotropes with different dimensionalities: (3D) graphite, (2D) graphene, (1D) carbon nanotube and (0D) fullerene.

a layered crystal: The atoms in each layer of the bulk material are strongly covalently bonded, while only weak van der Waals forces exist between the layers. In a theoretical study, researchers searched databases for layered materials and found more than 5500 layered compounds.[19] Density-function theory calculations suggested that more than 1000 of these should be easy to exfoliate and are therefore likely to be produced. Among this large family of 2D materials, the entire range of electronic properties is represented, with insulators, semiconductors, metals and even superconductors, as well as various magnetic properties.

In case of carbon, the two-dimensional form consists of only a single layer of atoms. This allotrope is known as graphene and will be described in more detail below.

Graphene

Graphene consists of a single layer of carbon atoms arranged in a hexagonal, honeycomb lattice.[52] Each atom is connected to its three nearest neighbours forming an atomically thin plane of sp^2-bonded carbon atoms with a molecular bond length of 0.142 nm.[53] The structure of graphene is shown schematically in Fig. 2.2 A. Historically, graphene was thought to be perfectly flat and therefore thermodynamically unstable. However, electron microscopy revealed warping of the atomically thin membrane, which helped to explain the existence of graphene and 2D materials in general.[17] The calculated *"3D"* structure of graphene is illustrated in Fig. 2.2 C.

Among the family of 2D materials, graphene has served as the pioneer: It was the first to be fabricated and is still the most studied material in this class to this date. Apart from being a new material, one main reason for the huge effort on studying graphene are its exciting and extraordinary properties. Especially the electronic properties, which are dictated by the electron in the delocalized π orbital, have aroused interest in research, but also hope for many applications.

In the band structure of graphene (see Fig. 2.2 B), the valence and conduction band meet at the so-called Dirac points making graphene a zero-gap semimetal. The energy dispersion at these points exhibit a linear relation which makes electrons propagating through graphene behave as if they were massless. Therefore, the electron mobility in graphene is extremely high, up to $200\,000\,\mathrm{cm^2\,V^{-1}\,s}$ for suspended graphene at low temperature.[54] In addition to its outstanding electronic properties, graphene shows very high thermal conductivity, optical transparency and is one of the strongest materials ever measured.[55,56]

Several methods for the fabrication of graphene exist. The Scotch tape method, introduced by Geim and Novoselov in 2004,[5] is still a widely used technique today. The weak van der Waals forces between the layers in graphite allow them to be separated by peeling with Scotch tape, while the layer itself remains largely intact due to the strong covalent bonds. Continuous peeling steadily reduces the number of layers of graphite, eventually resulting in few- and monolayers of graphene. This mechanical exfoliation technique produces high-quality graphene with a low defect density. However, it is time-consuming and thus not suitable for large-scale production. Exfoliation can also be performed in large quantities by using liquid-phase exfoliation. The layers in graphite are separated by means of sonication in solution, which usually results in a large number of rather small graphene fragments.[35] Wafer-scale production of graphene can be achieved by chemical vapor deposition (CVD). In this bottom-up approach, carbon-containing precursor gases are introduced into a vacuum chamber and react at high-temperature on a metal-catalyst to form graphene. However, the defect density of CVD-grown graphene is still higher than that of exfoliated graphene, making it less attractive for the fabrication of high-quality graphene.

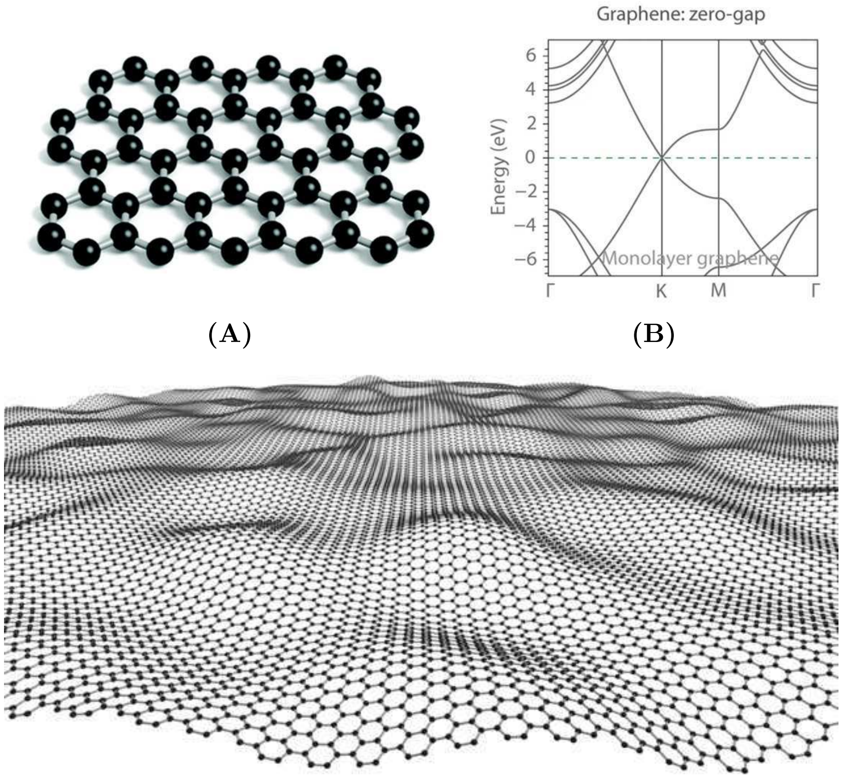

(A) **(B)**

(C)

Figure 2.2: Graphene, the pioneer of the 2D materials. (A) Illustration of the hexagonal atomic structure of graphene. (B) Band structure of graphene. The linear dispersion at the K-point results in electrons propagating as massless fermions through graphene leads to the exciting electronic properties of graphene. (C) Warping of the atomically thin graphene membrane. Reprinted with permission from (A) Roldán et al.[57], (B) Xia et al.[58], and (C) Meyer et al.[17] respectively[59].

Hexagonal Boron Nitride

Another important material in the family of 2D material is hexagonal boron nitride. The crystal structure consists of a single atomic layer with alternating boron and nitrogen atoms in a honeycomb lattice, as shown in Fig. 2.3. This makes hBN a structural analogue of graphene with a lattice constant slightly (1.8%) larger than that of graphene.[60] hBN monolayers are insulators with a band gap of approximately 6 eV.[20] It is therefore of interest as an insulating layer for electronic devices. However, hBN monolayers are only 0.33 nm thick and thus typically allow a high leakage current. For this reason, multilayer hBN is usually used.[61]

hBN monolayers can be obtained by the above mentioned mechanical and liquid-phase exfoliation. In addition, CVD processes allow the fabrication of hBN on a larger scale.[20]

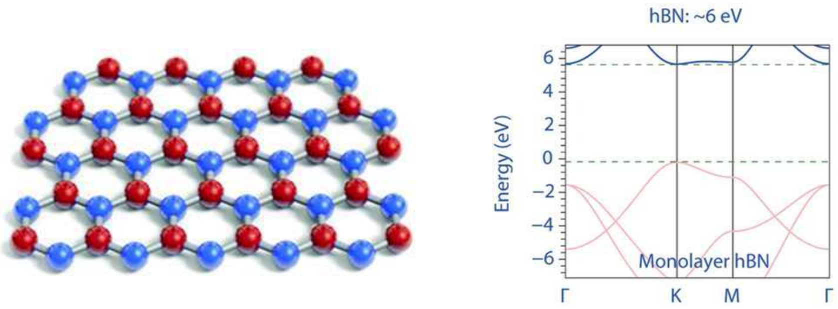

(A) **(B)**

Figure 2.3: Monolayer of hexagonal boron nitride. (A) Alternating nitrogen and boron atoms are arranged in a hexagonal lattice making hBN a single atom thin 2D material. (B) Band structure of hBN showing the large band gap. Reprinted with permission from (A) Roldán et al.[57] and (B) Xia et al.[58]

Transition Metal Dichalcogenides

Transition metal dichalcogenides comprise a whole class of 2D materials. Their crystal structure consists of a transition metal atom between two chalcogen atoms as shown in Fig. 2.4. Therefore, in contrast to graphene, a transition metal dichalcogenide (TMD) monolayer includes three atomic planes, resulting in a thickness of 0.6 - 0.7 nm.[62]

TMDs can exist in different structural forms, i.e. polymorphisms, with variations in the arrangement of their atoms. The most common forms for monolayers include the 1T (octahedral coordination) and 2H (trigonal prismatic coordination) phases, as shown in Fig. 2.4 A. The chemical composition of the TMD determines the thermodynamically stable form. TMDs have the general formula MX_2 and

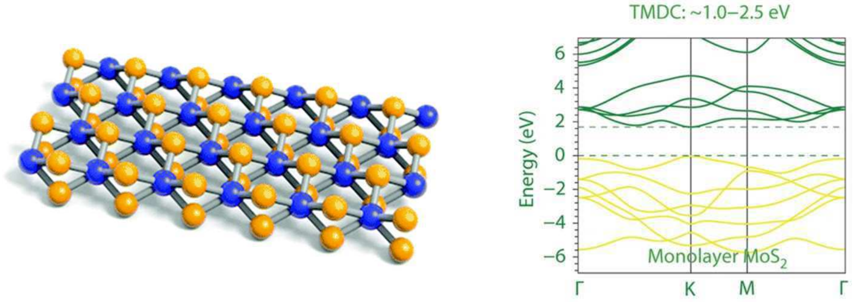

(A) **(B)**

Figure 2.4: (A) Structure of transition metal dichalcogenide monolayer with the chalcogen and metal atoms indicated by yellow and blue spheres, respectively. (B) Direct band gap in the calculated band structure of MoS_2. Reprinted with permission from (A) Roldán et al.[57] and (B) Xia et al.[58]

many different metal-chalcogen combinations are known such as MoS_2, tungsten disulfide (WS_2), tungsten diselenide (WSe_2), niobium diselenide ($NbSe_2$) and others. The electronic properties of TMD monolayers are likewise highly dependent on the chemical composition, ranging from semiconducting to superconducting. Superconductivity was observed for $NbSe_2$ at about 3 K.[63] Semiconducting behaviour can mainly be found for the group-VI TMDs, i.e. Mo or W as metal. For group-VI TMDs, except for tungsten ditelluride (WTe_2), the thermodynamically stable form is the trigonal prismatic coordination (2H).

Similar to graphene, TMDs can be obtained by mechanical exfoliation from the bulk crystal as well as by direct growth by means of CVD.[18,64]

The band structure of group-VI TMDs is dependent on the thickness, i.e. the number of layers. The bulk material, multilayers as well as bilayers show an indirect band gap. However, TMD monolayers have a direct band gap in the visible range of about 1 - 2 eV and therefore attracted attention for the application in electronic and optical devices.[25,29,66,67] Fig. 2.6 shows the investigation of the photoluminescence (PL) of TMD monolayers. In (A), an optical image of a CVD-grown MoS_2 flake is given. The flake consists of a surrounding monolayer area, with a small bilayer region in the centre. The bilayer can be clearly recognized by the darker contrast. The second layer is grown at an angle of 180°, thus indicating the AB stacking of the bilayer. In single layer MoS_2, the PL is dominated by the radiative recombination of a primary exciton with an energy of about 1.88 eV.[68] A PL intensity map of this exciton is shown in the lower part of Fig. 2.6 A for the CVD-grown flake. The PL signal of the monolayer region is 100 times stronger than that of the bilayer region, which is due to the transition from an indirect to a direct bandgap semiconductor.

The PL spectra of different TMD monolayers are shown in Fig. 2.6 B. In this study, the influence of the silicon dioxide (SiO_2) substrate as well as the tempera-

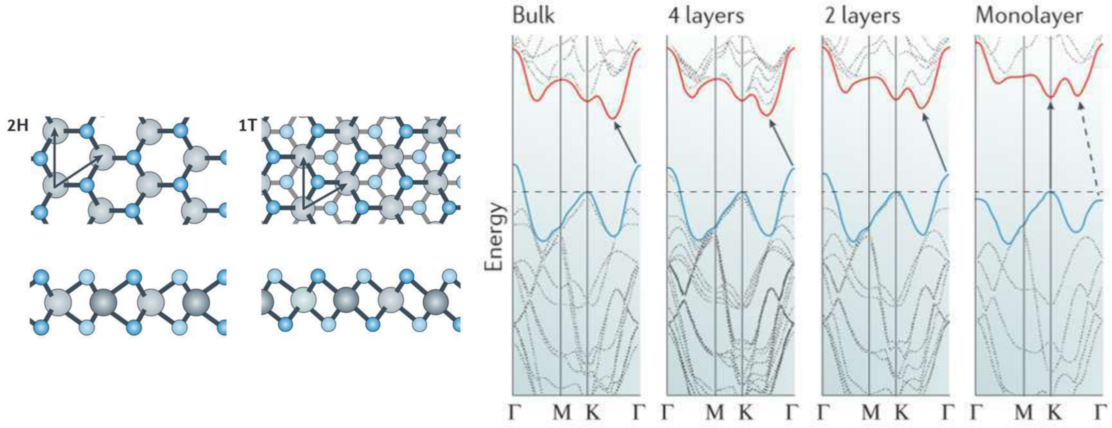

(A) **(B)**

Figure 2.5: (A) Trigonal prismatic (2H) and distorted octahedral (1T) phase of TMDs. For the 2H phase, the chalcogen atoms are located on top of each other, whereas in the 1T phase they are shifted. (B) Band structure of 2H-MoS_2 for different thicknesses. The monolayer shows a direct band gap while in thicker MoS_2 an indirect band gap occurs. Reprinted with permission from Manzeli et al.[65]

ture is investigated. Therefore, monolayers are prepared directly on the substrate or capped between hBN layers. Different emission energies can be observed for the various materials, representing the slightly different band gap of TMD monolayers. An increase of the signal intensity as well as a narrower emission linewidth can be observed for the hBN-capped samples as well as for lower temperatures. The small linewidth reveals the presence of various emission peaks, indicating the more complex origin of the PL signal for most TMDs rather than a single exciton recombination. The reduced and broadened signal can be attributed to the SiO_2 substrate due to its surface roughness as well as charge transfer and local electric field fluctuations, all prevented by the capping in hBN.[69] Low-temperature measurements affect the influence of phonon coupling and defects states.

In particular, defects can lead to non-radiative recombinations and additional localized energy levels, causing a broadened and reduced PL signal. Chalcogen vacancies are the most common defect in the TMD monolayers and lead to states 0.1 - 0.3 eV below the conduction band minimum.[70] However, selected defect manipulation can be used for targeted band structure modifications to achieve beneficial properties, as will be considered in more detail in Section 2.3.

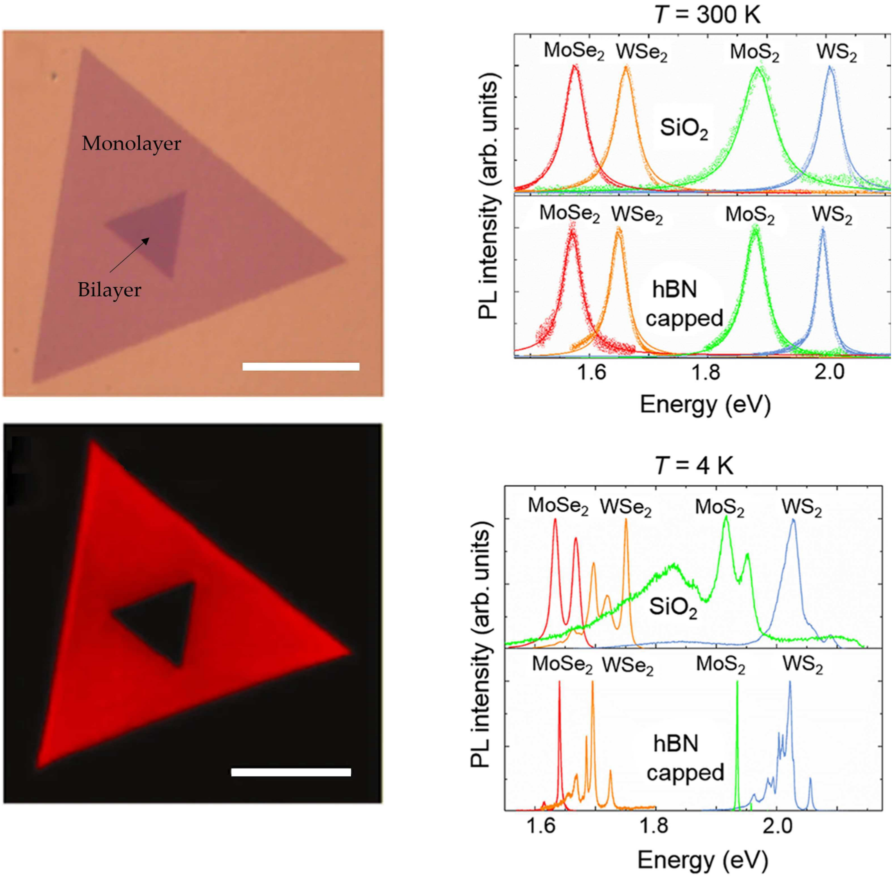

(A) (B)

Figure 2.6: Photoluminescence of TMD monolayers. (A) Optical microscope image of MoS_2 flake and corresponding PL intensity map of the exciton peak. In the monolayer region, a significantly higher PL signal can be measured due to the direct band gap. Scale bar is 50 µm. (B) PL spectra measured for different TMD monolayer materials. The influence of the SiO_2 substrate is investigated by comparing the signal with hBN-capped TMD layers. Capping in combination with low temperature result in narrow linewidths and higher intensities of the emission by reducing charge transfer to the substrate as well as non-radiative recombination due to defects. Reprinted with permission from (A) Zhang et al.[71] and (B) Cadiz et al.[69]

2.2 Van der Waals Heterostructures

The extensive studies on 2D materials, in particular on graphene, led to another new research area. Investigation of the electrical properties of graphene on Si/SiO$_2$ revealed the limitation of studying substrate-supported 2D materials: Scattering due to charged surface states as well as impurities limit the quality of graphene and thus prevent realising its full potential.[72–74] Measurements on suspended graphene led to improvements,[54,75] but of course involve challenges in terms of sample design and preparation, as well as measurement techniques. Thus, alternative substrates were explored. Dean et al. have successfully demonstrated the use of hBN as insulating support. In short, mechanically exfoliated graphene was picked up using a polymer carrier, and eventually placed on top of another exfoliated hBN flake.[37] The large band-gap, similar lattice constants, and the absence of dangling bonds and surface charge traps make hBN on the one hand a well-suited substrate for studying the electrical properties of graphene.[38,76]

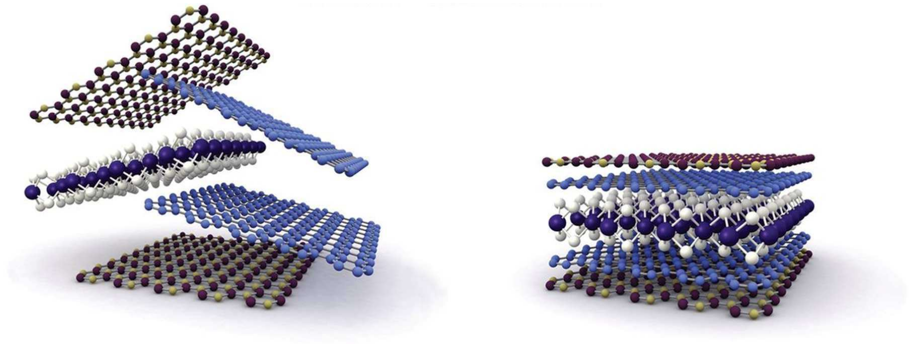

(A)

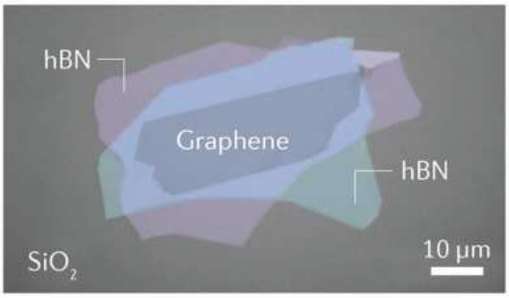

(B)

Figure 2.7: (A) Visualization of the concept of van der Waals heterostructures. Various 2D materials are combined to form a stack of layers made up of different materials. (B) Optical microscope image of an hBN-graphene-hBN sandwich on SiO$_2$ substrate. Reprinted with permission from (A) Novoselov et al.[77] and (B) Wang et al.[40]

On the other hand, it was the first realisation of a 2D-2D heterostructure and the beginning of the emerging field of vdWHs. As for the bulk counterparts of 2D materials, each layer in vdWHs consists of a covalently bonded lattice and is bound by weak van der Waals interactions to the neighbouring layers. Most importantly, however, instead of having the same material in each layer, the heterostructure can contain different materials in each layer without the constraints of lattice matching.[78] The combinations of these artificial composites are practically endless, due to the large number of 2D materials as well as the ability to modify each layer in terms of its electronic, optical, structural or chemical properties.[34] Fig. 2.7 illustrates the concept of vdWHs and an optical microscope image of a fabricated hBN-graphene-hBN sandwich. The vertical atomic layer sequence of a heterostructure can be seen in Fig. 2.8. A cross-section of the heterostructure is prepared and imaged by means of TEM, showing the atomically sharp and clean interface between the different 2D materials.

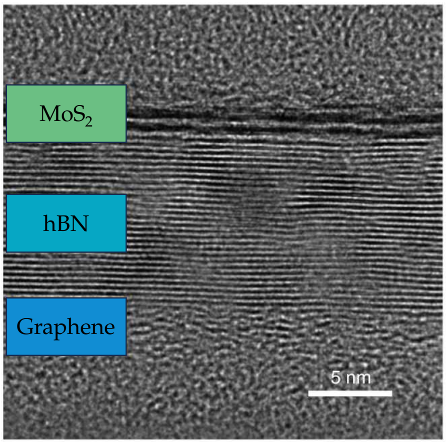

Figure 2.8: Cross-sectional TEM image of a MoS_2-hBN-graphene heterostructure between substrate and protective layer. Scale bar is 5 nm. Reprinted with permission from Liu et al.[79]

The van der Waals assembly allows building of extremely thin functional structures, which will be considered in more detail below, but also the capping and encapsulation of a 2D material with protective layers to improve its electrical properties[80] or to increase the stability under electron beam irradiation.[81] In addition, the assembly of crystal structures allows the creation of superlattices, which frequency is set by adjusting the twist angle. By doing so, the band structure of the heterostructure can be tuned and unpredicted properties of material combinations have been found.[82–84] For example, bilayer graphene with a twist angle of 1.1°, which is called the magic angle, showed superconducting behaviour.[36,85]

Several techniques for the fabrication of vdWHs exist, among which the mechanical assembly as well as the direct growth by CVD are the most established methods.[35,77] In the following, these two methods will be presented, followed by some examples and applications showing the possibilities of these artificial materials.

Mechanical Assembly

The most common method for the creation of vdWHs is the mechanical assembly of different 2D materials, which is sometimes referred to as deterministic assembly. While several variations in the process steps exist, the required setup is always based on an optical microscope with a long working distance to observe the stacking including micromanipulators for positioning.

The mechanical assembly approach has been pioneered by Dean et al. in 2010 by placing graphene on hBN as insulating substrate.[37] Therefore, a PMMA layer serves as sacrificial layer to carry the 2D material during the transfer steps of the assembly. The process is shown in Fig. 2.9 A. A Si/SiO_2 wafer is coated with a water-soluble polymer followed by PMMA. Graphene is exfoliated using the Scotch-tape method directly onto the polymer-PMMA stack. Immersing the stack into deionized water, dissolves the polymer, leaving the 2D material attached to the PMMA floating on the water surface. Using a glass slide, the PMMA layer with the graphene flake can be caught and taken out of the water. For the target substrate, hBN is exfoliated onto another Si/SiO_2 wafer. Finally, the graphene can be positioned on top of the hBN flake by using a micromanipulator carrying the glass slide and an optical microscope for observation. The sacrificial PMMA layer is dissolved in acetone resulting in the hBN-graphene assembly.

Several variations of this method exist, e.g. by using different water-soluble polymers[24,86] or other sacrificial layers.[82,87] Schneider et al. developed a method in which an exfoliated 2D material flake on Si/SiO_2 is covered with a hydrophobic polymer.[88] Dipping the stack into water delaminates the polymer due to intercalation of water between the hydrophobic polymer and the hydrophilic Si/SiO_2. The polymer, carrying the flake, remains floating on the water surface. By pumping down the water, the flake including the polymer can be transferred onto another 2D material followed by dissolving the polymer.

All these methods are based on using a thin film as carrier of the 2D material which is then removed after the placement on the substrate or another 2D material. Other techniques have been developed without the need of such a sacrifical layer. For example, Castellanos-Gomez et al. used a viscoelastic stamp made out of PDMS as carrier.[89] The 2D material is directly exfoliated onto the PDMS and subsequently put on top of the target substrate. Again, an optical microscope and micromanipulators are used for the exact positioning. By slowly raising the PDMS, the flake is released and remains back on the target. As no sacrificial layer is used in this method, no wet chemistry is required and thus, making this all-dry method advantageous because no polymer residues can remain between the 2D material layers.

Wang et al. presented an approach for exploiting the van der Waals forces between 2D materials for picking up and carrying an exfoliated flake.[40] First, hBN is exfoliated onto a PDMS-polymer stack and attached to a glass slide. The hBN is brought into contact with the desired 2D material on Si/SiO_2 and used to pick it up due to the van der Waals forces between them. The stack is then stamped onto the target substrate leaving the layer assembly behind. This avoids any potential residues, as the desired 2D material is never in contact with polymers. However, the final assembly of the 2D materials is capped by the hBN carrier.

In summary, the mechanical assembly techniques allow the fabrication of van der Waals heterostructures from previously prepared 2D materials without constraints of lattice mismatches. The required setup is relatively cheap and can easily be implemented inside a glovebox to perform the assembly in a controlled environment. The 2D materials are transferred with the help of a carrier substrate, as for example different polymers, viscoelastic stamps or other 2D crystals. All-dry methods have been implemented in order to avoid the use of solvents, which can result in undesirable residues. The observation by an optical microscope and the use of micropositioning systems allows the alignment of the individual layers of the van der Waals heterostructure within a few micrometers.[37]

With the upcoming research field of twistronics, the control of the twist angle between the individual layers of the heterostructure becomes important to create a desired superlattice. The mechanical assembly of vdWHs allows control of the twist angle by adding a rotational axis to the micropositioning system. Importantly, the lattice orientation of the 2D crystals has to be known. Therefore, the straight edges of exfoliated or grown 2D materials can be exploited as they indicate the orientation.[90] In addition, second harmonic generation or polarized Raman spectroscopy can be used.[80,91] Kim et al. presented another technique for the creation of twist-controlled structures: A twisted bilayer can be achieved by picking up a section of a deposited 2D material, followed by a relative rotation and the re-deposition of the section on top of the remaining flake.[92] For this method, knowledge of the crystal orientation is not necessary, however, only assemblies consisting of the same material can be produced.

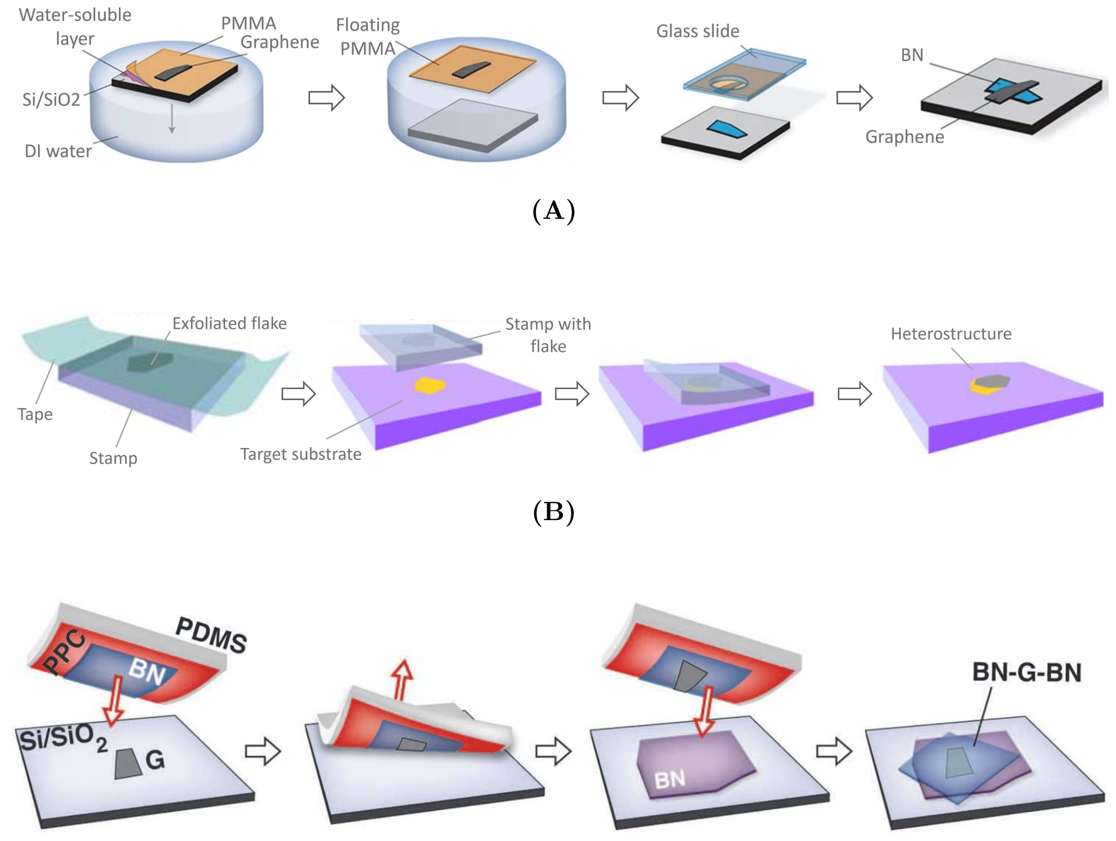

(A)

(B)

(C)

Figure 2.9: Mechanical assembly methods. (A) Graphene is exfoliated on a polymer-PMMA stack. The polymer is dissolved in water, allowing the graphene to be caught with a glass slide as carrier to position the PMMA-graphene stack on top of an hBN flake. The graphene is released by dissolving the PMMA layer in acetone. (B) Exfoliating the 2D material directly on a viscoelastic stamp avoids the use of polymer layers and wet chemistry. (C) The van der Waals (vdW) forces between 2D materials can be used to pick up other 2D flakes, avoiding any contact with other carrier media. Reprinted with permission from (A) Dean et al.[37], (B) Castellanos-Gomez et al.[89], and (C) Wang et al.[40]

Growth Methods

Another method for the fabrication of vdWHs is the direct growth by means of CVD. As for the fabrication of pure 2D materials, CVD processes allow the fabrication on larger scales in comparison to mechanical exfoliation and mechanical assembly.

However, direct growth of a heterostructure is challenging. For many material combinations, the environment and parameters required for high-quality growth prevented the entire CVD fabrication of heterostructures. For example, growing TMDs on CVD-hBN required the transfer of the hBN from the copper substrate used for the synthesis to sapphire due to the reaction of S with Cu.[93] In addition, the high temperatures as well as the oxygen containing precursors used for growing TMDs decomposed the already grown hBN. Therefore, TMDs were often grown on exfoliated hBN.[94] In recent years, however, improvements in growth processes have enabled the direct growth of the entire heterostructure.[95–97]

In contrast to the mechanical assembly, the synthesis of vdWHs allows the creation of both vertical and lateral heterostructures. In the latter, the different materials grow in the same plane and are connected by covalent bonds.[35] Gong et al. showed the formation of vertical and lateral WS_2/MoS_2 heterostructures in the same system depending on the process temperature.[95]

The position of the grown heterostructure is barely controllable as it is based on random nucleation. However, there have been a few attempts to control the growth of the top 2D material of a bilayer heterostructure.[98,99] For example, Li et al.[99] have shown that laser patterning of a grown mono- or bilayer 2D material creates defects, which serve as nucleation sites for the growth of a second material

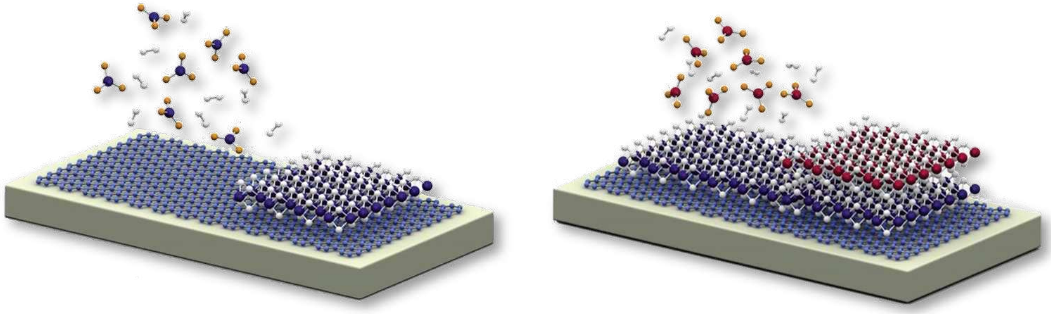

Figure 2.10: Direct growth of vdWHs. Precursors react from the gas phase on a heated substrate, ideally forming a monolayer of the target 2D material. By repeating the process with different precursors and process conditions, different layers can be grown on top of each other. Reprinted with permission from Novoselov et al.[77]

on top. By doing so, regular arrays of heterostructures have been fabricated, but the controlled positioning is limited in comparison to the mechanical assembly.

The twist angle between the layers depends on the growing conditions as well. For the mechanical assembly approach, in principle any twist angle is possible and freely selectable. In contrast, only a few distinct twist angles are allowed when growing vdWHs epitaxial.[100] Nevertheless, recent work has shown that gas-flow perturbations in combination with certain substrate geometries creating non-equilibrium growing conditions which increases the amount of twisted bilayer graphene.[101]

2.3 Patterned 2D Materials and vdW-Structures Tailoring Properties for Applications

The fields of applications of pristine 2D materials and their vdW heterostructures are numerous. In addition, specific modifications can be applied to tailor the properties to be optimized for a certain application. Optical and electrical applications were the focus in research to date, with modifications mainly targeting band-gap engineering. However, tailored 2D materials have also been used to create advanced nanopores and for sensing applications.

Several approaches have been used to tailor the properties of 2D materials, such as applying electric fields,[102,103] doping with impurity atoms[104] and inducing strain.[105,106] In the following, however, in particular the modification of properties based on patterning the materials on the nanometer scale will be considered.

In its pristine form, graphene is a zero-gap semimetal. Thus, opening a band-gap with a defined energy is of great interest for applications. Theoretical works initiated the area of band-gap engineering of nanopatterned graphene (see Fig. 2.11 A). Regular arrays of holes, also called an antidot pattern, can result in a band-gap of several eVs depending on the hole size and frequency.[107] In addition, the confinement in a graphene nanoribbon leads to a semiconducting behaviour. Density-functional theory (DFT) calculations indicate that a band-gap similar to germanium or indium nitride can be achieved with a ribbon width of 2 - 3 nm, and one similar to silicon or gallium arsenide with a width of 1 - 2 nm.[108]

Experimental band-gap engineering by means of nanopatterning has also been carried out, and partially applied in functional devices. Nanoperforated graphene has been fabricated with electron beam lithography[109] or block copolymer lithography[110,111] and investigated for its electrical properties. For example, a 150 meV wide band gap has been realized in encapsulated graphene, as illustrated in Fig. 2.11 B.[109] The band gap is tunable by applying a magnetic field. Fig. 2.11 C shows the integration of nanopatterned graphene field-effect transistor (FET) device.[110] Typical responses of a semiconducting film on the applied gate voltage can be observed. In addition, the transfer characteristic is tunable by adjusting the periodicity and size of the introduced holes.

Besides typical semiconductor applications, graphene nanoribbons have been demonstrated as a gas sensor, as shown in Fig. 2.11 C.[112] Photolithography and oxygen plasma were used to introduce the ribbon structure into graphene. Afterwards, the patterned graphene was transferred onto polyimide as substrate, making the sensor transparent and flexible. Due to the restricted size, the ribbon exhibits Joule heating when the bias voltage of the measurement is applied, enabling the reversible NO_2 absorption and desorption without the need for external heating for recovery of the sensor. This all-graphene sensor impressively demonstrates the ability to fabricate both the active area as well as the electrodes from a single graphene layer by specific nanopatterning.

Band-gap engineering by means of nanopatterning has also being investigated for TMD monolayers. In a theoretical study, Shao et al.[113] calculated the resulting band-gap for different antidot lattices in MoS_2. By varying the hole sizes and distances, the band-gap energy converges to a certain value for increasing supercell areas. Thus, the change was attributed to an edge effect of the simulated structures.

Due to their excellent optical properties, experimental work has been carried out to tailor them for use in applications by patterning with top-down-techniques such as electron beam lithography. However, the introduced electron dose was found to damage the TMD monolayer, leading to degraded optical properties. Stanev et al.[114] revealed the significant degradation of the PL. However, they have shown that encapsulation in hBN during patterning provides a beam damage protection to preserve the native optical properties. In low-temperature PL measurements, a weak size-dependent energy shift could be observed for an antidot lattice introduced into encapsulated molybdenum diselenide ($MoSe_2$). As the patterned materials were on a silicon substrate, transmission electron microscope (TEM) could not be used to understand the observed shift.[114]

MoS_2 nanoribbons have been directly grown on a phosphine treated silicon wafer as shown in Fig. 2.12 A, avoiding a potential effect on the resulting properties due to the patterning method.[115] Compared to 2D MoS_2, the ribbons exhibit a PL peak which is about 50 meV higher in energy. In addition, the emission is tunable by adjusting the ribbon width.

A number of promising approaches for nanophotonics have already been demonstrated for thin film TMDs. Besides emitting and harvesting light, nanopatterned TMD films can serve as waveguides.[116] Similar applications can certainly be expected for nanostructured 2D TMDs. As an example, spatially controlled second-harmonic generation has been shown for a nanopatterned MoS_2 monolayer (see Fig. 2.12 B).[117] Diffraction of the generated second-harmonic at an introduced

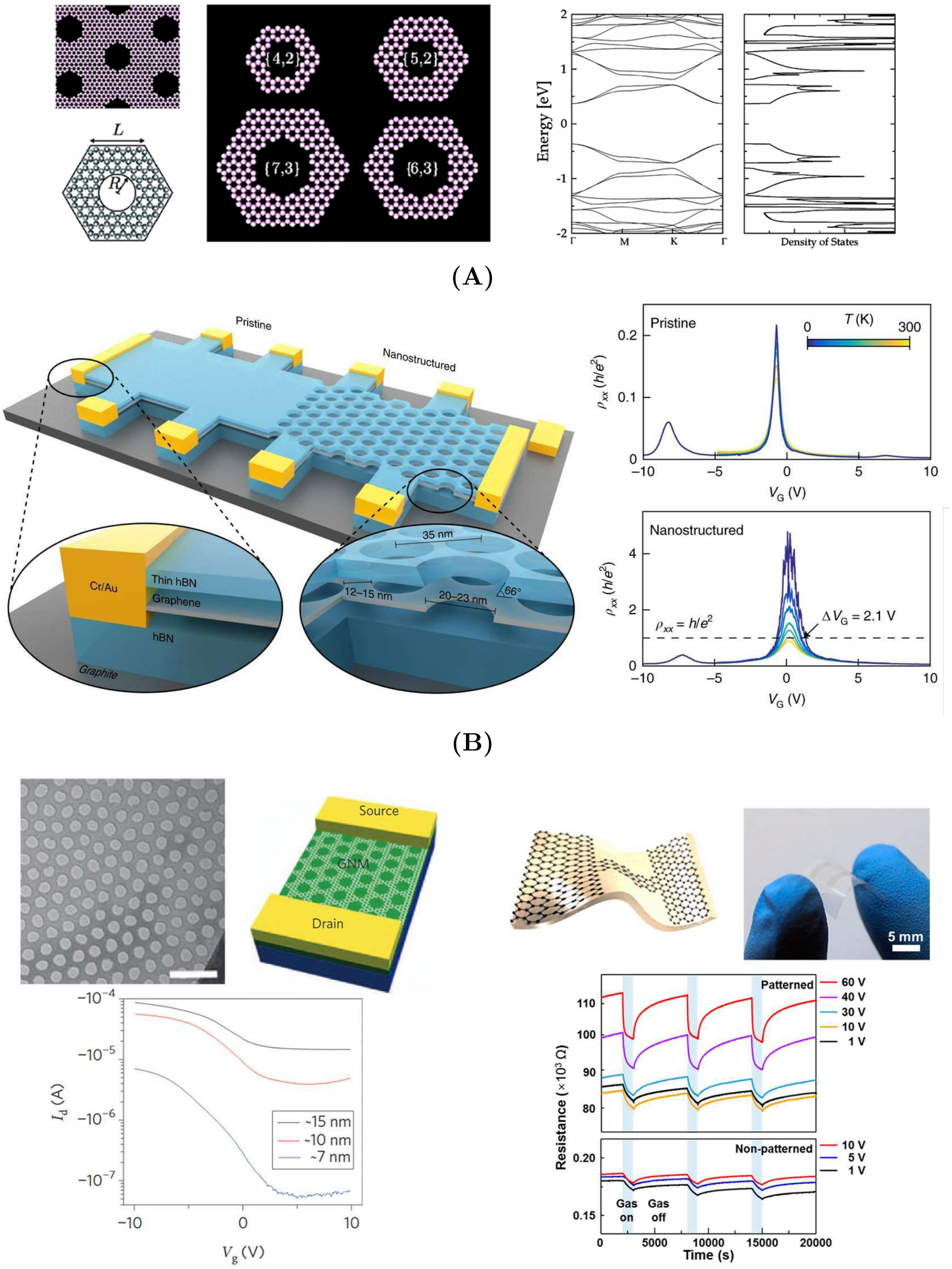

(A)

(B)

(C)

(D)

Figure 2.11: Tailoring the properties of graphene for applications. (A) Theoretical study of opening a band gap by introducing an antidot lattice. Depending on the hole size and frequency of the lattice the energy of the band gap can be adjusted. (B) Electron beam lithography is used for nanostructuring graphene encapsulated in hBN. Resistivity measurements reveal a band gap of approximately 150 meV. (C) Application of a graphene antidot lattice as FET device. The transistor properties can be adjusted by varying the lattice structure. The scale bar is 100 nm. (D) Application of a graphene nanoribbon as gas sensor. The restricted size results in Joule heating of the sensor area when applying the bias voltage, enabling reversible NO_2 absorption and desorption without external heating. Reprinted with permission from (A) Pedersen et al.[107], (B) Jessen et al.[109], (C) Bai et al.[110], and (D) Kim et al.[112]

grating allows the controlled emission. Moreover, fabrication of a fork-like pattern as grating results in the generation of a vortex beam in the first diffraction order of the second-harmonic wave.

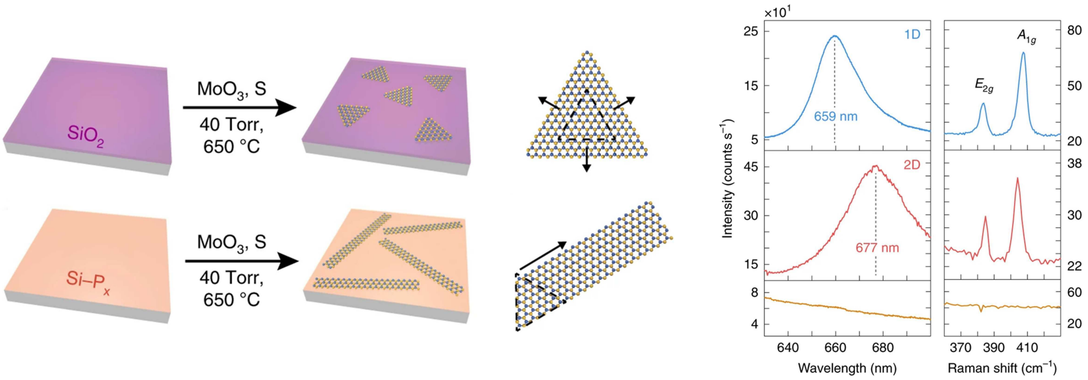

(A)

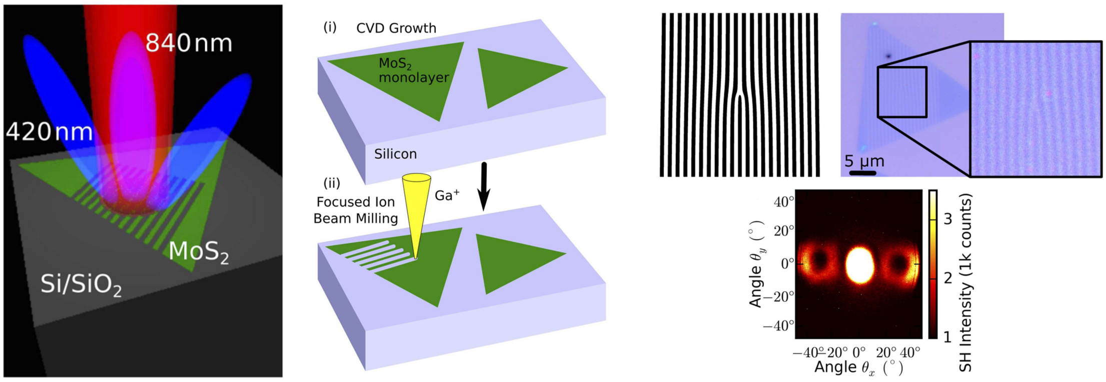

(B)

Figure 2.12: Properties and application of nanopatterned TMD monolayers. (A) MoS_2 nanoribbons are directly grown on a phosphine treated silicon wafer. The optical properties of the ribbons are tested and compared to a conventional 2D MoS_2 flake. In the PL measurement, the ribbon exhibits a tunable exciton emission at higher energies (blue curve). The orange curve shows the background signal of the phosphine silicon wafer. (B) Second-harmonic generation at a MoS_2 monolayer. The patterned grating leads to a diffracted emission. (Right) Introducing a fork-like grating generates a second-harmonic vortex beam in the first order of the diffraction pattern. Reprinted with permission from (A) Chowdhury et al.[115] and (B) Löchner et al.[117] © Optica Publishing Group.

As introduced above, 2D materials can be combined to create layered artificial solids. The properties of these vdWHs can be tailored by the composition, the layer sequence and the relative orientation of the layers. The possibilities are even more versatile, as each individual layer can be modified as described above, for example by nanopatterning. The main tool for tailoring the properties of vdWHs is based on adjusting the twist angle between the layers, thus controlling the frequency of the resulting supperlattice. In the most prominent example, two graphene monolayers have been stacked at a specific angle of 1.1°.[84] The resulting electronic band structure is dominated by the superlattice and exhibits superconducting properties. Moreover, the fabrication of graphene-hBN stacks allowed the experimental investigation of the quantum Hall effect.[119]

Regarding the optical properties of TMD heterostructures, the PL emission peak can also be tuned by adjusting the twist angle. Fig. 2.13 shows the investigation of $MoSe_2/WS_2$ heterobilayers assembled under different angles.[118] The newly appearing peak (P1) is compared to the exciton peak of a $MoSe_2$ monolayer (X_A). Hybridization of the excitonic bands of the two materials result in an altered PL spectra with an energy shift as a function of the twist angle.

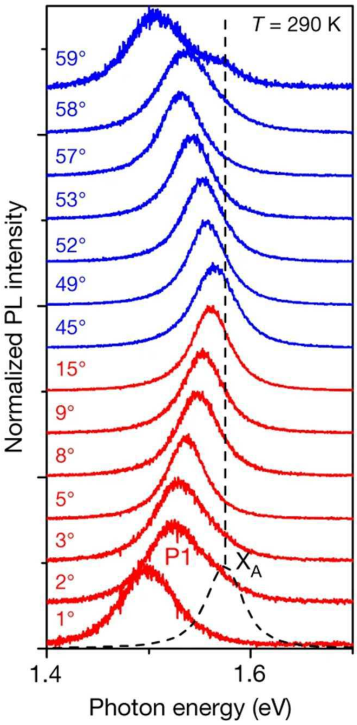

Figure 2.13: PL spectra of $MoSe_2/WS_2$ heterostructure for several twist angles. Reprinted with permission from Alexeev et al.[118]

VdWHs have emerged as promising platforms for various functional lightweight and flexible devices. Due to the unique and diverse properties within the family of 2D materials, optoelectronic applications are numerous, such as FETs, flash memories as well as light harvesting, detection or emission devices, to name just a few. Planar 2D FETs with different compositions have been realized. A coplanar design as illustrated in Fig. 2.14 A was used for a FET, which employs graphene as bottom contact and MoS2 as the transistor channel material.[120] While most devices are based on exfoliated 2D materials and are therefore one-off pieces, CVD processes enable large-scale fabrication and building of entire logic circuits, even with interconnections made of graphene.[121] By encapsulating the entire functional device with hBN (see Fig. 2.14 B), extremely high charge-carrier mobilities can be achieved in MoS_2.[122]

Optoelectronic devices are particularly based on TMD materials due to their intrinsic band-gap and strong absorption in the visible spectrum. For example, a monolayer $MoSe_2$ with a thickness of 0.65 nm absorbs as much light as 15 nm GaAs or 50 nm silicon.[123] In addition, high internal quantum efficiencies of over 70% have been shown for a graphene-WSe_2-graphene photodetector.[124] An illustration and schematic of the device is given in Fig. 2.14 C.

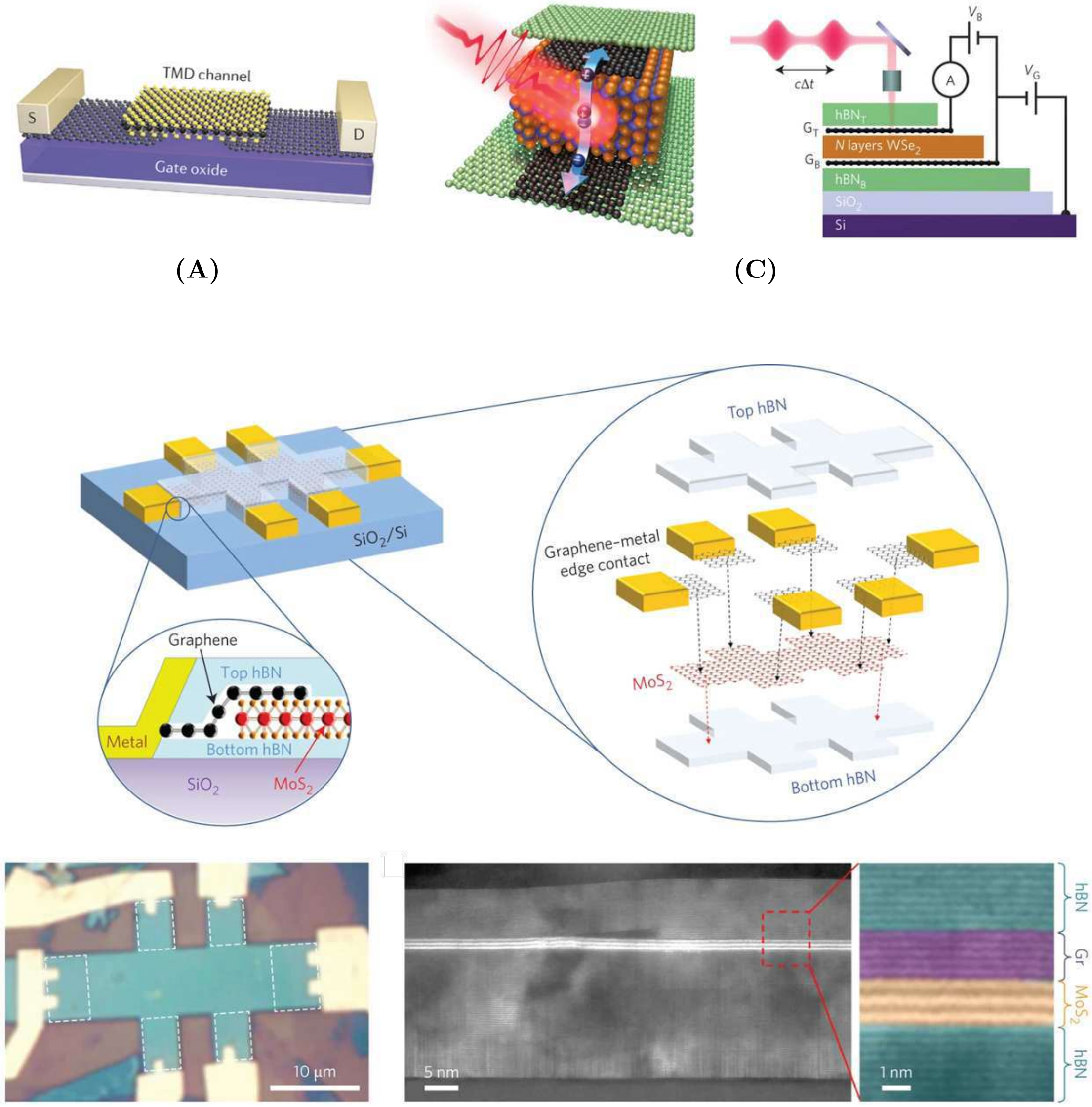

(A) **(C)**

(B)

Figure 2.14: Functional devices based on vdWHs. (A) Design of a planar transistor with TMD as the channel material and graphene as bottom contacts. (B) MoS_2-based device encapsulated in hBN to avoid extrinsic scattering of the charge carriers. A cross-sectional TEM image shows the atomic layer structure of the device. (C) Photodetector consisting of multiple layers of WSe_2 as active element, hBN as encapsulation and graphene as electrodes connected for the measurement. Reprinted with permission from (A) Liu et al.[78], (B) Cui et al.[122], and (C) Massicotte et al.[124]

2.4 Electron Microscopy

Studying small objects requires the ability to observe them. Microscopy in general comprises a variety of different techniques to magnify objects that are not visible by the eye alone due to their small size. The oldest microscopy technique, optical microscopy (OM), has been developed since the late 16th century and, in its simplest form, uses visible light and lenses made of glass.[125] However, the resolving power of an optical microscope is limited by the optical diffraction limit, which is determined by the wavelength of the photons used. The resolution can be defined as the smallest distance between objects that can still be distinguished and is around 200 - 300 nm for a good optical microscope.[126] Thus, materials can not be investigated on the atomic scale by means of OM, which would require an improvement in resolution of about a factor of 1000.

Electron microscopy (EM), on the other hand, uses electrons for imaging. As introduced by Louis de Broglie in 1924, electrons have wave-like characteristics as well.[127] However, due to their smaller wavelength in comparison to photons, better resolutions can be achieved. Only few years after the discovery of de Broglie, Hans Busch developed electromagnetic lenses for electrons as the equivalence to glass lenses in OM.[128] The application of using theses lenses in an electron microscope was then invented by Leó Szilárd in 1928.[129] In the following years, Ernst Ruska and Max Knoll accomplished to take the first magnified image using electrons. Shortly after, in 1933, they built the first TEM which exceeded the resolving power of optical microscopes.[130,131]

Since then, further research has been conducted in the field of EM. With spectroscopic methods such as energy-dispersive X-ray spectroscopy (EDS) and electron energy loss spectroscopy (EELS), materials can be examined for their chemical composition.[132,133] Great development work has also been carried out to improve the resolving power of the microscopes by increasing the electron energy or developing new techniques like wavefront restoration or off-axis holography.[134–137] In this regard, theoretical work by Otto Scherzer has revealed that spherical aberrations cannot be avoided for static, rotationally-symmetric electromagnetic lenses as commonly used in EM. This consequently limits the achievable resolution.[138,139] However, the invention of aberration correctors for electron lenses eventually led to the powerful microscopes capable to resolve materials atomically, and which are used today in both materials science as well as in biology for structure elucidation.[140–142]

2.4.1 Conventional Transmission Electron Microscopy

The principle of the originally developed EM by Ruska and Knoll, the conventional transmission electron microscopy (CTEM), corresponds well to that of an OM. As mentioned above, however, a beam of accelerated electrons is used instead of an electromagnetic wave. The high-energy electrons transmit the thin, usually up to 100 nm, sample and thereby interact with the specimen and provide information about its structural morphology and chemical composition. In contrast to an OM, vacuum inside the microscope is required to avoid scattering of the electrons with air molecules. This would falsify or even prohibit the signal arising from the interaction with the specimen. Therefore, the entire beam path runs inside of a vacuum tube. Fig. 2.15 shows the schematic setup of a typical CTEM. In the following, the main components are discussed in more detail.

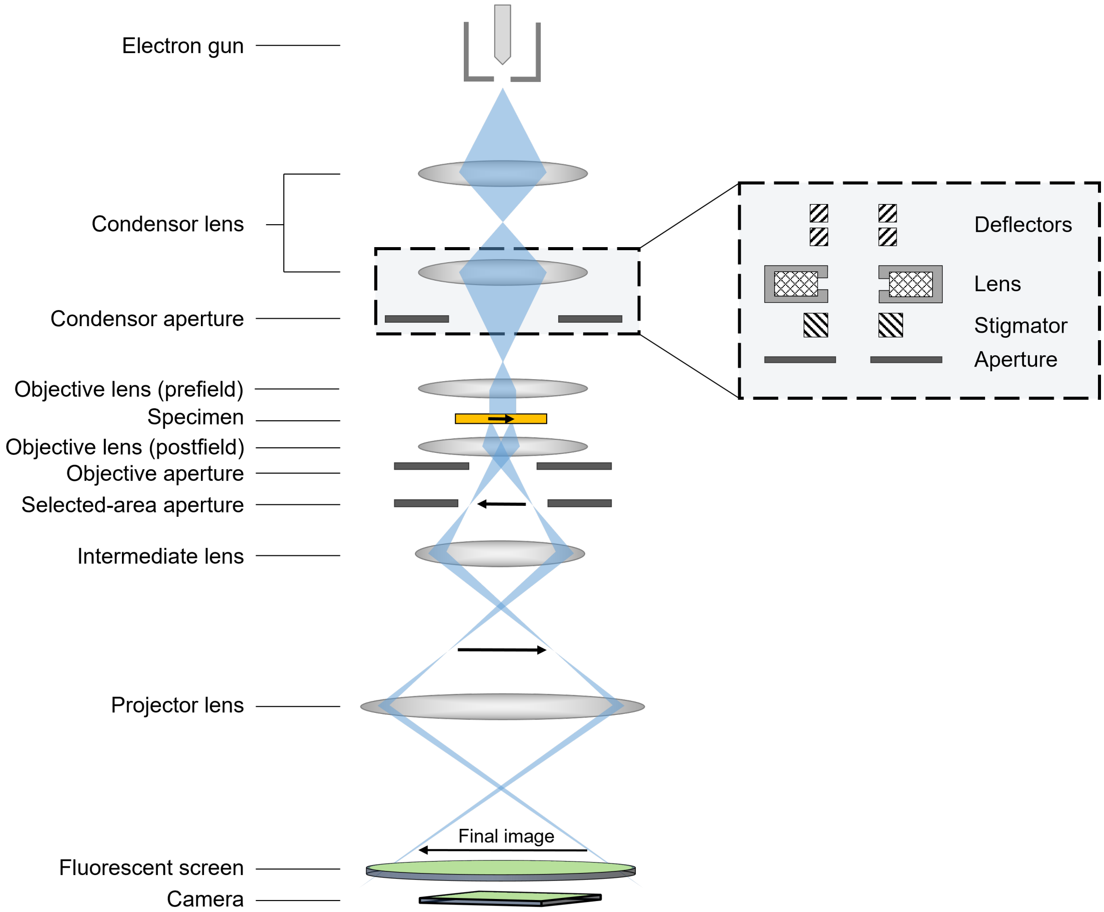

Figure 2.15: Schematic diagram of a conventional transmission electron microscope.

Electron gun

The electron gun consists of two elements: the electron source that provides the electrons as well as a system to accelerate them to a certain energy, typically in the range of 60 - 300 keV, which is sufficient to transmit the thin TEM specimens.

Today, there are two types of electron sources, thermionic and field-emission sources. In both cases, the electrons have to be lifted above the potential wall of the source material to be extracted and enter the vacuum of the microscope. The required work is called the work function.

In thermionic sources, the energy to overcome the work function is provided by heating. Early microscopes were equipped with tungsten filaments which have to be heated to 2700 K. Current thermionic sources use a lanthanum hexaboride (LaB_6) crystal which requires only about 1900 K for the emission of electrons.[143] A smaller temperature results in a smaller energy spread of the produced electrons. The resulting improvement in coherence is favorable for increasing the resolution of the microscope.[144]

Field emission sources, on the other hand, exploit the so-called Schottky effect. The work function for electrons is reduced by applying a high electric field to the tip of the electron source. By doing so, Schottky field emission guns (FEGs) which usually consist a tungsten tip coated with zirconium oxide (ZrO_2) emit electrons when operating at a temperature of 1800 K. In addition, with higher electric fields the potential wall becomes thinner and electrons can tunnel through the barrier. With sufficiently small tip radii, emission of electrons can occur even at room temperature. These so-called cold FEGs have to be operated at ultra-high vacuum, however, possess an extremely small energy spread.

The design of the acceleration system for the creation of electrons with short wavelengths depends on the type of electron source. For a thermionic source, a triode system is used. The cathode is at a high negative potential and the emitted electrons are accelerated to the grounded anode. The potential difference between cathode and anode represents the acceleration voltage. The third electrode, the so-called Wehnelt cylinder, is located around and just below the cathode. Its potential is slightly more negative compared to the cathode and thus reduces the beam current. However, the exact potential is controlled by the beam current itself, leading to a self-biasing arrangement and stabilisation of the emission. In addition to its control function, the Wehnelt cylinder acts as an electrostatic lens to focus the electrons already in the gun.

In a FEG, again the cathode is at negative potential. A positively charged extractor electrode with just a few kilo volt potential is placed below the cathode. The extractor builds up the electric field at the tip required to extract the electrons. Another electrode with weakly negative potential, the so-called suppressor, surrounds the cathode and avoids the emission of electrons coming from any other part than the tip. The grounded anode is located below the extractor electrode and accelerates the electrons. To focus the electrons in the gun, a gun lens is used, but also the electrostatic field between extractor and anode acts as a focusing element.

Electromagnetic lens system

The electron lenses usually used in EMs are magnetic lenses. They consist of a coil of copper wires that are housed in a cylindrical symmetrical core of iron, which is known as pole piece. A current passing through the coil creates a magnetic field inside the bore of the pole piece. While the field is axially symmetric, the field strength increases from the center of the gap towards the edge of the bore.

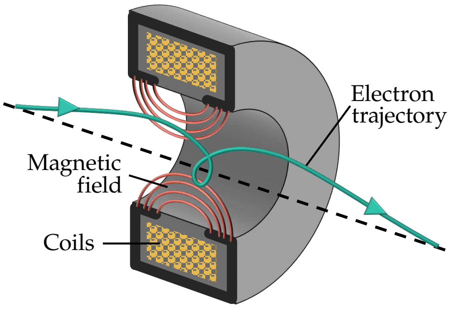

Figure 2.16: Electromagnetic lens.[143,145]

Electrons coming straight down and passing the center of the lens remain undeflected. However, electrons that are not parallel to the optical axis experience forces that bend their path. The Lorentz force depends on both the velocity of the electron as well as the magnetic field it is passing through. At first, the electron coming with an angle experiences a force that pushes it out, around the optical axis. The velocity of the electron now has an additional circumferential component. Due to this, a force will push the electron towards the optical axis. When reaching the lower part of the lens, opposite forces causes the circumferential motion to stop. Overall, electrons coming with an angle passing the magnetic lens in a helical trajectory and are drawn towards the optical axis. Thus, like in a typical focusing lens, an incident divergent beam exits the lens as a convergent beam. A simplified illustration of an electromagnetic lens including the electron's trajectory is shown in Fig. 2.16.

In an EM, multiple magnetic lenses are used. However, each lens comes with a set of other elements that support its function. The required electron-optical precision is significantly higher than what is feasible during the mechanical assembly of the microscope. In each lens system, thus, a pair of deflector coils that are perpendicular to the passing beam is placed in front of the actual electron lens. The incoming beam, which may not be perfectly parallel and along the optical axis, can be deflected to compensate for shifts and tilts. By doing so, the perfect entrance in the actual lens can be guaranteed despite imperfections caused, e.g. by the mechanical assembly. Of course, the magnetic lens itself may also be imperfect. For example, differences in the wire thicknesses can cause asymmetry in the magnetic field. The resulting stigmatic lens focuses stronger along one axis which negatively affects the quality of the image. Therefore, coils that are known as stigmators are located behind the magnetic lens to correct for imperfections of the lens symmetry. The last element of the lens system is an aperture. As in OM, aberrations increase with the distance from the optical axis. Thus, the aperture blocks parts of the beam that are far off axis.

In aberration corrected microscopes, an additional lens system is arranged in series with the objective lens. As mentioned above, geometric aberrations are unavoidable in static, rotationally symmetric lenses.[138] However, the use of e.g. hexapole-lenses can compensate for the positive spherical aberration of the objective lens.

Image formation and detection

In CTEM, the illumination system (i.e. the condenser lenses) illuminates an area of the specimen (see Fig. 2.15). Different scenarios can occur when the electron beam interacts with the specimen. The electron can leave the specimen without any interaction as an unscattered primary electron. On the other hand, inelastic scattering can occur. The incoming electron loses energy in the specimen and thereby creating for example secondary electrons or X-rays. In addition, the electron beam can interact elastically and leaves the specimen, usually under high scattering angles, without the loose of energy.

CTEM uses the signal arising from the interference of narrow-angle elastic or inelastic primary electrons and unscattered electrons to create a magnified image of the sample. As electrons can not be seen with the bare eye, the magnified image of the specimen is put onto a viewing screen, which is coated with a material that emits visible light when being exposed to electrons (e.g. silver doped zinc sulfide). For recording, early microscopes used photographic films. In contrast, today a thin scintillator converts the electron signal into photons. The scintillator is fiber-coupled to a charge coupled device (CCD) or complementary metal oxide semiconductor (CMOS) camera to record the images.

For the contrast mechanism in CTEM, a distinction is made between amplitude and phase contrast. The former occurs in samples with high density objects: Stronger scattering at these objects results in less electrons contributing to the image. However, for high-resolution transmission electron microscopy (HRTEM) where thin samples are used, which of course is applicable to 2D material, phase contrast is the important mechanism. To understand phase contrast, the electron beam has to be considered as an electron wave.

The wavelength of an electron in free space is given by the De Broglie wavelength

$$\lambda = \frac{\mathrm{h}}{p} = \frac{\mathrm{h}}{m_0 v} \quad , \tag{2.1}$$

where p is the momentum of the electron and h the Planck's constant. The momentum can be replaced by the mass of the electron m_0 and its velocity v. For an electron accelerated by the voltage U_0, the kinetic energy is:

$$eU_0 = \frac{1}{2} m v^2 \quad . \tag{2.2}$$

Thus, with Eq. (2.1) and Eq. (2.2), the non-relativistic wavelength of an electron traveling in free space can be calculated as

$$\lambda = \frac{h}{\sqrt{2meU_0}} \quad . \tag{2.3}$$

In contrast, the wavelength λ_m of an electron inside of the potential Φ of a material is given by:[146]

$$\lambda_m = \frac{h}{\sqrt{p^2 + 2me_0\Phi(x,y,z)}} = \frac{h}{\sqrt{2me(U_0 + \Phi(x,y,z))}} \quad . \tag{2.4}$$

The potential Φ represents the specimen, e.g. the crystal periodicity, and can therefore vary across the specimen, i.e. $\Phi = \Phi(x,y,z)$. Importantly, the wavelength for electrons in matter is reduced compared to electrons traveling in free space. Thus, a phase shift ϕ can be calculated for an electron wave passing a crystal layer with thickness dz:[146]

$$\phi(x,y,z) = 2\pi \left(\frac{dz}{\lambda_m} - \frac{dz}{\lambda} \right) = 2\pi \frac{dz}{\lambda} \left(\sqrt{1 + \frac{\Phi}{U_0}} - 1 \right) \quad . \tag{2.5}$$

Under the assumption that the potential is constant along the z-direction and $\Phi \ll U_0$, the phase shift for a specimen with thickness t is[146]

$$\phi(x,y) = \frac{\pi t}{\lambda U_0} \Phi(x,y) \quad . \tag{2.6}$$

This means that the incoming plane electron wave is modulated by the potential Φ of the specimen.

Interference with the diffracted wave, converts the phase modulation into a detectable amplitude variation. For an ideal imaging system, however, no phase shift occurs between the primary beam and the diffracted waves. In TEM, a phase shift is generated by residual spherical aberration C_s and intentional defocusing Δf by the operator. In addition, the phase difference depends on the scattering angle and therefore according to Bragg's law on the lattice distance d:

$$\phi = \phi\left(\theta, C_s, \Delta f\right) = \phi(d, C_s, \Delta f) \quad . \tag{2.7}$$

Thus, for a given lattice distance, the phase shift can be adjusted to have constructive interference and therefore high contrast in the image by choosing an appropriate defocus. However, for the same defocus, the phase shift for another lattice distance is different, resulting in less contrast, no contrast or even inverted contrast. The dependence of the image contrast on the lattice distance and structure size is given by the phase contrast transfer function (CTF):

$$CTF(q) = \sin\left(-\pi\Delta f\lambda q^2 + \frac{1}{2}\pi C_s\lambda^3 q^4\right)\cdot\exp\left(-\pi^2 C_c^2\left(\frac{\Delta E}{U_0}\right)^2\lambda^2 q^4\right) \quad , \tag{2.8}$$

with $q = 1/d$ as the reciprocal length of the lattice, i.e. the lattice frequency. The contrast transfer is damped for higher frequencies due to the chromatic aberration C_c and the energy spread of the electron gun ΔE. Spatial incoherence caused by the finite size of the electron gun results in an additional damping envelope. However, in modern microscopes this spatial envelope plays a minor role and is therefore not considered in Eq. (2.8).[147]

In Fig. 2.17 the phase transfer is plotted for three defocus values. For the defocus of 450 nm, the influence of the varying transferred contrast is illustrated. Depending on the lattice frequency, which is represented by the distance of the two stars, their contrast varies from dark over zero to bright. Direct interpretation of a TEM image is therefore only possible for frequencies up to the first zero crossing of the contrast. The best imaging conditions, i.e. the first zero crossing at the highest possible frequency, arise when imaging at the so called Scherzer defocus ($\Delta f_{\mathrm{Sch}} = 1.2\sqrt{C_s\lambda}$) as can be seen in Fig. 2.17 C.[146]

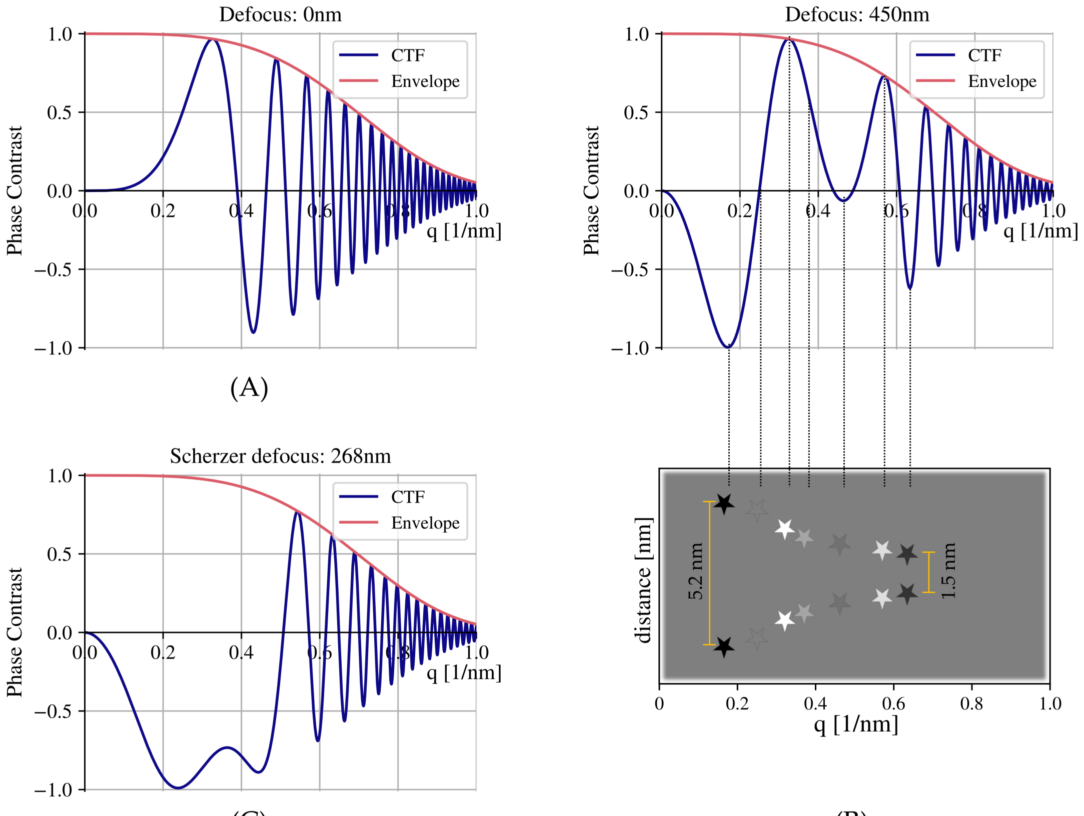

(A)

(C)

(B)

Figure 2.17: (A-C) Calculated contrast transfer function for different defocus values. (B) For a defocus of 450 nm, the resulting contrast is illustrated in the grayscale image for stars with varying distances, representing different lattice constants. (C) In the Scherzer defocus, the first zero crossing of the contrast occurs at the highest possible frequency, giving the optimum imaging conditions.

2.4.2 Scanning Transmission Electron Microscopy

The first variation from CTEM has been invented by Manfred von Ardenne already in 1938.[148] Instead of illuminating a large area on the specimen simultaneously, in scanning transmission electron microscopy (STEM) the electron beam is focused to a small probe on the sample and scanned over a region of interest point-by-point. At each point, the electron beam interacts with the specimen generating a signal that is detected, amplified and finally displayed on a computer display for the corresponding point. A schematic of a STEM including various detectors is shown in Fig. 2.18.

In STEM, the resolution is determined by the achievable probe size of the focused electron beam, as well as other factors such as the interaction volume in the sample. In modern microscopes, aberration correctors in the illumination system can be used to reduce aberrations of the electron beam and create probes smaller than 100 pm. Thus, for thin specimens, atomic resolution can be achieved. In contrast to CTEM, where the magnification results from multistage imaging with several lenses, the magnification in STEM is simply determined by the the scan dimension, i.e. the distance between the pixels in the scan. As mentioned above, the interaction between electron beam and specimen creates various types of signals, which can be recorded by using different detectors. For example, depending on the scattering angle, bright-field (BF) or annular dark-field (ADF) detectors collect electrons leaving the specimen under a small or a large angle, respectively. STEM includes also techniques for investigating the chemical composition of the sample such as EDS and EELS: For each scanning point, the characteristic X-rays or the energy loss of the primary electron can be measured. Given the resolution of STEM, atomically resolved elemental maps of the region of interest are possible.

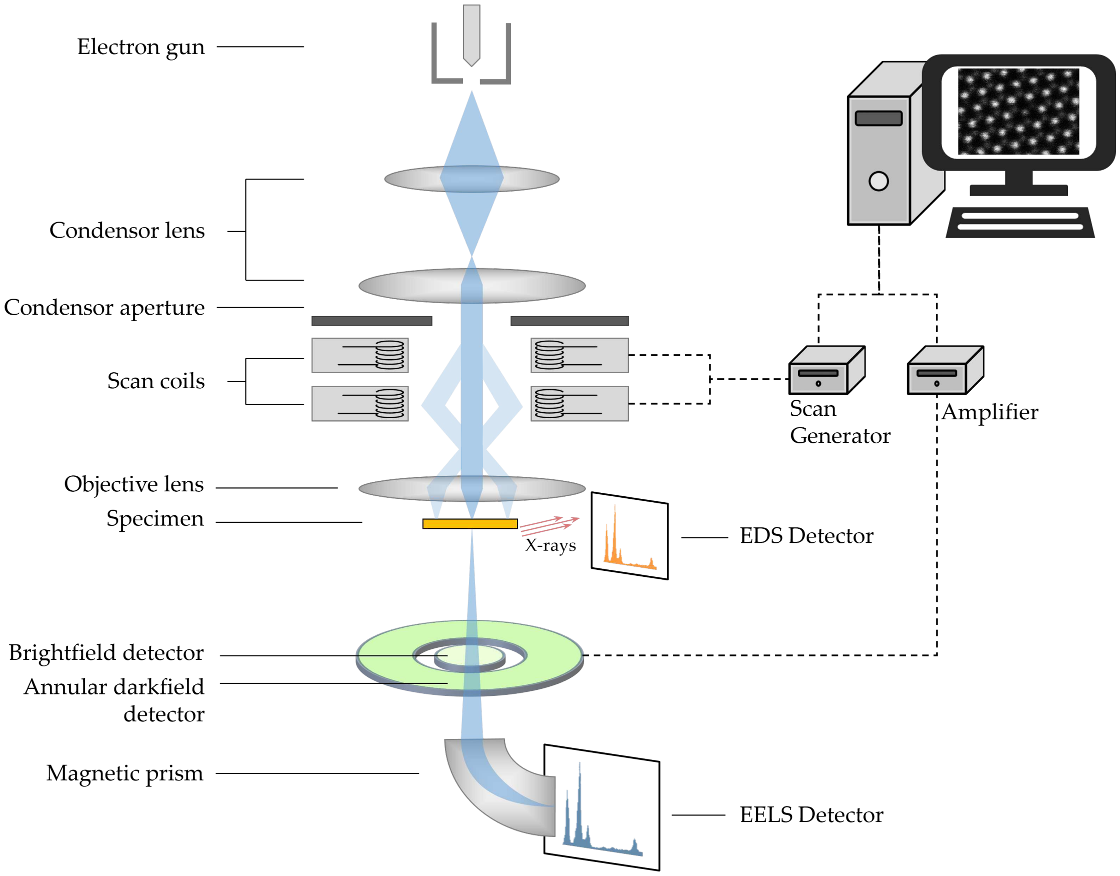

Figure 2.18: Schematic diagram of a scanning transmission electron microscope. The focused electron beam scans the sample, producing signals that can be collected by different detectors and thus creating the image pixel by pixel.

2.4.3 Scanning Electron Microscopy

Beside detecting electrons that transmitted the sample, the signal arising from backscattered and secondary electrons leaving the specimen towards the gun can be recorded by using detectors mounted above the sample. This type of EM has also been described by von Ardenne in 1938.[148] A typical schematic setup of an SEM is shown in Fig. 2.19. Today, dedicated SEMs are used in order to investigate the surface of bulk samples and thus eliminate the need for the time-consuming preparation of thin TEM samples. They are typically operated at acceleration voltages between 0.5 - 30 kV. The resolution of an SEM is limited by several factors: On the one hand, the usage of relatively low electron energies as well as large working distances (i.e. distance between last lens and the specimen) result in probe diameters of about 1 - 10 nm. On the other hand, for a bulk sample, the

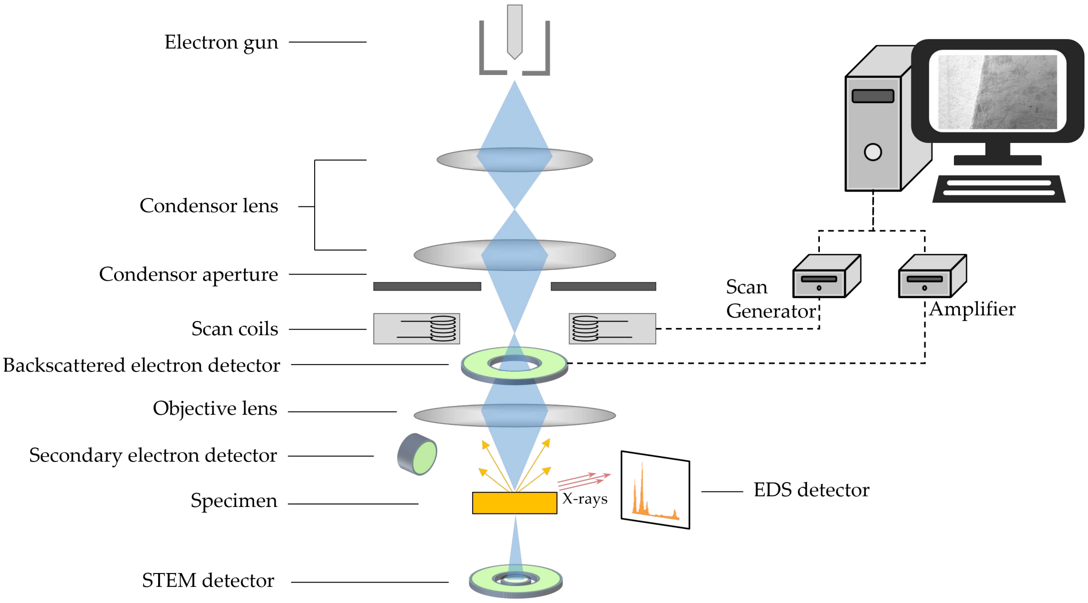

Figure 2.19: Schematic diagram of a scanning electron microscope. With the exception of the STEM detector, the signal is collected above the sample. This allows thick samples to be examined.

excited area is significantly larger compared to a thin TEM sample and thus, the origin of the created signal is no longer restricted to the location of the electron beam.

As in STEM, various detectors can be used to record the signal arising from the interaction between the electron beam and the specimen and thereby creating different type of contrast, i.e. topological or material contrast. For thin specimens, a detector below the sample can be used to image transmitted electrons. SEMs can be equipped with an EDS detector in order to investigate the chemical composition of the material.

2.4.4 Holography and Phase Plates in Electron Microscopy

The improvement of electromagnetic lenses including their power supplies and the associated realization of aberration correction have been a key to the success of electron microscopy. However, electromagnetic lenses can not create arbitrary wavefronts, thus limiting the possibilities regarding controlled electron beam shaping.[149] Phase plates (PPs) are other optical elements regularly used in OM, but becoming less common in EM.

In CTEM, for an ideal lens without aberrations ($C_s = C_c = 0$) at zero defocus, no contrast is transferred from the specimen to the image as can be seen from Eq. (2.8). PPs can be used to overcome this problem to enable in-focus imaging by enhancing the image contrast. The PP is inserted in the back-focal plane of the objective lens to apply a phase shift between the diffracted beam and the direct beam. Therefore, mainly either thin-film or electrostatic PPs are used. The former consists of a thin-film material, which thickness is adjusted so that a certain phase shift is applied to the diffracted beam due to the mean inner potential U_i of the material. The required thickness t for a phase shift ϕ can be calculated as follows:[144]

$$\phi = \frac{2\pi}{\lambda}\frac{eU_i}{E}\frac{E_0+E}{2E_0+E}t \quad \Leftrightarrow \quad t = \phi\frac{\lambda}{2\pi}\frac{E}{eU_i}\frac{2E_0+E}{E_0+E} \quad . \tag{2.9}$$

Here, E is the energy of electron accelerated by the voltage U_0 (i.e. $E = eU_0$) and $E_0 = m_e c^2$ is the electron rest mass energy. In the typical design, called a Zernike PP, the thin film has a hole in the center that allows the direct beam to pass unchanged, thus creating the phase difference.[150] The Hilbert PP, an alternative design, covers half of the back-focal plane and thereby creates an enhanced topological contrast. The exact mathematical derivation of the contrast enhancement can be found e.g. in Malac et al.[151]. The typical PP based on thin films have several drawbacks, such as the sharp onset of the phase shift, which can lead to image artifacts. However, efforts have been done to fabricate phase plates with tapered edges to provide a smooth onset.[152,153] Other drawbacks are contamination and aging of the material, which can hardly be avoided. Therefore, special holders can be used that allow easy replacement of the phase plate via load locks.[154]

Electrostatic phase plates, such as the Börsch PP,[155] create an electrostatic field through which the direct beam is directed and phase shifted relative to the diffracted beams. Their design makes them tunable by adjusting the field strength, but complex to manufacture. In addition, a significant part of the beam is blocked, which can result in image artifacts and low signals.

Phase plates can also be of interest for scanning electron microscopy techniques. Instead of rastering a simple focused electron probe across the specimen, other geometries can enable advanced techniques. Again, OM can serve as an example, having succeeded in overcoming the optical resolution limit by inventing techniques like stimulated emission depletion (STED) microscopy.[156]

The generation of complex electron probes can be realized with phase plates. The underlying idea is similar to that of holography, which is briefly introduced in the following. Electron holography is a microscopy technique that obtains information about the phase shift of the electron wave passing through the specimen. This information is usually lost in electron microscopy when recording the image using conventional films or detectors. Holography is a two step process, illustrated in Fig. 2.20. First, the object is illuminated with the reference wave. The interference

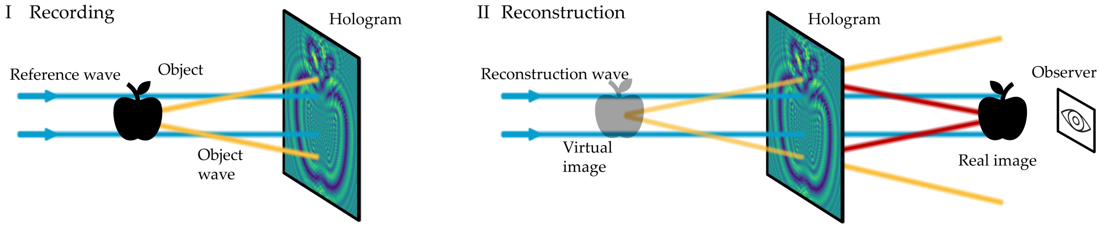

(A) In-line holography

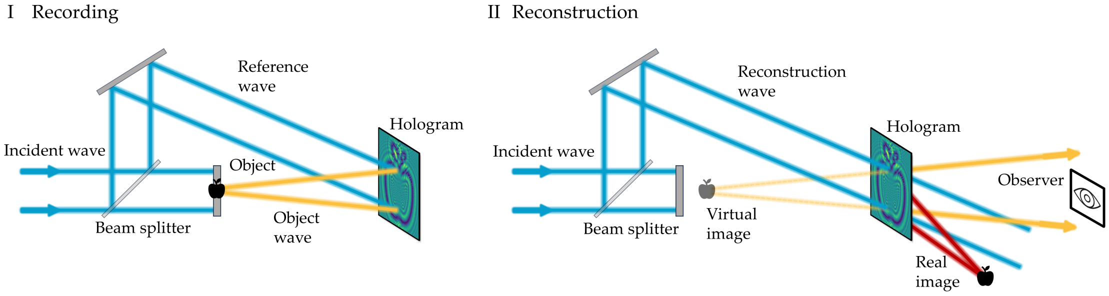

(B) Off-axis holography

Figure 2.20: Electron holography. The interference pattern between a reference wave and the created object wave is recorded, forming the hologram. The hologram contains the three-dimensional phase information of the object. In a second step, an image of the object can be reconstructed by illuminating the hologram. (A) With in-line holography, which is invented by Dennis Gabor and honoured with the Nobel Prize in Physics in 1971, the twin images are created on one axis, resulting in a reduced image quality. (B) Off-axis holography can be used to separate the real and the virtual image. Concept taken from Poon & Liu[158].

pattern between the scattered wave (i.e. the object wave) and the reference wave is recorded to create the hologram. The hologram contains the three-dimensional phase information of the object and is used to reconstruct the object in the second step. Illuminating the hologram with the reconstruction wave generates a real and virtual image of the original object.

Two experimental setups can be used for holography.[157] In its original form, called in-line holography (Fig. 2.20 A), the virtual and the real images are on the same axis as the reconstruction wave, leading to a deterioration in the quality of the reconstruction. This is overcome by off-axis holography, which separates the two images, as shown in Fig. 2.20 B. Nowadays, a three-dimensional reconstruction of the object is often done on a computer, which is why it is called digital holography.

In addition, the hologram itself can be computer-generated. Thus, any desired reconstructed wave can be designed. This allows tailor-made electron beams to be formed by manufacturing the hologram as a phase object and then applying a proper illumination. In the simplest case, the setup for applying this holographic phase plate is similar to the reconstruction of the hologram in the in-line holography (see Fig. 2.20 A). Different Hermite-Gauss modes and even the institute logo as an electron beam have already been produced using computer-generated holograms fabricated with thin-film materials.[159,160] As each portion of the hologram contains information about the entire object, small imperfections in the fabricated phase plate have only little effect on the reconstructed wave, making hologram-based waveforming a robust method.

For the application in electron microscopy, electron vortex beams are of great interest. They are the equivalent to optical vortices that have been used extensively in various optical microscopy methods.[161] Vortex beams possess a doughnut-like intensity distribution and a radially changing phase. The phase difference of one revolution can be a multiple of 2π and defines the orbital angular momentum (OAM) of the vortex. Several methods have been used to realize electron vortex beams. As shown Fig. 2.21 A and B, Y-dislocations as diffraction gratings create a series of vortices with different OAMs corresponding to the diffraction order. Both naturally occurring dislocations (e.g. in the crystal structure)[162] and manufactured dislocations are suitable.[163,164] Spiral phase plates can generate a single vortex beam with a defined OAM (see Fig. 2.21 C). Usually they are fabricated with lithographic techniques[166], but also a natural spiral phase plate from stacked graphite sheets has been used.[167] Moreoever, programmable phase plates based on applying an electrostatic field to introduce a phase shift allow the creation of various beam shapes such as vortices.[149]

Typically, the phase plates are placed inside of the illumination path of the electron microscope, and with the help of the condenser lens system, the modified electron beam is focused to a small electron probe, which can be scanned over the specimen. This can potentially be applied for local magnetic measurements. For example, a change in the OAM of the vortex probe due to the interaction with the magnetic specimen could be analyzed by comparison with a reference wave or a so-called OAM analyzer.[168] The former technique has been successfully applied for a quantitative measurement of the out-of-plane magnetic field of a magnetic pillar.[169] In addition, a difference in the EELS spectrum of a ferrum sample could be shown using left- and righthanded vortices.[163] However, the experimental realization of high-resolution mapping of magnetic materials is still challenging.[170]

Furthermore, electron vortices could provide angular momentum on the atomic level for the manipulation of material, similar to the application of vortices in optical tweezers.[171,172]

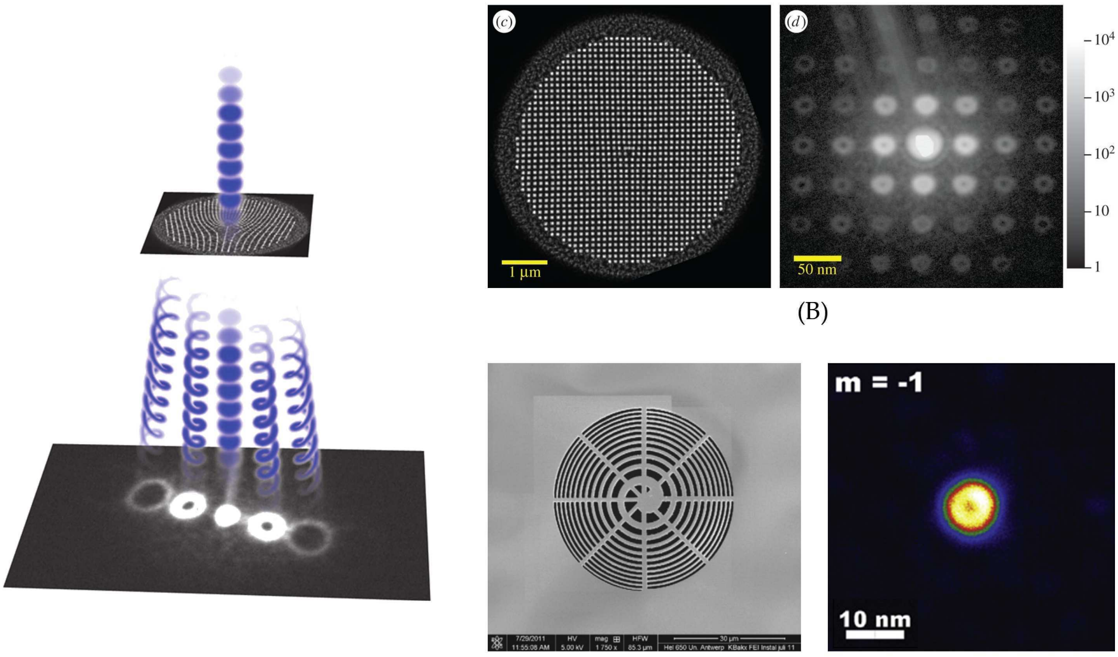

(A)

(B)

(C)

Figure 2.21: Formation of electron vortices. (A,B) Y-dislocations can be used as diffraction grating, generating a set of vortices with different OAMs. (C) A spiral phase plate is fabricated and used as hologram in an in-line holography setup to create a single electron vortex. Reprinted with permission from (A) McMorran et al.[164], (B) McMorran et al.[165], and (C) Verbeeck et al.[166]

2.5 Electron Beam Damage

Electron microscopy images are the result of the interaction between the beam electrons and the specimen material. However, the interaction can also cause sample modifications known as electron beam damage, which can be either permanent or temporary. A variety of damaging effects can occur, depending on a number of factors such as the material and thickness of the specimen, the energy and dose of the electron beam, and other environmental parameters such as the microscope pressure and the specimen temperature.

Heating and Electrostatic Charging

For inelastic scattering, most of the transferred energy results in generated heat and leads to a local increase of the specimen temperature.[144] The heating is negligible for materials with good thermal conductivity. However, for other materials and also for thin films where the heat dissipation is restricted, heating due to electron irradiation can damage the specimen.[173] Reducing the beam current as well as using a good thermal conductive coating can reduce the temperature rise of the sample.[174]

Electrostatic charging of the observed area arises from unbalanced charges in the specimen, i.e. the incoming electrons (incident beam) and the outgoing electrons (backscattered, secondary electrons) create a residual net charge. Typically, the specimen is grounded through the sample holder, however, insulating materials do not discharge sufficiently. Electrostatic charging affects the imaging, but can also cause mechanical forces and specimen damage.[175]

Radiolysis

Another type of beam damage is radiolysis, which is sometimes referred to as ionization damage. Radiolysis can occur for both organic as well as inorganic materials, but the exact mechanism for damaging the specimen varies. For organic materials, the incoming electrons can excite the specimen electrons and thereby break chemical bonds.[175] In this way, polymer fragments are created or, if the electron irradiation generates reactive species, cross-linked polymers can be formed.[143] Either way, the original structure of the specimen is damaged.

For inorganic materials the exact mechanism is highly dependent on the material. E.g. in transition-metal oxides, inner-shell vacancies in the metal can be created followed by an interatomic Auger decay from the oxygen atom. As a result, the neutral or positive oxygen atom is repelled by the metal ion and pushed into vacuum.[176]

In ionic materials, interband transitions can be caused by the incoming electrons. After recombination, an anion vacancy and a cation interstitial are eventually formed, changing the initial structure and composition of the material.[143]

Radiolysis can be reduced e.g. by using low-dose techniques or choosing a higher acceleration voltage, as the inelastic scattering cross section decreases with increasing incident electron energy.[177]

Hydrocarbon Contamination

The specimen can also be damaged by the deposition of contamination during the electron beam irradiation. Incoming and outgoing electrons can polymerize mobile hydrocarbon molecules, which diffuse on the specimen surface, forming a layer of fixated carbon contamination. The resulting concentration gradient of mobile species causes more contaminants to diffuse towards the illuminated area.[146] Depending on the electron energy, exposure time and type of illumination, the contamination layer can be tens of nanometers thick.[178] Especially when studying 2D materials with low atomic numbers, the contamination layer prevents high-resolution imaging. The hydrocarbons originate from microscope components, e.g. pump oils, vacuum greases and seals, but also from the specimen itself as a result of the preparation, storage and transfer.[175]

While in some cases the growth of contamination is an undesired process, the effect can also be used as a contamination lithography and intended deposition, which will be described in more detail below.

Atomic Displacement and Sputtering

Although the electron mass is significantly smaller than the mass of the atomic nuclei, elastic scattering processes can also cause damage to the specimen by displacing atoms from the crystal lattice to interstitial positions. Atomic displacement is also referred to as knock-on damage. An electron which is deflected by the Coulomb potential of the nuclei transfers the energy E_{t} during the scattering process. The energy E_{t} depends on the scattering angle θ, the incident electron energy E and the atomic mass number m_n and can be calculated as[179]

$$E_{\mathrm{t}}(\theta) = E_{\mathrm{t,max}} \sin^2\left({}^{\theta}\!/\!{}_{2}\right) \quad , \tag{2.10}$$

with

$$E_{\mathrm{t,max}} = \frac{2m_nE\left(E + 2m_ec^2\right)}{\left(m_n + m_e\right)^2 c^2 + 2m_nE} \quad , \tag{2.11}$$

where m_e is the electron mass and c the speed of light. With the approximations $m_n \gg m_e$ and $m_n c^2 \gg E$, the maximum transferred energy can be expressed as[180]

$$E_{\mathrm{t,max}} = \frac{2E(E + 2m_e c^2)}{m_n c^2} \quad . \tag{2.12}$$

As can be seen from Equation (2.10), the transferred energy increases for large scattering angles, with the maximum energy $E_{\mathrm{t}} = E_{\mathrm{t,max}}$ for $\theta = 180°$.

The energy required to displace an atom in the specimen is called the displacement energy E_{d}, which depends on the specimen material, i.e. bond strength, atomic weight, etc. At room temperature, the displacement energy for graphite is 25 eV.[181] From Equation (2.12), the threshold of the incident electron energy for atomic displacement can be calculated. Thus, for the given E_{d} of graphite, incident electrons with $E > 125\,\mathrm{keV}$ can lead to beam damage in terms of atomic displacement.

For an atom at the surface of the specimen, less energy is required to displace the atom. In contrast to an atom inside the material, which is displaced to an unfavorable, interstitial position, a surface atom can easily escape from the specimen and enter the vacuum of the microscope. This type of beam damage is called electron beam sputtering and is particularly severe for 2D material where all the atoms are surface atoms. Sputtering occurs when the incident beam electrons transfer enough energy to break the covalent bonds of the specimen material.[180] For graphene, the required transferred energy is about 23 eV, which results in an expected knock-on threshold of approximately 110 keV. However, knock-on damage in graphene can already be observed for incident energies of 86 keV. The reduced energy threshold can be explained by an oscillation of the atom parallel to the incoming electron beam, which allows a higher transferred energy $E_{\mathrm{t,max}}$ compared to a static atom.[180]

The cross section for Coloumb scattering of the incident electron at the atomic nuclei is originally derived by Mott[182] and approximated by McKinley and Feshbach:[183]

$$\begin{aligned}\sigma_D =& \frac{4Z^2E_R^2}{m_e^2c^4}\left(\frac{E_{\mathrm{t,max}}}{E_{\mathrm{d}}}\right)\pi a_0^2\left(\frac{1-\beta^2}{\beta^4}\right)\\ &\left\{1 + 2\pi\alpha\beta\sqrt{\frac{E_{\mathrm{d}}}{E_{\mathrm{t,max}}}} - \frac{E_{\mathrm{d}}}{E_{\mathrm{t,max}}}\left[1 + 2\pi\alpha\beta + (\beta^2 + \pi\alpha\beta)\ln\left(\frac{E_{\mathrm{t,max}}}{E_{\mathrm{d}}}\right)\right]\right\}\end{aligned} \tag{2.13}$$

This expression is true for the static lattice approximation. However, a more accurate knock-on damage cross section can be obtained by considering atom oscillations.[180]

Fig. 2.22 A shows the calculated knock-on cross sections for graphene for both the static and the dynamic model, i.e. considering oscillations. The data is calculated using the script provided by Meyer et al.[184]. The blue curve shows the cross section in the static lattice approximation with a sharp onset. In contrast, the modified cross section (yellow line) exhibits a smooth increase and explains the observed knock-on damage for carbon in graphene for slightly smaller incident beam energies. Thus, the modified cross section considering also atom vibrations should be taken into account particularly for incident energies close to the knock-on threshold. For higher energies, it is sufficient to use the static lattice approximation to calculate the knock-on damage cross section.

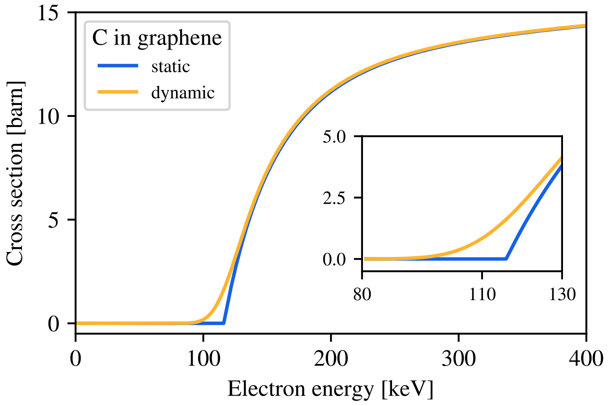

(A) Carbon atom in graphene.

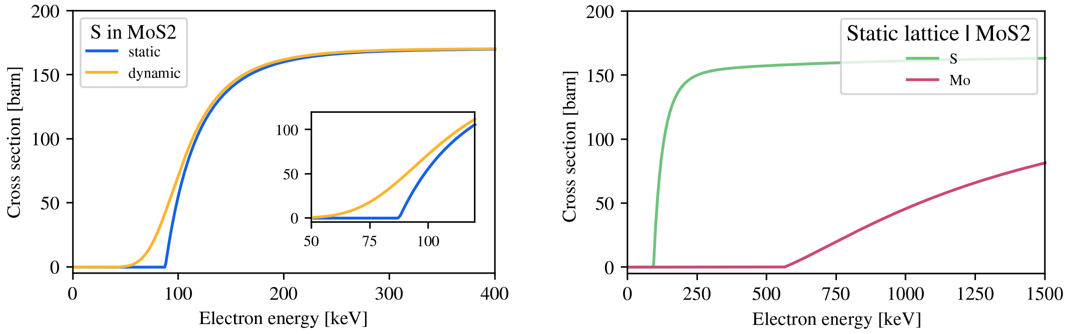

(B) Sulfur atom in MoS_2. **(C)** Sulfur and molybdenum in MoS_2.

Figure 2.22: Knock-on cross sections calculated for different 2D materials. (A) Considering the dynamic model, knock-on damage for the carbon atoms in graphene starts with electron energies higher than 86 keV. (B) and (C) Comparison of the knock-on damage in MoS_2 for the different models and the two different atom species, respectively.

In Fig. 2.22 B, the comparison for the static and the dynamic model is given for the sulfur atom in MoS_2. The same deviation for the two models can be observed. In contrast to carbon in graphene, sulfur atoms can be knocked-out even at electron energies below 80 keV.

For the two atom species (sulfur and molybdenum) in MoS_2, the knock-on cross section is given in Fig. 2.22 C. As can be seen, the threshold for molybdenum (red curve) is at significantly higher electron energies compared to sulfur (green curve) and well beyond the typical energies used in modern TEMs. Thus, in the case of knock-on damage in TMDs, the radiation damage is initiated with the creation of the light chalcogen atoms and then followed by further degradation of the already damaged material.[185]

Beam Damage as Tool for Nanopatterning

When investigating the material structure of a specimen, beam damage in electron microscopy is obviously a problem that needs to be avoided. However, the spatially resolved modifications due to the damage can also be used to intentionally pattern the material. The idea is rather simple: The pattern of interest can directly be transferred into the specimen by controlled placement of the electron beam at specific positions or tracks. The ability to form a small electron probe enables patterns and modifications on the nanometer scale, and with aberration correction even down to the atomic level.[44,186,187] Importantly, no photo resist is necessary for this direct-write lithography method. As a result, the possible resolution surpasses that of classical, resist-based electron beam lithography.[188] Several of the beam damage types described above can be used for patterning.

The deposition of hydrocarbon contamination allows for the creation of patterns by gaining material. The controlled deposition in electron microscope is referred to as electron beam induced deposition (EBID) (see Fig. 2.23 A). Mobile hydrocarbons present on the specimen, as described above, can be exploited for writing structures consisting of carbon.[189] In addition, materials other than carbon such as tungsten, gold and platinum can be deposited by EBID with introducing certain precursors using the gas injection system (GIS) of the microscope.[190,191] Typically, organometallic compounds are used as precursors, which diffuse on the sample surface and decompose under the electron beam irradiation to form a solid deposit containing metal with a high carbon content.

In contrast, the loss of material due to beam damage can also be used for patterning. Related to EBID, but basically the opposite, is electron beam induced etching (EBIE) (see Fig. 2.23 B). The etching is assisted by gasses, which are introduced into the microscope chamber and diffuse on the sample. The gasses decompose under the electron beam forming reactive species, which chemically react with the specimen material.[193] Volatile reaction products are created and

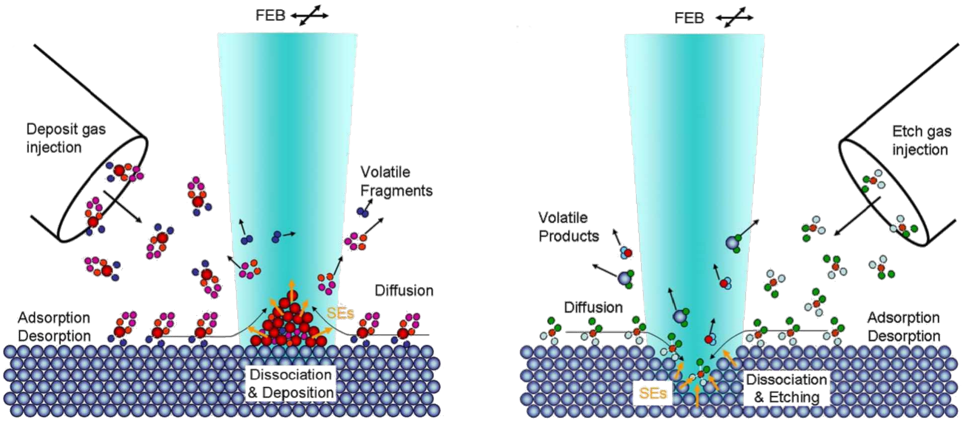

(A) (B)

Figure 2.23: Electron beam induced deposition and etching. In both cases, molecules are injected by the GIS of the microscope and diffuse on the specimen surface. (A) In the case of deposition, the precursor molecules are cracked under the electron beam and polymerise with other molecules. (B) For etching, the electron beam generates reactive species which react with the substrate to form volatile products which are then removed by the vacuum system. In both cases, a concentration gradient causes the injected molecules to diffuse towards the beam. Reprinted with permission from Utke et al.[192]

removed by the vacuum system of the microscope. Different gasses as etching agents can be introduced to etch a variety of specimen materials. For example, water vapor is used to etch organic materials, while XeF_2 has been found to work for silicon-containing materials such as SiO_2, Si_3N_4, and SiC [194] and TMDs.[195] Etching rates in EBIE depend on several parameters such as the partial pressure of the etching agent, the electron energy as well as flux and and gas migration on the sample surface. For a detailed insight into the mechanism and investigations on EBIE, reference is made to the relevant literature, e.g. Utke et al.[192]

Another option for controlled removal of material for patterning is the use of a high energy electron beam for sputtering. As described above, for a given material there is an energy threshold above which the incident electron transfers enough energy to knock out an atom of the specimen. Typical SEMs do not provide sufficient energy, however, (S)TEMs usually use acceleration voltages between 80 and 300 keV. In particular, 2D materials are of great interest for patterning as their extremely thin thickness allows structures with the highest resolution. Modern STEMs with aberration correctors enable direct patterning by sputtering on the atomic level. Nanopores, -bridges, and -gaps have been introduced with 200 and 300 keV electron beams into freestanding graphene without damaging the surrounding crystal lattice.[196,197] Other materials such as TMDs [186,198] and black phosphorus [47] have also been patterned by electron beam sputtering.

Chapter 3

Methods and Materials

3.1 Fabrication and Transfer of 2D Materials

The 2D materials used in this work were either CVD grown or mechanically exfoliated from bulk crystals and transferred onto TEM grids with a perforated carbon support film. The CVD grown materials were obtained from commercial vendors or from academic cooperation partners.

Monolayer graphene was purchased from Graphenea.[199] The "easy-transfer" graphene comes on a paper/water-soluble polymer stack as carrier with another sacrificial layer on top. For transferring, the stack is placed in deionized water. The polymer dissolves, leaving the graphene with the sacrificial layer floating on the surface of the water. The TEM grid is used to pick up the graphene with the sacrificial layer. After annealing for 1 h at 150 °C, the sacrificial layer is dissolved in hot acetone.

In collaboration with Xiao Wang from the School of Physics and Electronics at Hunan University, mono- and few-layers TMDs (MoS_2, WS_2 and WSe_2) are obtained. CVD processes are used to grow the materials on a Si/SiO_2-wafer. The flakes are transferred following the procedure in Meyer et al.[189], which is illustrated in Fig. 3.1. First, the TEM grid is placed on the wafer with the support film facing the 2D material. The grid is positioned and held in place using a Kleindiek piezomanipulator. A drop of isopropyl alcohol is added, and as it evaporates, the surface tension ensures good contact between the TEM grid support film and the 2D material or the wafer, respectively. Contact is further enhanced by annealing on a hot plate for 5 min at 200 °C. An aqueous solution of KOH is used to etch away the SiO_2 layer and thus, leaving the TEM grid with the 2D material floating

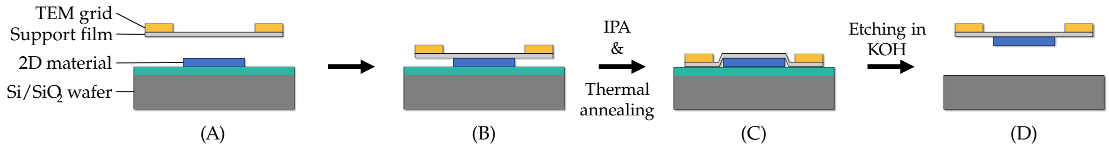

Figure 3.1: Schematic illustration of the transfer of a 2D material flake. (A,B) The TEM grid with the support film is placed on top of the 2D material and the Si/SiO$_2$-wafer. A piezo-manipulator is used to hold the grid in place. (C) Good contact between flake and support film is achieved by surface tension during the evaporation of a droplet of IPA as well as thermal annealing. (D) After etching the SiO$_2$ using KOH, the TEM grid now carrying the 2D material can be removed from the substrate.

on the surface. Finally, the TEM grid is picked up and washed in deionized water and isopropyl alcohol, followed by drying in air.

The "Scotch tape method" is performed to mechanically exfoliate thin sheets from bulk crystals of graphite.[5] In short, the crystal is placed on the tape to peel of a thick piece of the material. Repetitive peeling reduces the number of layers and eventually results in few- and monolayers of the material. The thickness of the flakes is measured by means of atomic force microscopy. Therefore, a Bruker Innova© is used, operated in contact mode. The exfoliated flakes are again transferred to the TEM grid according to the method shown in Fig. 3.1.

Prior to patterning or imaging the transferred 2D material in an electron microscope, the samples are baked-out on a hot plate for 10 - 15 min at 200 °C in order to reduce the amount of hydrocarbon on the specimen.

3.2 Photoluminescence Measurements

The PL measurements are done on two different optical setups. A custom-built inverted microscope of the AG Meixner (Institute of Physical and Theoretical Chemistry, University of Tübingen) operated by Dr. Kai Braun is used for the initial measurements. The other measurements are performed on a Renishaw inVia™ Raman microscope. On both optical microscopes, a 532 nm laser is used for the excitation. The spectral range of the Raman microscope can be adjusted to record the PL spectrum. However, some optical elements of the microscope are not suitable for wavelengths higher than 690 nm. Thus, only the spectral range from 600 - 690 nm is considered.

3.3 Electron Microscopy

3.3.1 Nanopatterning

EBIE is performed in a Zeiss Crossbeam XB1540 equipped with a multi-GIS (Orsay Physics 5-line GIS). For etching graphene, a H_2O reservoir is inserted for water-assisted EBIE. An acceleration voltage of $3\,\mathrm{kV}$ and a beam current of $3\,\mathrm{nA}$ is used with a typical dose per area of about $5\,\mathrm{C\,m^{-1}}$ for patterning. Relatively basic patterns are created using the microscope software (Zeiss SmartSEM).

FIB milling is done in a Zeiss Crossbeam Auriga 40 with a gallium focused ion beam (FIB) from Orsay Physics. Typically, a beam current of $10\,\mathrm{pA}$ is used with an acceleration voltage of $30\,\mathrm{kV}$ for patterning 2D materials. The microscope is equipped with a pattern-generator software (Zeiss Atlas 5), which is used for creating the patterns as well as for scan control during patterning.

Electron beam sputtering is performed on two Jeol JEM ARM200F, one equipped with a probe-corrector (CEOS CESCOR). The microscopes are operated at an acceleration voltage of $200\,\mathrm{kV}$ in order to provide enough energy to overcome the knock-on threshold for the materials used. Within this work, software has been written that allows the structuring of almost arbitrary patterns. The software consists of two parts: A pattern generator which is written in Python, including a graphical user interface (GUI), and a DigitalMicrograph software that provides the scan-control of the STEM during the patterning process. A flowchart for the created software is given in Fig. 3.2.

The pattern generator converts user-defined shapes or imported images into a dictionary of individual points. The dictionary contains the x-y-coordinates as well as a dose for each point. The GUI can be used to visualize the pattern, either by highlighting the points' dose or order (see Fig. 3.3). The user can select specific points individually or as a group to change their dose or doing a variety of other modifications, such as adding or deleting points, creating arrays of patterns, or moving and rotating them. In addition, STEM images can be imported and displayed in the user interface for precise positioning of the pattern on the specimen. The dictionary is exported as a txt-file, again containing all the points in the patterning order with their coordinates and dose. Importantly, in this step the coordinates are translated into the coordinate system of the microscope.

The scan control software reads the created txt-file. During the patterning procedure, the software places the beam on the point coordinates and waits for the given dose before continuing with the next point. By doing so, the pattern is written point after point. For the aberration corrected microscope, which is a dedicated STEM and therefore equipped with Gatan's DigiScan™ system, the scan coils are controlled by the software for positioning the electron beam. On the other

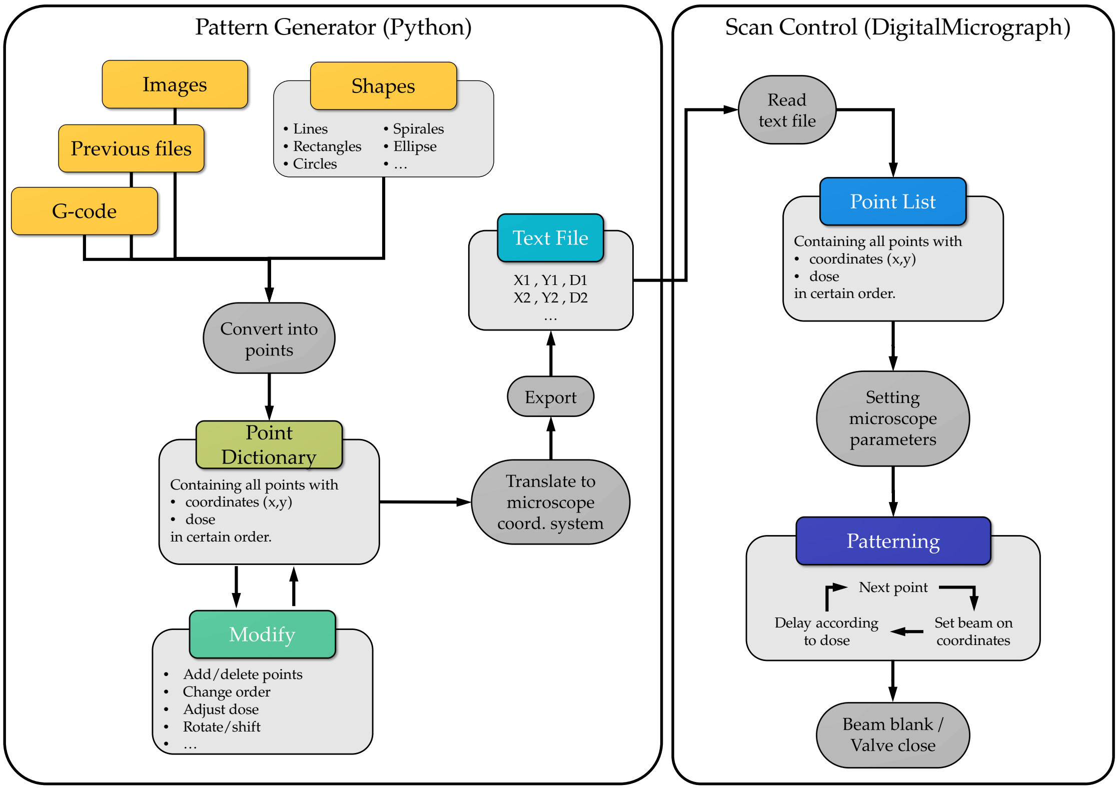

Figure 3.2: Flowchart of the software written for patterning by STEM. The pattern generator with its user interface is used to create the desired pattern and convert it into a list of coordinates. The second part, the DigitalMicrograph script, controls the beam position of the microscope in order to introduce the pattern according to the created point list.

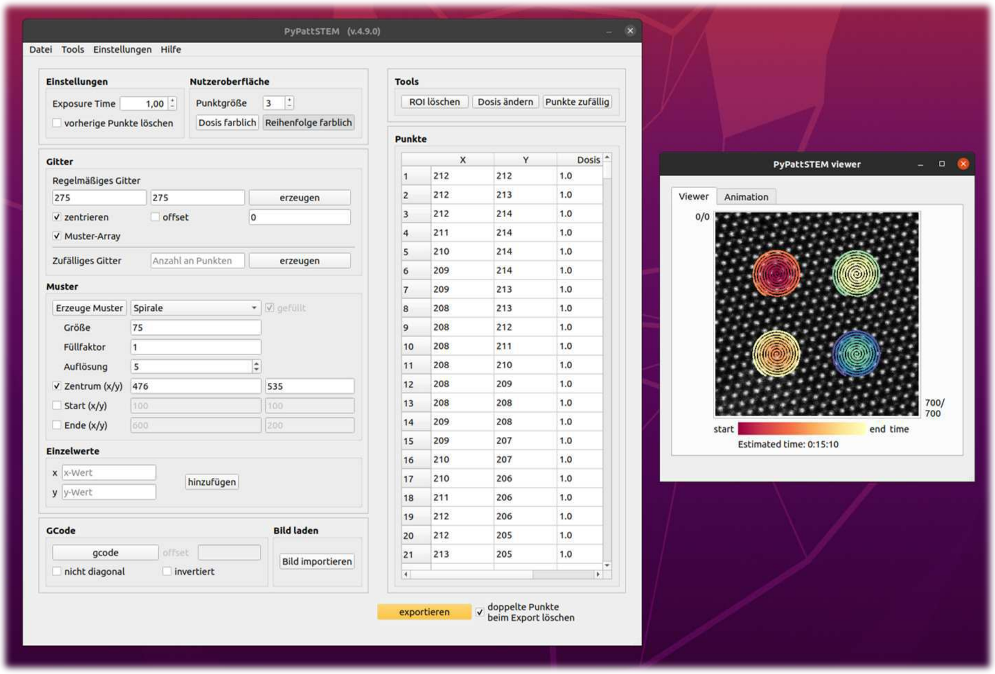

PyPattSTEM (v.4.9.0)

Einstellungen

Exposure Time 1,00

☐ vorherige Punkte löschen

Nutzeroberfläche

Punktgröße 3

Gitter

Regelmäßiges Gitter 275 275

☑ zentrieren ☐ offset 0

☑ Muster-Array

Zufälliges Gitter Anzahl an Punkten

Muster

Erzeuge Muster Spirale ☑ gefüllt

Größe 75

Füllfaktor 1

Auflösung 5

☑ Zentrum (x/y) 476 535

☐ Start (x/y) 100 100

☐ Ende (x/y) 600 200

Einzelwerte

x x-Wert

y y-Wert

GCode

☐ nicht diagonal ☐ invertiert

Punkte

	X	Y	Dosis
1	212	212	1.0
2	212	213	1.0
3	212	214	1.0
4	211	214	1.0
5	210	214	1.0
6	209	214	1.0
7	209	213	1.0
8	208	213	1.0
9	208	212	1.0
10	208	211	1.0
11	208	210	1.0
12	208	209	1.0
13	208	208	1.0
14	209	208	1.0
15	209	207	1.0
16	210	207	1.0
17	210	206	1.0
18	211	206	1.0
19	212	206	1.0
20	212	205	1.0
21	213	205	1.0

☑ doppelte Punkte beim Export löschen

PyPattSTEM viewer

Estimated time: 0:15:10

Figure 3.3: Screenshot of the graphical user interface of the pattern generator that was written in this thesis for patterning with the scanning electron microscope. The shape to be patterned can be generated and modified by the user (left) and visualized as an overlay on the image acquired by the microscope (right).

hand for the non-corrected microscope, the beam shift is used to put the beam on the coordinates. After the patterning process, the electron beam is blanked or the beam valve is closed via the software, leaving the microscope in a safe state and thus allowing e.g. overnight patterning.

3.3.2 TEM for Imaging

Imaging is performed in a Jeol JEM ARM200F TEM equipped with an image-corrector (CEOS CETCOR). To reduce beam damage, an acceleration voltage of 80 kV is used. High-resolution TEM images are recorded in Scherzer defocus.[144] Dark-field TEM is used to highlight crystal orientations in medium magnification images. Therefore, an objective aperture is put into the beam path in the diffraction plane to select one specific diffraction spot. Thus, only electrons scattered in this direction are used for image formation, highlighting the selected lattice orientation.[144]

CHAPTER 4

RESULTS

4.1 Patterning of 2D Materials

4.1.1 Electron Beam Induced Etching

Gas-assisted EBIE was used to introduce structures into 2D materials serving as features and alignment marks for the subsequent stacking.

Some examples of structures that were fabricated into suspended graphene are shown in Fig. 4.1. Holes with diameters up to 100 nm are created by putting the beam on a single spot. By varying the time, the size of the hole can be adjusted. The exact dose required for EBIE is highly dependent on the experimental conditions. The system vacuum, the partial pressure of the precursor gas and the amount of contamination on the specimen affect the etching rate. Putting the beam on a single spot for 3 - 5 s results in hole diameters between 30 and 100 nm. Bigger holes can be created in a more controlled manner by scanning the beam across a circular area. Fig. 4.1 A shows an SEM image of a freestanding graphene membrane. Contamination on the graphene is visible as brighter lines and speckles. In the center, a hole with a radius of 100 nm has been introduced. In the same way, other shapes like circle fragments or a cross are introduced as shown in Fig. 4.1 B and C, respectively. Notably, the carved areas in the center of the cross appear to be stable and do not tend to collapse and fold over, although they are freestanding in two directions, In general, feature sizes down to about 100 nm are reproducibly possible.

As can already be presumed from the minimum feature size and the presented SEM images, the edges of the structures created by EBIE are not flat. Fig. 4.2

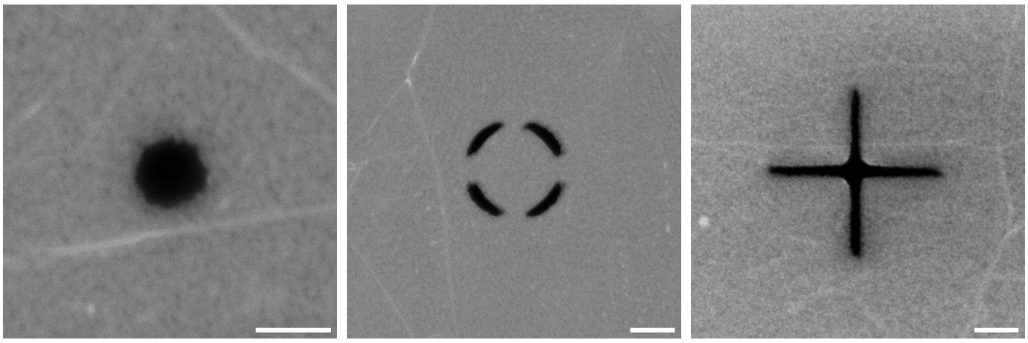
(A) **(B)** **(C)**

Figure 4.1: Different patterns introduced into freestanding graphene by means of EBIE. Scale bars are (A) 250 nm and (B,C) 500 nm. (B,C) Reprinted with permission from Haas et al.[200]

shows a TEM image of such an edge. In fact, it exhibits significant roughness, i.e. wavy edges with indentations of around 10 nm and material aggregations in some areas. The fourier transform (FT) of the image indicates that the crystallinity of the graphene is still preserved next to the removed region. However, amorphous material contaminating the graphene monolayer dominates the image.

The introduced geometries must be designed to provide stability. Completely separated patterns having no support cannot be introduced into the thin membranes. This is demonstrated for a closed ring introduced into graphene (see Fig. 4.3). Initially, an almost freestanding disc is created, supported only by some fragile connections to the outer part. Applying a higher electron dose breaks these supports and causes the disc to collapse and eventually stick either on the surface of the graphene or at the edge of the hole.

In contrast to graphene, TMDs such as WS_2 cannot be patterned by water-assisted EBIE, since the chemical etching process is highly material specific. Fig. 4.4 A shows the attempt to pattern a line across both the suspended WS_2 and the perforated support film. Importantly, the carbon film is significantly thicker (approx. 12 nm[201]) than the WS_2. The cut-through region is only present on the carbon support and not on the WS_2. A slight contrast difference is also visible on the TMD due to etched organic contamination covering the suspended WS_2.

Another example is shown in Fig. 4.4 B. Rather than having a freestanding membrane, few-layer WS_2 is intended to be patterned directly on the supporting film. The carbon support is again completely removed, even below the flake. At first glance, the WS_2 remains intact. Nevertheless, higher-magnified ADF-STEM images reveal that the TMD is affected to a small extent as well. In some areas, thinner regions of the material can be recognized by the darker ADF-contrast. However, even in these areas the crystallinity of the WS_2 is still present.

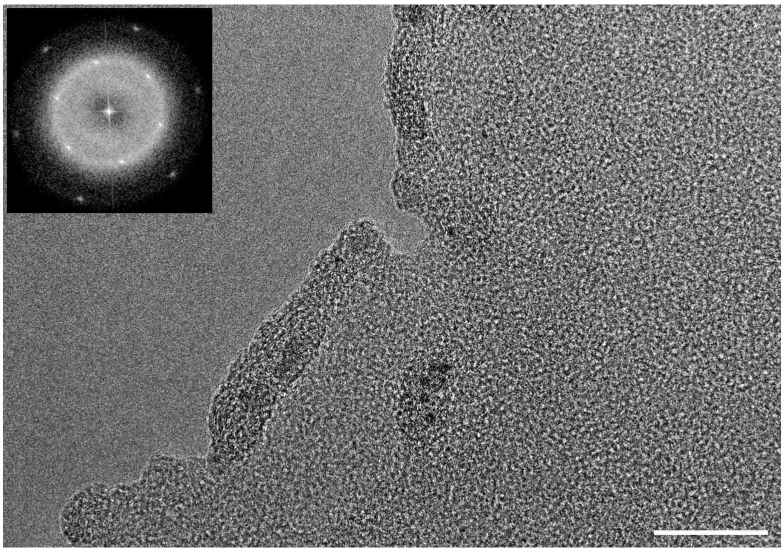

Figure 4.2: TEM image of a graphene edge after patterning by EBIE. Material agglomerations as well as rough edges can be seen close to the edge. Amorphous contamination covers the graphene. However, the crystallinity is preserved even close to the removed region, as can be seen from the FT. Scale bar is 20 nm.

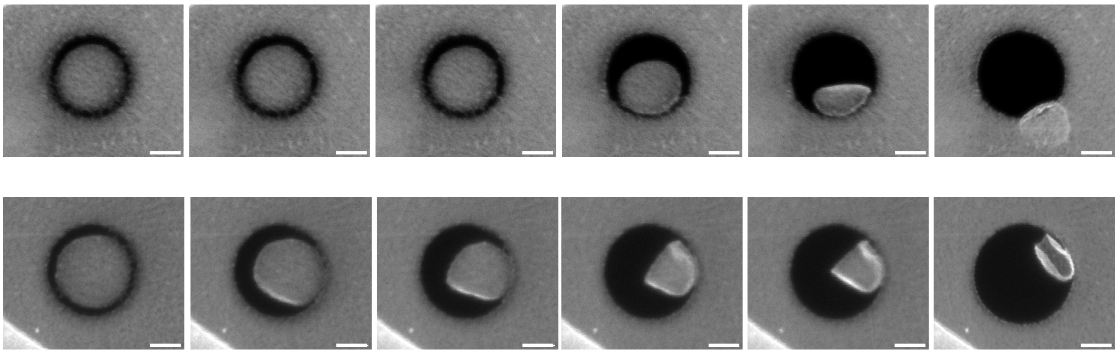

Figure 4.3: Introducing a closed ring into graphene by EBIE. At first, the central disc is still stabilized by remaining material. Additional electron dose lead to either adhering of the disc next to the hole (top row) or rolling up (bottom row). Scale bars are 300 nm. Reprinted with permission from Haas et al.[200]

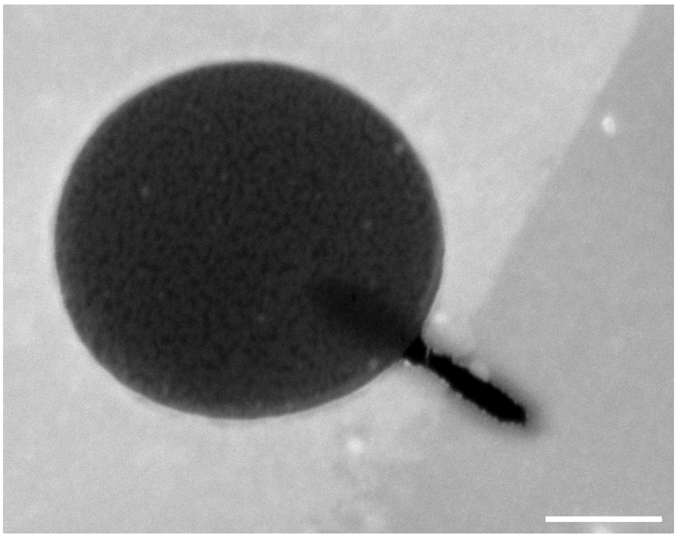

(A)

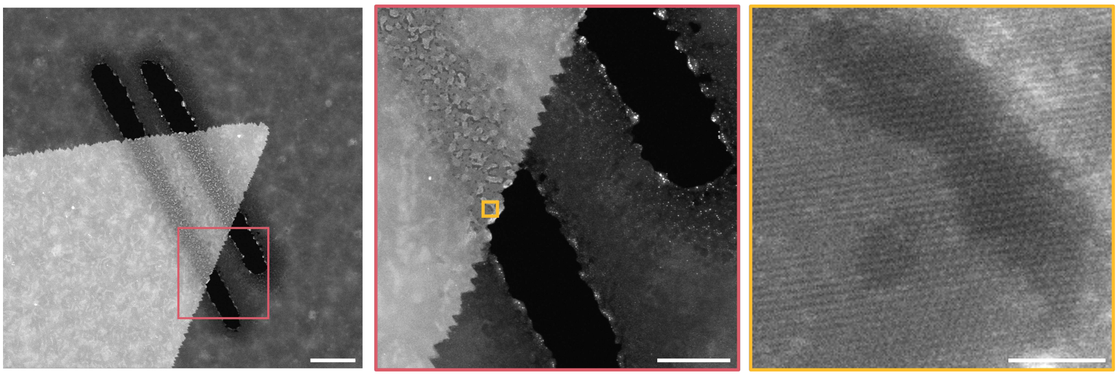

(B)

Figure 4.4: EBIE of WS_2 on amorphous carbon support film. (A) The line is patterned into the support, but not into the freestanding, thinner WS_2. (B) The carbon support is even completely removed under the WS_2 flake. The flake is also slightly damaged, however, the crystallinity of the material is still intact. Scale bars are (A) 500 nm and (B) 250 nm, 100 nm and 3 nm from left to right.

4.1.2 Focused Ion Beam

In addition to patterning with the electron beam of the SEM, the FIB of a cross-beam system was used. Due to the higher mass of the gallium ions, the material removal is significantly increased compared to the SEM. Thus, a low beam current between 1 and 10 pA was applied to introduce patterns into 2D materials and extensive pre-exposure during imaging with the ion beam was avoided. In contrast to EBIE, ion beam milling is a purely physical removal process allowing all types of materials to be patterned.

Example images are shown in Fig. 4.5 A. Freestanding WS_2 is structured with bow-tie like patterns. The remaining material forms a nanoribbon with a reproducible width of 40 nm and a length of up to 400 nm. The maximum achievable stable length has not been tested. However, tearing or collapsing of the strips has not been observed, therefore they can probably be even longer.

The edge of the pattern was examined in more detail using TEM. Material aggregations can only be observed in the patterning direction, which was chosen to be towards the ribbon. In addition, extensive destruction of the material can be seen far from the actual cutting edge. From Fig. 4.5 B, the loss of crystallinity is visible: An approximately 30 - 40 nm wide amorphous rim surrounds the entire introduced patterns. Beyond these regions, the actual crystal structure of WS_2 is still preserved.

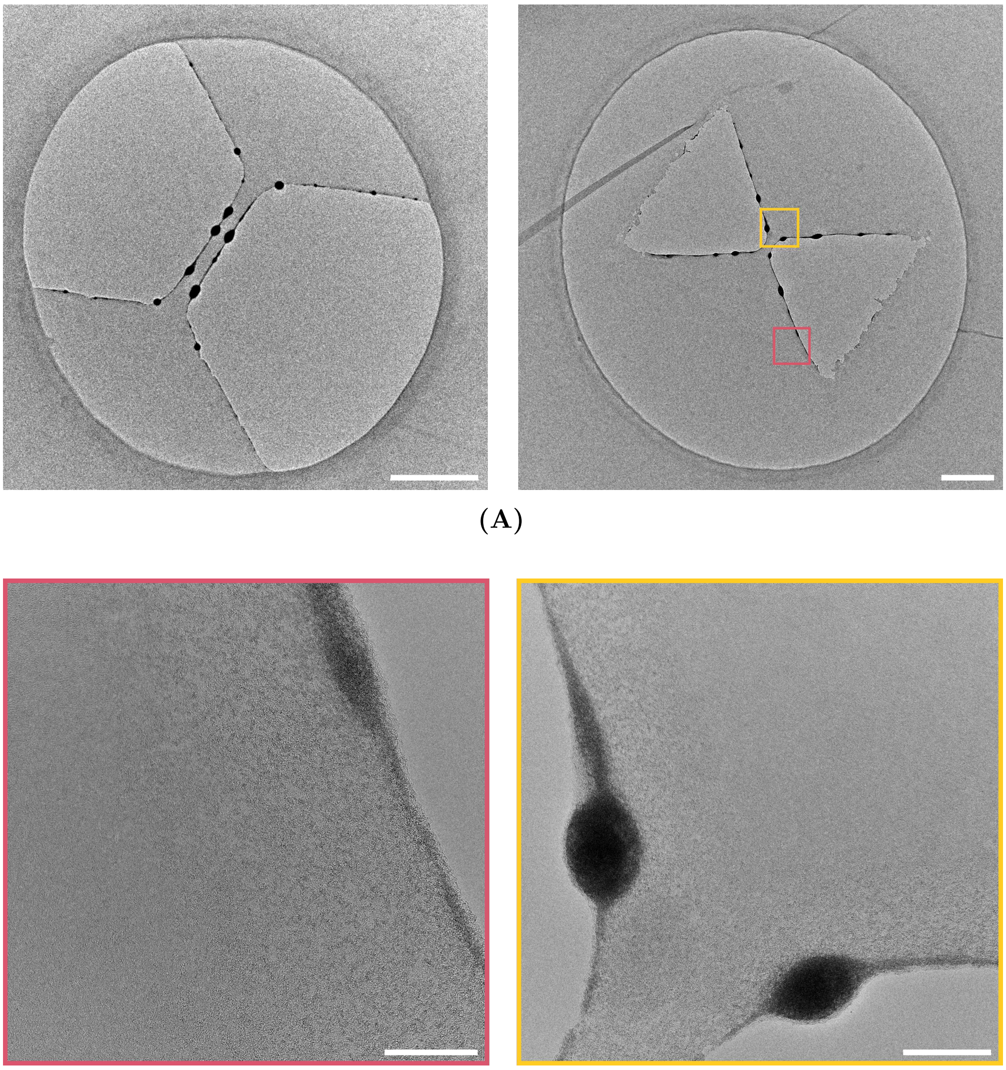

(A)

(B)

Figure 4.5: TEM images of nanoribbons introduced into WS_2 by means of FIB. (A) Overview images show freestanding ribbons as well as material aggregations occuring in the direction of the patterning. (B) In addition, the crystal structure of the material is destroyed even 30 - 40 nm away from the actual edge of the pattern. The position of the higher magnified images are indicated by the colored squares in the overview images. Scale bars are (A) 250 nm and (B) 20 nm and 30 nm for the left and right image, respectively.

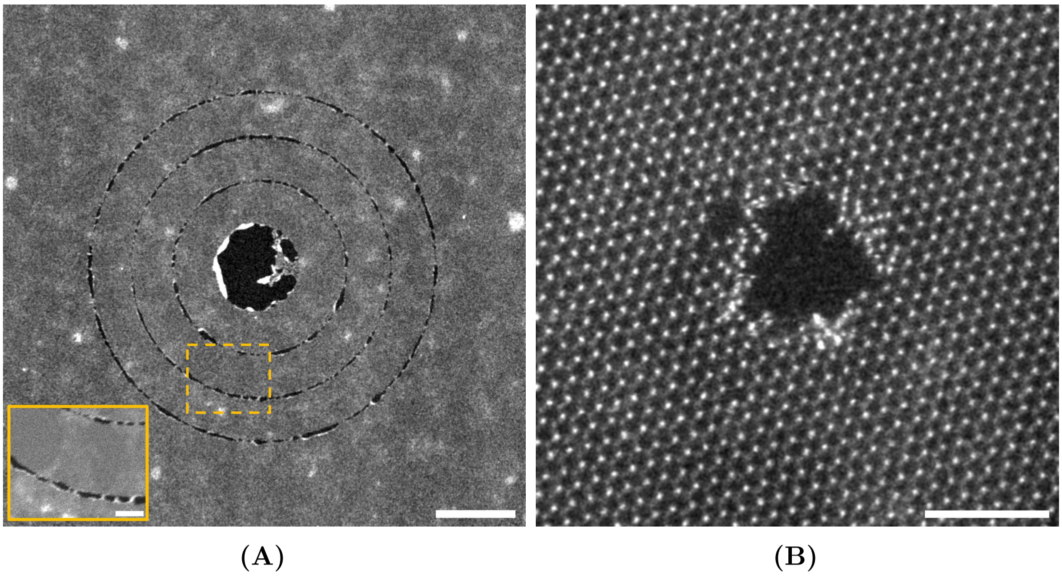
(A) (B)

Figure 4.6: ADF-STEM images of patterns introduced by sputtering with 200 keV electrons. (A) Automated beam positioning allows the creation of any desired shape, demonstrated by a structure consisting of a central hole and three concentric rings. (B) Due to the small achievable electron probe size, atomic-scale patterning is possible. Scale bars are (A) 50 nm, (inset) 10 nm and (B) 2 nm. (A) Reprinted with permission from Haas et al.[200]

4.1.3 Scanning Transmission Electron Microscope

EBIE and FIB are powerful tools for introducing patterns down to tens of nanometers. In order to create higher resolution structures, direct patterning was performed with the high-energy beam of the STEM. As described in the Methods section, a patterning software was written for automated beam positioning in the microscopes allowing any desired shape to be patterned.

For example, a central hole surrounded by concentric rings is introduced into a MoS_2 monolayer. The pattern is shown in Fig. 4.6 A. The central hole has a radius of 25 nm and the concentric rings measure 50, 75 and 100 nm in radius, respectively. The thickness of the rings is supposed to be 2 nm. However, the ring structures are not perfectly continuous, exhibiting remaining connections in some places. Remaining material is also present in the central hole.

The powerful capability of STEM for high-resolution patterning is demonstrated in Fig. 4.6 B by patterning a MoS_2 monolayer. In the ADF-STEM, the pristine hexagonal atomic lattice is clearly visible. In the center a hole with a radius of 1 nm is created by the electron beam. At the edge of the hole an accumulation of disordered atoms can be observed.

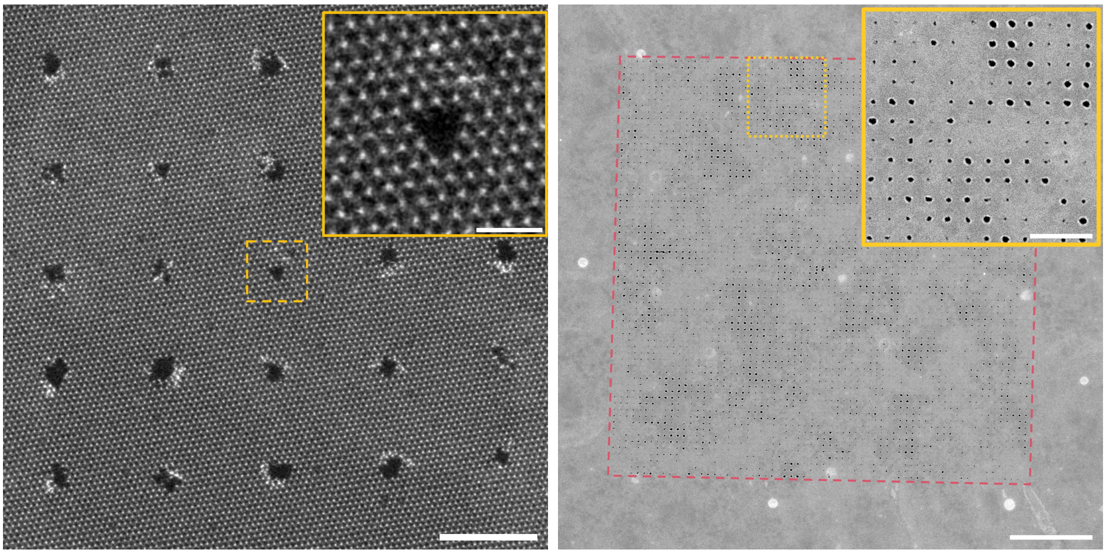

(A) (B)

Figure 4.7: (A) Array of holes patterned on the atomic scale with small variations in the exact hole size and shape. (B) 1 x 1 µm array with holes demonstrating the ability to create patterns with high resolution and accuracy even on large areas. Scale bars are (A) 5 nm, (A, inset) 1 nm, (B) 200 nm and (B, inset) 50 nm.

A regular array of holes with an intended size of 1 nm is patterned into WS_2. The result is shown in Fig. 4.7 A. The actual sizes of the holes vary between 0.5 nm (inset image) and 1 nm. At the edges of most holes, clustering of atoms is clearly visible. The pristine lattice shows some smaller defects, which can result from the electron irradiation during imaging.

High-resolution patterning can also be achieved for a large area. Fig. 4.7 B shows a regular array of 5 nm holes arranged over an area of 1 x 1 µm. The distance between the holes is 15 nm. Brighter and darker patches indicate different levels of contamination across the sample. The varying sizes of the introduced holes are evident, and notably, some holes are entirely missing. Most importantly, however, holes are formed over the entire 1 μm^2 area allowing high-resolution patterning even on large areas.

The order in which the electron beam is directed at each point of the shape is critical to the quality of the structures created. In the following, the order will be referred to as the patterning direction.

For creating a simple circle, several patterning directions are possible. The circle can be patterned line-by-line as shown in Fig. 4.8 A on the left. As a result, more material aggregates at one side of the created structure. However, when patterning spirally from the inside to the outside, the aggregation occurs symmetrically around

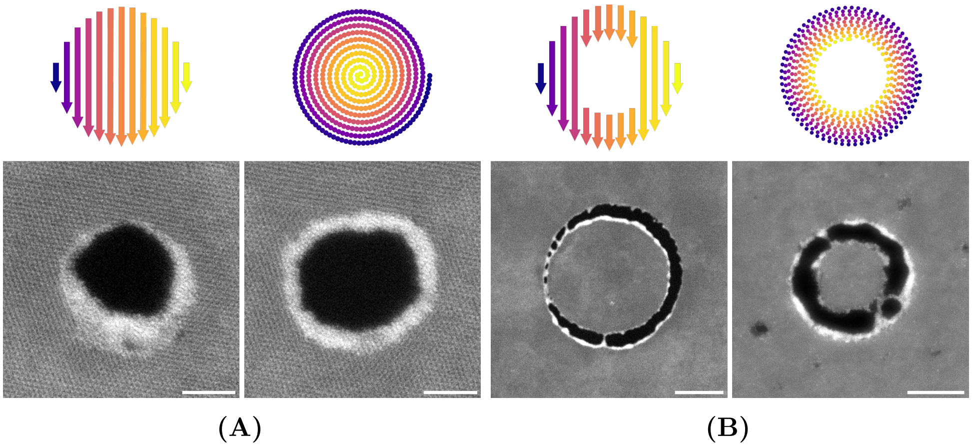

Figure 4.8: Influence of the patterning direction on the resulting structure. (A) When introducing a hole, a spiral-like patterning promotes an even agglomeration of redeposited atoms around the structure. (B) The patterning of a spiral-like ring can result in an almost freestanding disc. (B) Reprinted with permission from Haas et al.[200]

the hole (see Fig. 4.8 A left). The same behaviour has been observed for other geometries such as squares and rectangles. Generally, the material is deposited on the side where the patterning sequence ends.

The patterning direction is also crucial when introducing a ring into the thin membrane. When patterning line-by-line, the resulting disc sticks to the side where the patterning ends. For example, Fig. 4.8 B left shows a ring introduced into MoS_2 with the created disc attached to the left side.

In contrast, patterning the ring spirally results in a non-shifted disc, supported by residual material around the ring. Such a structure is given in Fig. 4.8 B right: A ring is patterned into WS_2 and the disc seems to be hold only by three tiny strings. Interestingly, complete falling out of these structures has never been observed. Breaking all the supports on one side will displace the disc and eventually attach it to the other side. Once a disc is attached, it can not be detached with the electron beam, regardless of an increased electron dose.

The quasi freestanding discs such as the one shown in Fig. 4.8 are investigated in more detail in the TEM, in particular to understand their stability. First of all, the crystal structure of the WS_2 is preserved next to the patterned site. Importantly, also in the central disc the crystallinity is maintained, as can be seen in Fig. 4.9. The TEM images reveal amorphous material in the patterned ring in addition to the remaining WS_2 strings previously observed. The amorphous material is probably due to the deposition of contamination during patterning. In some cases the strings of the residual material are not continuous from the inside to the outside. Therefore, the stability of the quasi freestanding discs probably derives from the amorphous material within the ring structure.

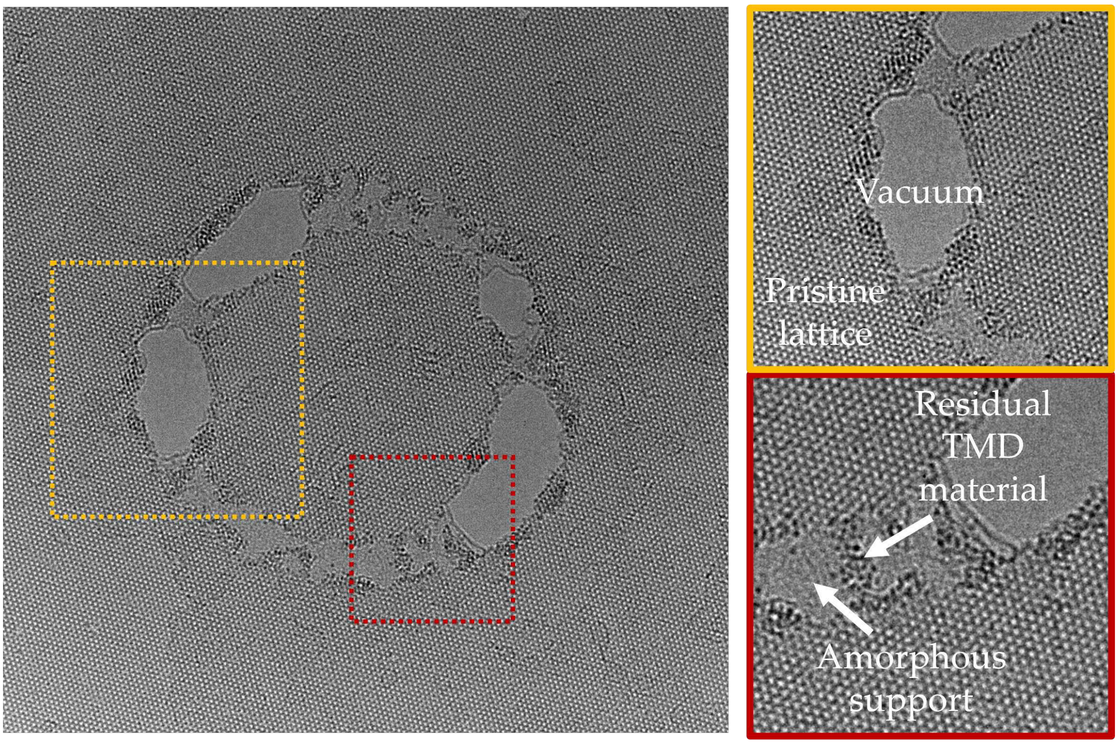

Figure 4.9: HRTEM images of the fabricated quasi freestanding WS_2 disc. The crystal lattice is perfectly preserved in the disc after patterning. Amorphous material and WS_2 residues can be seen, stabilizing the structure.

4.2 Photoluminescence of Patterned WS_2

The electronic and optical properties of 2D materials can be tailored by introducing modifications, for example by patterning on the nanometer level as shown in the literature, see Section 2.3. In this section, modifications due to an electron beam are investigated for a resulting change of the optical properties by measuring the PL. These experiments were carried out jointly with Nils Rieger within the scope of his Master's thesis, which I co-supervised. Freestanding WS_2 monolayers are used in order to avoid substrate related effects. Different patterns are introduced, such as hole arrays studied in the literature, but also the quasi freestanding disc presented above, which may show altered properties like an energy shift due to the size restriction.

In a first experiment, the PL of these two patterns are compared to pristine WS_2 and to an area which is exposed to the electron beam during imaging. The spectra are shown in Fig. 4.10. To enable a comparison, the data is normalized to the spectral region at 600 nm. The pristine WS_2 shows a sharp PL peak at 619 nm (≈ 2 eV), which is in good agreement with the room-temperature measurements from literature (see Fig. 2.6). This peak can be assigned to the A-exciton occurring in WS_2.[69] In addition, a small shoulder can be observed at around 670 nm. In the second spectrum of Fig. 4.10, the PL of a patterned WS_2 monolayer is shown. In this case, a quasi freestanding disc has been introduced (see Fig. 4.9). The intensity of the A-exciton is remarkably smaller compared to the pristine material, while the lower energy peak is more pronounced. For the patterned hole array (similar to Fig. 4.7), which requires a high electron dose, the A-exciton peak has completely disappeared and also no other feature can be seen in the spectrum. In the imaged area (fourth spectrum), no specific pattern was introduced but a

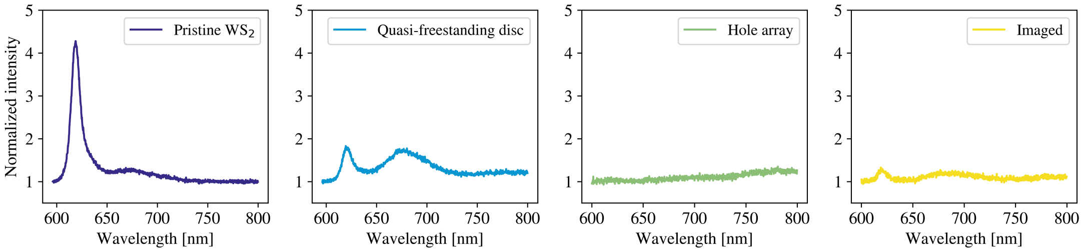

Figure 4.10: Photoluminescence of WS_2 exposed to a 200 keV electron beam during patterning or imaging. On the left side a reference spectrum of pristine, non-irradiated WS_2 is given, exhibiting a sharp peak of the A-exciton. In contrast, all the exposed WS_2 samples show a significant degradation of the exciton peak.

comparable electron dose was applied by illuminating the WS_2. Again, the peak of the A-exciton has almost disappeared and no other spectral feature is visible.

The first experiment reveals a significant degradation of the PL after electron beam irradiation. This effect is investigated in more detail with dose series for different electron energies. Freestanding WS_2 monolayers are irradiated in the TEM with 200 keV and 80 keV and in the SEM with 20 keV and 1 keV. Fig. 4.11 shows the dose series for the different electron energies. For these measurements, a different optical setup has been used, which only allows a reasonable measurement in the range between 600 nm and 690 nm. Nevertheless, the recorded spectra allow the examination of the electron beam induced degradation of the PL. To compensate for possible variances in the PL quality of the specimens that are used for the different energies, a reference spectrum has been recorded before the electron beam irradiation. For each electron energy, the intensity of the A-exciton

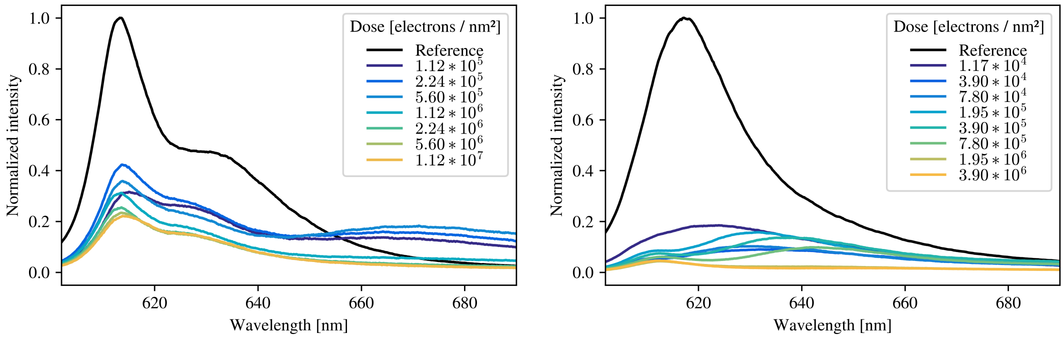

(A) 200 keV

(B) 80 keV

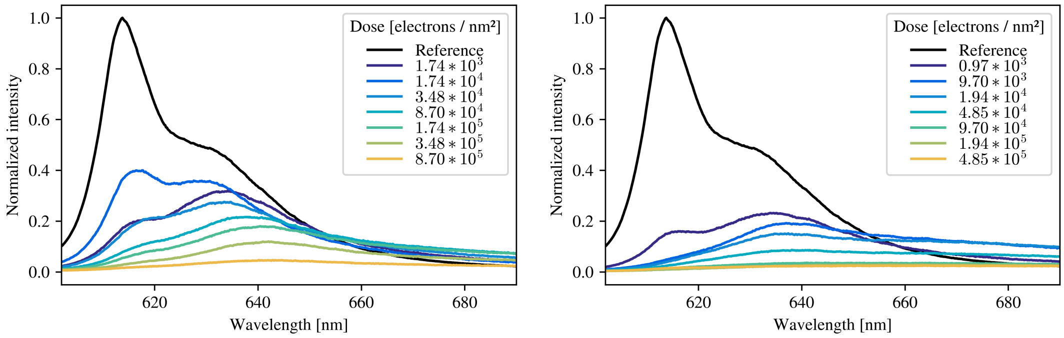

(C) 20 keV

(D) 1 keV

Figure 4.11: Dose series for different electron energies. For the 200 keV and 80 keV series, WS_2 is exposed to the electron beam in the TEM, for the 20 keV and 1 keV series in the SEM. As a reference for normalization, a spectrum is taken before electron irradiation (black curve). A substantial deterioration of the PL signal can be observed for all the investigated energies.

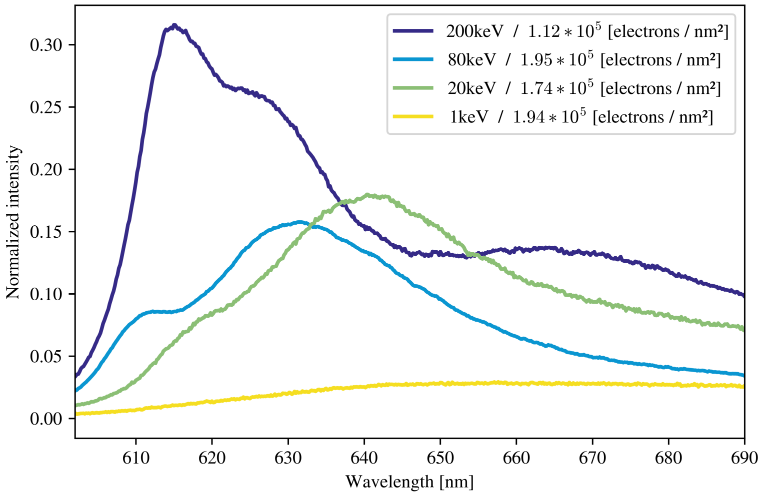

Figure 4.12: Comparison of different electron energies for similar applied doses. A stronger deterioration can be observed for a lower electron energy.

peak of this reference is used for normalizing, allowing the energies to be compared. The reference spectra are shown in black. Massive changes of the PL can be observed for all electron energies, especially the disappearing A-exciton peak at around 619 nm is striking. With increasing dose, the broad peak at lower energies dominates the PL spectrum. However, for the highest doses applied, there is almost no PL signal in the entire recorded spectral range.

In order to compare the different electron energies, comparable doses of the different series are considered as shown in Fig. 4.12. The A-exciton peak is only dominant in the 200 keV curve. For 80 keV, the exciton occurs as a small shoulder beside the broad lower energy peak. A similar behaviour, but even more pronounced, can also be seen for 20 keV. The spectrum of WS$_2$ exposed to the 1 keV electron beam exhibits an almost flat PL signal with no clear features. The measurements suggest that the PL signal increasingly deteriorates with decreasing electron energy.

4.3 Aligned Stacking of Nanopatterned 2D Materials

This chapter describes the development of a novel method for the fabrication of van der Waals heterostructures. In the Section 2.2, common techniques for the mechanical assembly have already been introduced. While these techniques are widely used, they have two major drawbacks with regard to miniaturization of the created structures and devices: The use of a substrate prevents the individual 2D layers to be patterned with high resolution prior to the assembly. In addition, the alignment during the assembly is observed by an optical microscope, thus the precision is limited to about 1 µm.

In this work, a method that overcomes these limitations is developed, allowing the aligned stacking of nanopatterned 2D materials for the fabrication of high-resolution structures. First, a general overview of the method is presented. Then, the individual process steps and components are described in more detail. Finally, assembled structures are demonstrated at the end of this chapter.

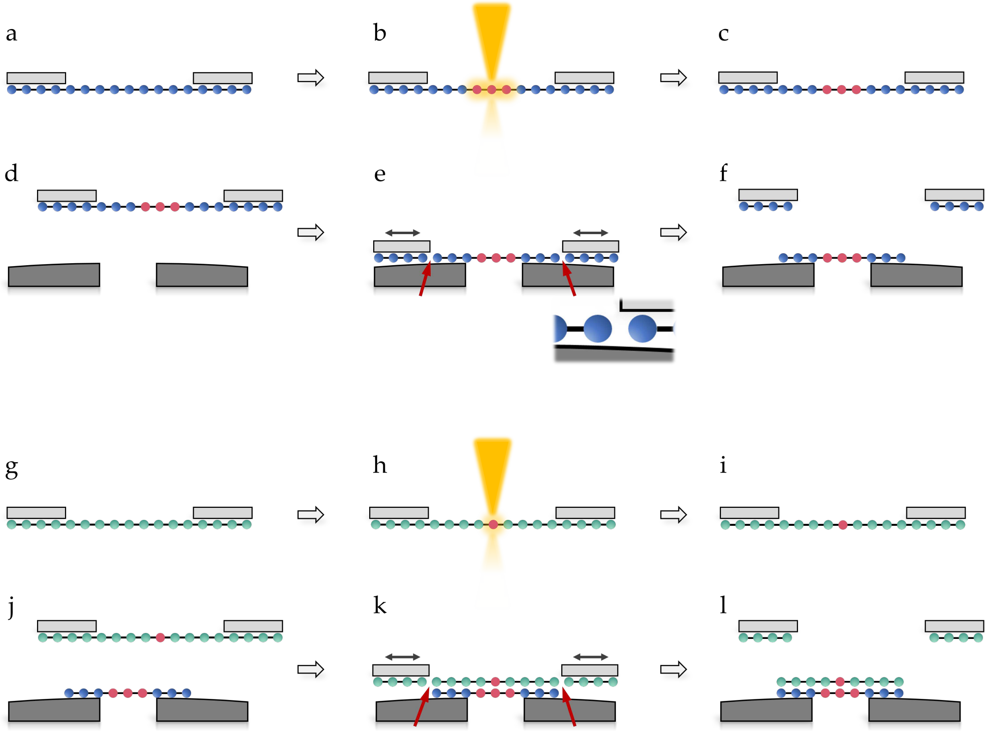

Figure 4.13: Schematic illustration of the invented stacking technique for the aligned assembly of nanopatterned 2D materials inside of an SEM. (A-F) Transferring the patterned layer from the perforated support film onto the substrate. (G-L) Repeating the process allows the assembly of multiple layers, creating a vdWH.

The method is schematically shown in Fig. 4.13. In order to enable high resolution patterning of the 2D material, freestanding membranes are used. The membranes are transferred onto a TEM grid, thus having them supported by the perforated carbon film of the grid (Fig. 4.13 A). After modifying the 2D material, e.g. by patterning with an high-energy electron beam (Fig. 4.13 B and C), the membrane is brought into contact with the target substrate (Fig. 4.13 D). The choice of the substrate will be explained and discussed in more detail below. Due to adhesion, the freestanding 2D material tears off from the support film and remains back on the target substrate (Fig. 4.13 E and F). By repeating these steps, additional 2D materials can be placed on top and thereby creating a van der Waals heterostructure.

Importantly, for precise control of the alignment on the substrate and the individual layers with each other, the stacking is performed inside of an SEM with the help of piezo manipulators, which allow extremely fine movements. Details on the setup will be presented below. Using an electron microscope allows observing the alignment with nanometer resolution.

The method can be divided into the following steps.

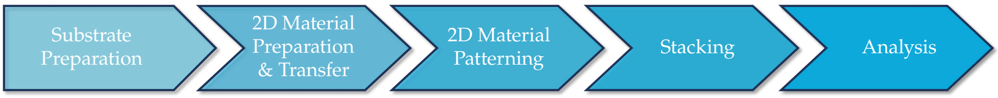

Each of these steps will be discussed in more detail in the following sections.

Substrate Preparation

As mentioned above, the developed stacking process is based on bringing the target substrate and the 2D materials into contact. Therefore, the choice of the substrate in terms of its geometry is very important. Bringing two straight planes into contact with each other at two distinct points is not possible. Thus, the target area of the substrate for the stacking must protrude and be the highest point of the substrate. In addition, the substrate has to fit into the SEM and the TEM for stacking and investigating the assembled vdWH.

To meet these requirements, a copper TEM lift-out grid is used. In particular, the central post as shown in Fig. 4.14 A serves as the position at which the heterostructure is to be assembled. However, additional modifications are necessary to make the post a suitable target substrate for the assembly and further TEM investigations. SEM and FIB images of the preparation are shown in Fig. 4.14 A-I. The central post is bent slightly upwards using tweezers, making the central post protrude. This can be seen in the SEM image in Fig. 4.14 D, showing a sideways view of the lift-out grid. By means of FIB, the shape of the central post is further modified: (C) At first, the width of the post is reduced to about 15 - 20 µm. (F) Afterwards, by milling from the side the post is thinned to approx. 5 µm. (H) In the final step, a rectangular hole serving as viewing window for TEM is introduced with a size of 2 x 2 µm. The surface of the post is slightly curved as can be seen in Fig. 4.14 e. This curvature facilitates contact between the 2D material and the substrate, in addition to bending the post upwards.

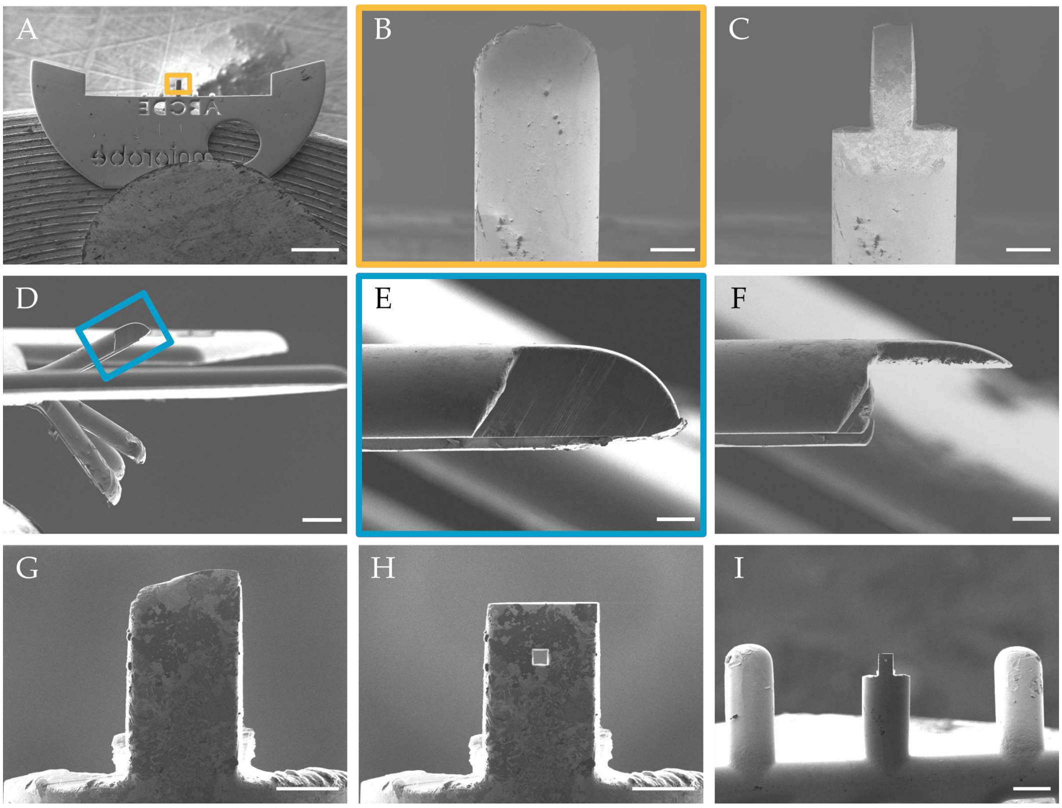

Figure 4.14: Preparation of the substrate by means of FIB. The central post of the lift-out grid is made thinner and narrower (B-F), and a window is inserted above it for examination in the TEM (H). Scale bars are (A) 500 µm, (B,C) 20 µm, (D,I) 50 µm and (E-H) 10 µm. Reprinted with permission from Haas et al.[200]

2D Material Preparation and Transfer

The 2D materials used for the assembly are obtained either by exfoliation or CVD-growth and subsequently transferred onto a TEM grid. Additional details regarding the methods can be found in Section 3.1.

For the stacking process, the 2D materials are prepared on a TEM grid with a QUANTIFOIL® holey carbon support film. The support film has a hole size of 10 µm, resulting in the 2D material suspended over a relatively large area. After transferring the 2D material, the TEM grid is carefully cut into quarters using a scalpel. This facilitates access to the region of interest on the grid.

2D Material Patterning

By patterning the 2D material prior to the stacking, in-plane structures can be introduced. As previously mentioned, the patterns can be created with high resolution, due to having the 2D material as a freestanding membrane. Depending on the required feature size, different patterning methods can be used as shown in Section 4.1.

For the assemblies presented in this work, EBIE is used to introduce structures into graphene as alignment marks for the stacking and measuring the precision of the invented method. In addition, direct patterning by STEM is used to introduce smaller features in graphene, but also to pattern non-carbon based materials such as MoS_2 and WS_2.

Special predetermined breaking points are introduced to facilitate detachment of the 2D material from the support film. As these structures are relatively large and damage to the crystal lattice in the close vicinity can be ignored, the breaking points are introduced by means of FIB. Fig. 4.15 shows a suspended graphene membrane across the hole of the support film with the patterned breaking points: Lines are arranged to form an almost closed circle at the outer part of the freestanding membrane, close to the support. The gap between the lines is approximately 500 nm wide.

Stacking in Scanning Electron Microscope

As mentioned above, stacking is performed under the observation in an SEM in order to assemble the patterned 2D materials with high precision. Therefore, a Zeiss CrossBeam XB 1540 has been used. Although this microscope is equipped with an additional ion beam column, only the electron beam is used. Thus, any scanning electron microscope with some additional equipment, which will be described in the following, allows the creation of vdWHs with the invented method. Fig. 4.16 shows

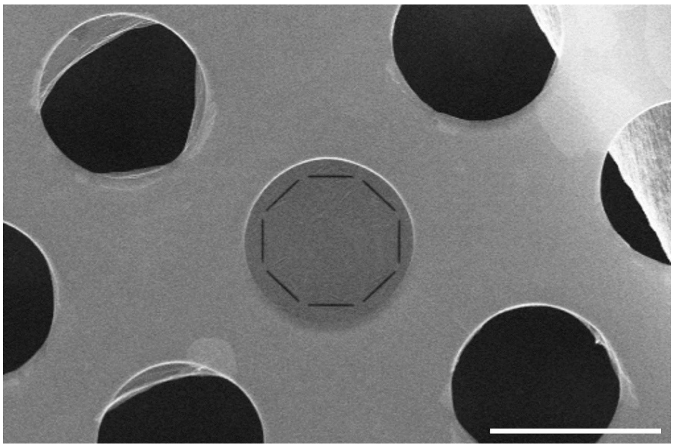

Figure 4.15: Predetermined breaking points introduced into the 2D material by FIB to facilitate tearing during stacking. Scale bar is 10 µm.

the schematic setup as well as a photograph of the electron microscope chamber.

The substrate is mounted on the microscope stage. This stage allows movements in the x-,y- and z-direction as well as rotating and tilting in one direction. The TEM grid carrying the patterned 2D material is clamped into a Kleindiek MM3A-EM piezo manipulator. The manipulator is mounted at the microscope chamber door. Importantly, tilts between the TEM grid and the substrate must be avoided. The optional use of an additional axis of rotation for the manipulator makes it possible to correct for misaligned tilts, but it was not used in this work. By mounting the manipulator on the chamber door rather than on the microscope stage, all available axes of both the manipulator and the stage can be used independently, giving more degrees of freedom for the alignment.

A photograph of the setup is shown in Fig. 4.16 B. It shows the opened microscope chamber with the piezo manipulator mounted on the door on the left. The TEM grid is held with a spring-based clamp as plug-in tool for the manipulator (see the inset in the photograph). On the right, the substrate is mounted on the microscope stage.

The stacking process is shown in Fig. 4.17 (A-F) and (G-L) as illustrations and SEM images, respectively. It is worth mentioning that a video recording the process is given in the supporting information of Haas et al.[200]. (A-C,G-I) First, the TEM grid is roughly positioned above the modified post of the lift-out grid. Importantly, vertical approaching is performed by using the z-axis of the microscope stage instead of using the manipulator to ensure a non-tilted arrangement. With the manipulator and the x-y axis of the stage, the patterned 2D material is moved above the viewing window the lift-out grid post.

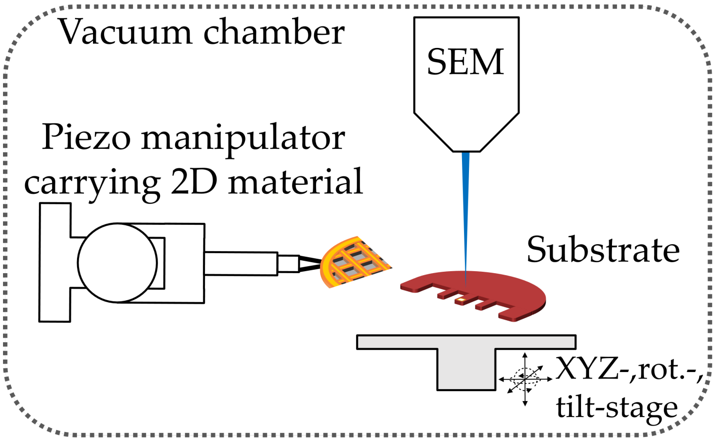

(A)

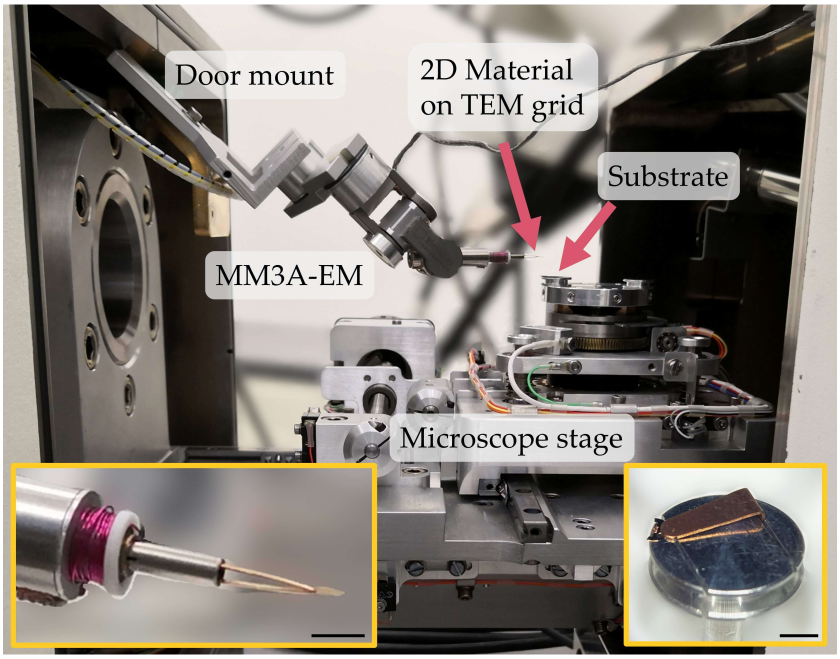

(B)

Figure 4.16: (A) Schematic drawing and (B) photograph of the setup used for the assembly of 2D materials in the SEM. The patterned 2D material is carried by the piezo manipulator (inset on the left) and located above the substrate (inset on the right). Scale bars are 3 mm. (A) Reprinted with permission from Haas et al.[200]

When choosing an acceleration voltage of 10 - 15 keV, the 2D material becomes semi-transparent, allowing both the 2D material on top and the substrate below to be observed. The vertical distance can be estimated by comparison of the focal lengths when imaging the 2D material and the substrate, respectively.

(D-E,J-K) After the rough alignment, a slow but continuous movement in the z-direction of the microscope stage is used to bring the 2D material and the substrate into contact. The 2D material can be aligned centrally over the viewing window in the substrate with the help of the piezo manipulator.

The contact is noticeable by a contrast change as can be seen in the above mentioned video and as illustration in (E). As soon as the 2D material and the substrate are in contact, the movement in the z-direction is stopped. Gentle and cautious x-y-movements with the manipulator allows breaking of the predetermined breaking points without any movement of the 2D material on the surface of the lift-out grid.

(F,K-L) Once the 2D material has been isolated from the support film, the substrate and the carrier can be moved away from each other resulting in the 2D material placed on the target substrate.

After the first layer, subsequent layers of 2D materials can be stacked on top in the same way to build a vdWH. Again, by choosing an appropriate acceleration voltage, the top layer becomes semi-transparent. This allows the observation of introduced patterns in both the already deposited 2D material and also the layer to be placed. Thus, the piezo manipulator can be used to precisely align the assembly.

The stacking of two layers with patterned features can be seen in the video.[202] Several example frames are displayed in Fig. 4.18 to show the observation and alignment of two layers. (A) shows a first graphene layer placed on the target substrate. A cross has been patterned before by means of EBIE, as illustrated in the inset image. (B) Another graphene layer with a 45° rotated cross is prepared and still on the support film. (C) The dual-mag mode of the electron microscope allows the observation of both the entire freestanding area (left) and a close-up to control the displacement of the two introduced features (right). As mentioned above, while moving them closer into contact, the layers can precisely be aligned with respect to each other. (D) and (E) shows images of the layers very close and in contact, respectively. A clear contrast change is visible.

By repeating the stacking process, additional layers can be placed in order to create an assembly of precisely aligned 2D materials.

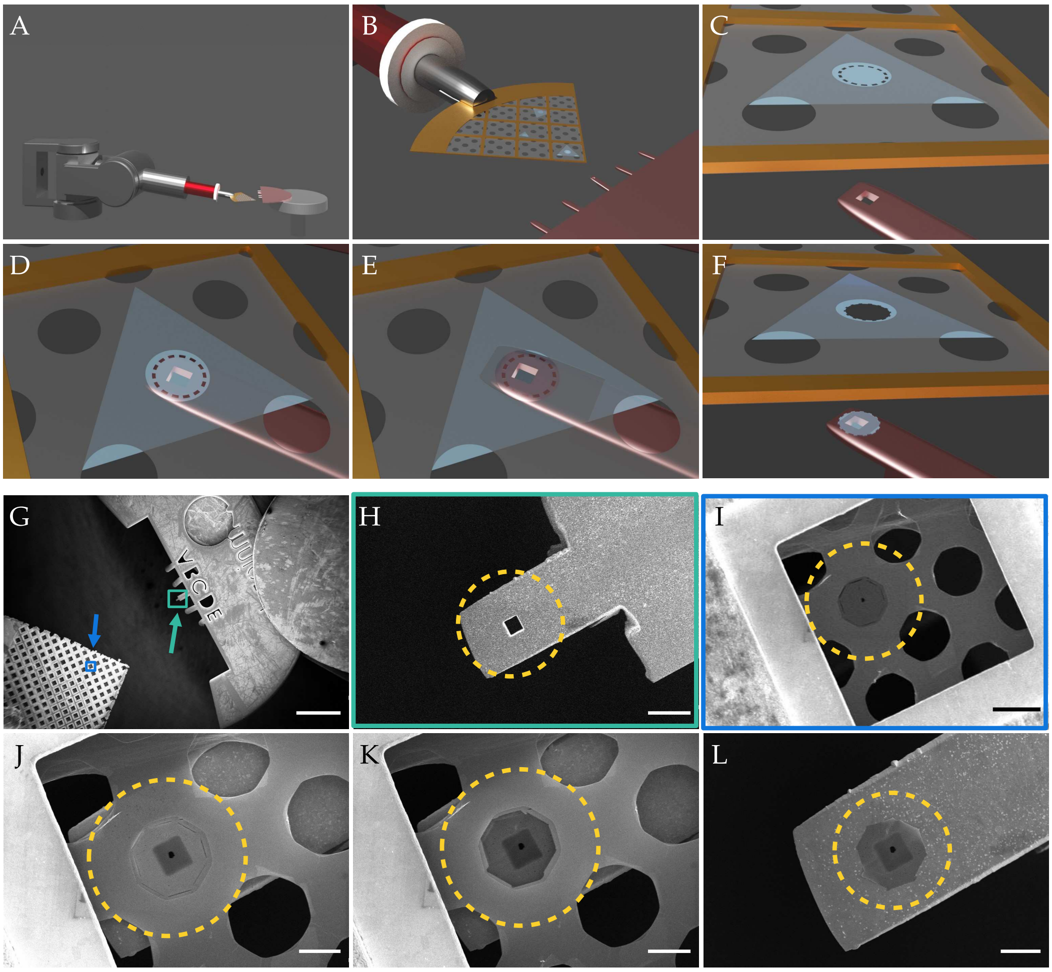

Figure 4.17: Stacking process as (A-F) illustrations and (G-L) SEM images demonstrated for a graphene layer with a small hole. (A-D, G-J) The quarter TEM grid carrying the 2D material is positioned above the substrate. (E,K) Bringing them into contact can be observed by a contrast change in the microscope image. (F,L) After breaking the predetermined breaking points, the 2D material remains on the substrate. Repeating the process allows the assembly of multiple 2D materials into a precisely aligned vdWH. Scale bars are (G) 500 µm, (H,I) 10 µm and (J-L) 5 µm. Reprinted with permission from Haas et al.[200]

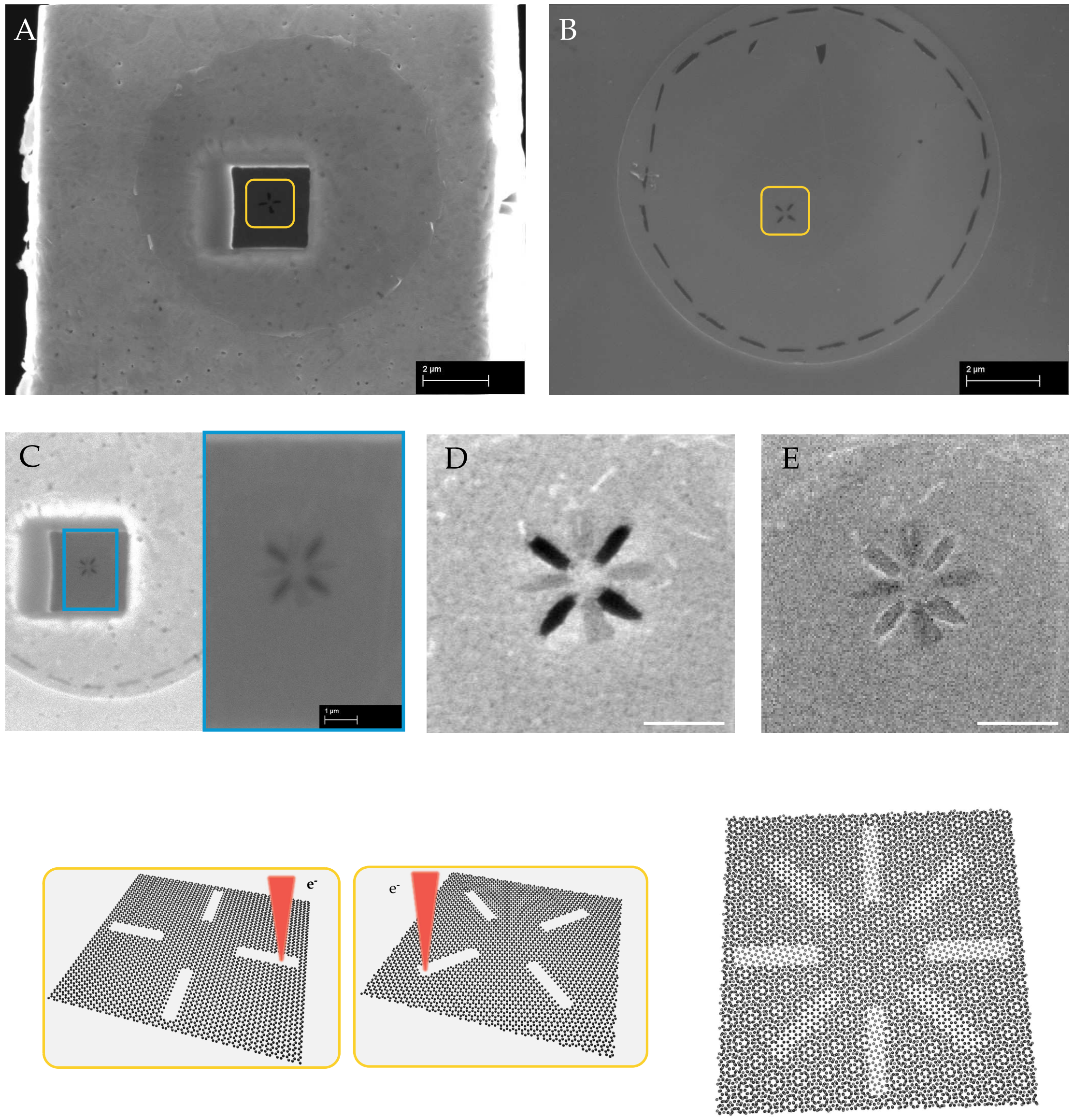

Figure 4.18: Extracted frames of a video recorded during stacking two patterned graphene layers. (A) The first layer is already placed on the substrate. (B) A second graphene layer is prepared on the support with the predetermined breaking points. As marker structures for the alignment, two 45° rotated crosses were introduced into the membranes by EBIE. (C) Substrate and support are brought closer to contact. Both crosses are visible in the SEM image and the dual-mag mode of the microscope can be used for a precise alignment. (D,E) Change in contrast at the moment when the two layers are brought into contact with each other. In the lower part, the assembly of the two layers into a crosshair structure is illustrated. Scale bars are (A,B) 2 µm, (C) 1 µm, and (D,E) 500 nm. Reprinted with permission from Haas et al.[200]

4.4 Stacking Results

Fig. 4.19 shows low magnification SEM images of two stacking processes. In both cases, graphene membranes are intended to be placed on the substrate. In (A), a small tilt between the support and the target substrate occurred and therefore, no contact could be made between the lower part of the graphene and the substrate. After tearing off the freestanding membrane from the support film, the graphene is rolled up rather than forming a flat film on the substrate as can be seen in the lower-left part of Fig. 4.19 A. In this case, it is not possible to stack further layers in a controlled manner.

On the other hand, if the substrate and support film are properly aligned in terms of tilts, the 2D material can be brought into contact over the entire freestanding area. As a result, the thin film adheres perfectly to the substrate. In Fig. 4.19 B, two layers of graphene are stacked on top of each other without any protruding edges. In the magnified image indicated by the yellow rectangle, the two layers can be distinguished by the small difference in contrast.

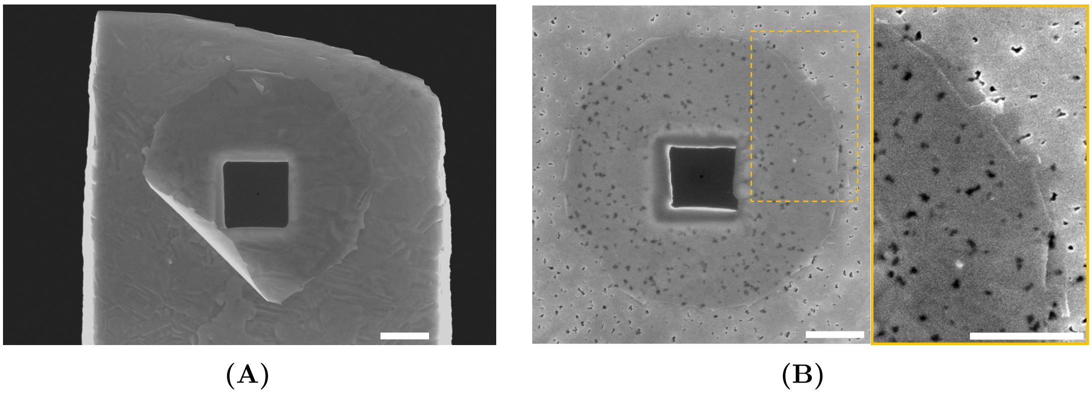
(A) **(B)**

Figure 4.19: SEM images after the stacking process. (A) Due to a misaligned tilt between substrate and 2D material, the lower left part of the membrane could not be brought into contact, resulting in a protruding film on the substrate. (B) When properly mounted, tilts between the substrate and the 2D material can be avoided. In this case, the two stacked graphene layers show perfect adhesion over the entire contact area. Scale bars are 2 µm.

The method can be used to stack any 2D material producible as a stable membrane suspended over the supporting film. For demonstration, several stacks from different materials have been fabricated and investigated by means of HRTEM.

As a first example, bilayer graphene is created. Fig. 4.20 shows the HRTEM image and the corresponding FT. Two sets of six points can be seen, indicating two twisted hexagonal lattices with same lattice constants. In the HRTEM image,

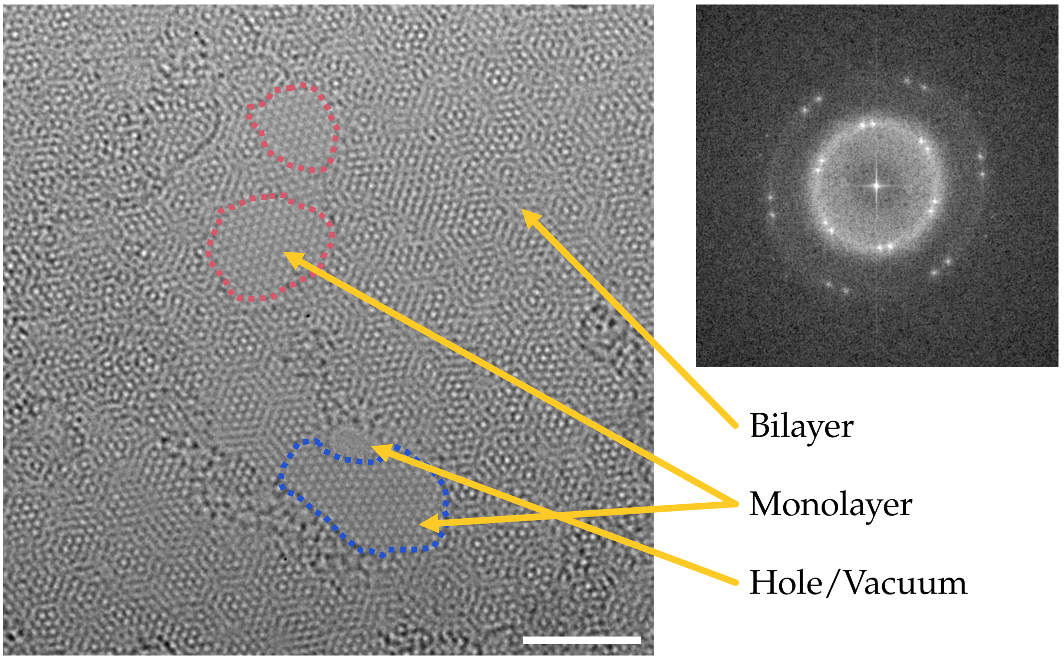

Figure 4.20: Bilayer graphene created by stacking two monolayers in the SEM. The HRTEM image reveals bilayer regions, monolayer regions and holes. The monolayer regions show different lattice orientations, indicating that damage occurred in both layers. Scale bar is 3 nm.

bilayer regions are also visible by the appearance of a moiré pattern. However, between the bilayer regions, monolayers and occasionally also holes occur. Interestingly, the lattice orientation of the two monolayers at the top (red dashed outline) are different from the orientation of the monolayer at the bottom (blue dashed outline). Thus, holes occur in both the top and bottom graphene layer. In addition, contamination is visible at several regions in the TEM image, e.g. in the left part.

Another example of stacking a different material is given in Fig. 4.21. Here, WSe_2 bilayers have been fabricated. Due to the high atomic number of WSe_2, hydrocarbon contamination has little influence on the image contrast and therefore, clear moiré patterns are visible in the HRTEM images. From the FT, the twist angle can easily be extracted from the angle between the two sets of points. As expected, the periodicity of the moiré pattern is inversely proportional to the twist angle: the smaller the twist angle, the larger the moiré period.

Neither the graphene nor the WSe_2 bilayers are true van der Waals heterostructures as they are made of the same material. However, similar to common mechanical assembly techniques, the presented method allows stacking of different materials without the constraints of lattice mismatch. Fig. 4.22 shows a graphene-MoS_2 heterostructure. The MoS_2 layer has been patterned prior to the assembly

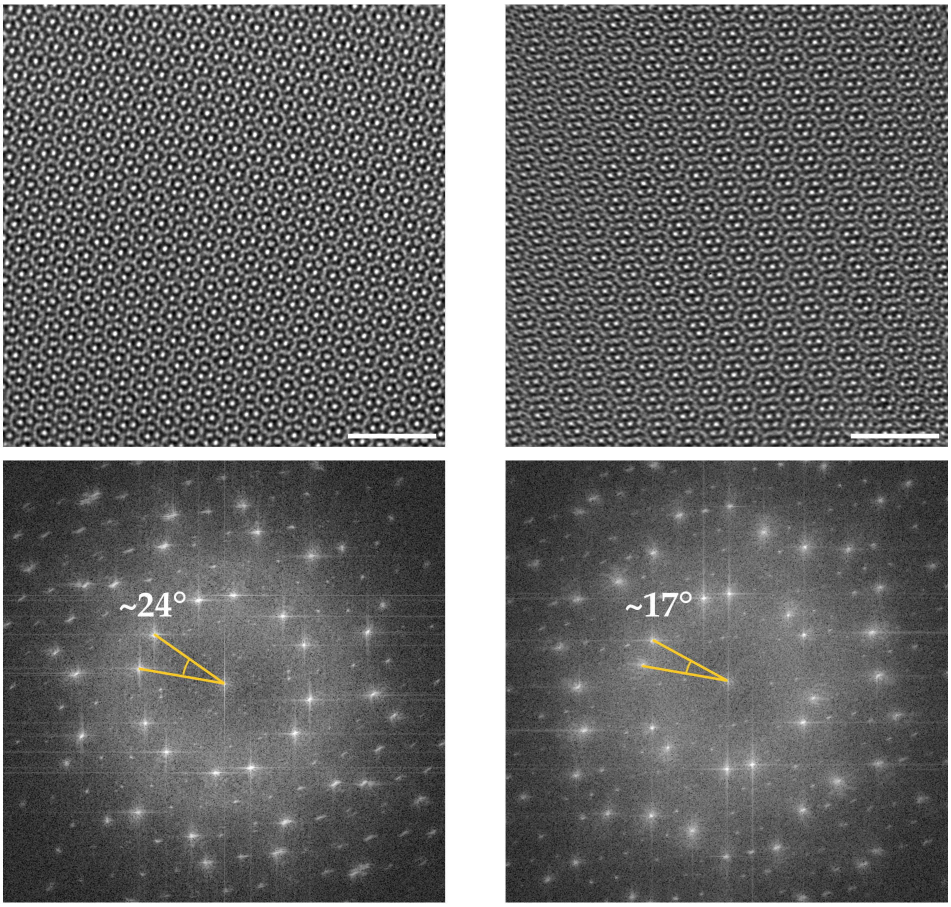

Figure 4.21: WSe_2 bilayers with different twist angles, resulting in different moiré periods. The exact twist angle can be measured in the FT. Scale bars are 3 nm.

with a similar structure as in Fig. 4.6 A. The HRTEM image in Fig. 4.22 shows a region of the heterostructure at the edge of the MoS_2 hole. On the left side, the graphene-MoS_2 stack is located. However, no moiré pattern is visible due to the difference in atomic numbers of the two materials. The FT exhibit two sets of points that have a small tilt angle, but more importantly, different frequencies and therefore originate from crystals with different lattice constants. The difference in the lattice frequencies in the FT is in good agreement with the expected difference of the lattice constants of graphene and MoS_2. As for the graphene bilayer, contamination is present all over the TEM image.

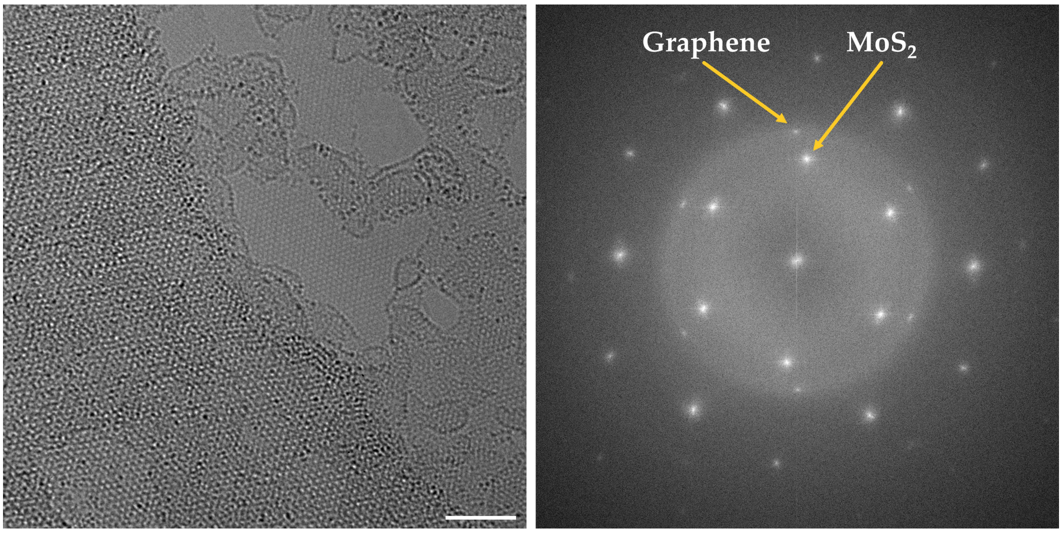

Figure 4.22: Graphene-MoS_2 heterostructure. The MoS_2 layer has been patterned prior to the assembly. The HRTEM image shows the edge of the introduced hole. The bilayer heterostructure and the graphene monolayer can be seen on the left and the right side of the image, respectively. From the FT, the two different lattice frequencies of graphene and MoS_2 can be identified. Scale bar is 3 nm.

Precisely Aligned Stacking

The main advantage of the presented method, however, is the ability to precisely align and stack nanopatterned 2D materials. Fig. 4.23 shows two stacking examples of graphene layers forming a crosshair-like structure. In Fig. 4.23 A-F, two graphene layers are patterned by EBIE with a hole and a cross, respectively. During the stacking, the two membranes are assembled by positioning the hole inside the cross. The resulting stack is observed in the TEM. Dark-field TEM is used to highlight the individual layers: By blocking all electrons except the ones of a certain diffraction spot, only the corresponding lattice orientation contributes to the image. Therefore, the cross and the hole are highlighted in Fig. 4.23 E and F, respectively.

Fig. 4.23 G-K shows the stack created as demonstrated in the published video and in Fig. 4.18. Again, dark-field TEM is used to distinguish the two layers after the assembly.

For both crosshairs, the individual layers are precisely aligned with respect to each other without major damage of the patterns. The relative twist between the crosses is maintained during the stacking. The displacement from the perfect alignment of the structures can be estimated to be about 20 nm.

A heterostructure consisting of MoS_2, patterned by STEM with the structure shown in Fig. 4.6 A is stacked on top of graphene, which is patterned with a hole done by EBIE. The two patterns are shown in Fig. 4.24 A and B. The central hole in MoS_2 and the hole in the graphene layer are precisely aligned during the stacking. By measuring the offset between the hole centers as shown in Fig. 4.24 C, the displacement between the layers is determined. For this structure, the two layers are stacked with a precision of about 10 nm.

In order to prove that the method allows a number of layers to be assembled, a ten layer stack of graphene is fabricated. In each of the layers, a hole with a different size is introduced by EBIE. Next, the layers are stacked in the order of increasing hole size. SEM images after each stacked layer are shown in Fig. 4.25 A. An illustration and TEM image of the resulting three-dimensional structure is given in Fig. 4.25 B and C. Small displacements of the hole centers can be recognized, with an average offset of the alignment for the ten layers of about 17 nm. The diffraction pattern (see Fig. 4.25 D) shows several diffraction peaks with the same lattice constants, indicating the ten different graphene layers.

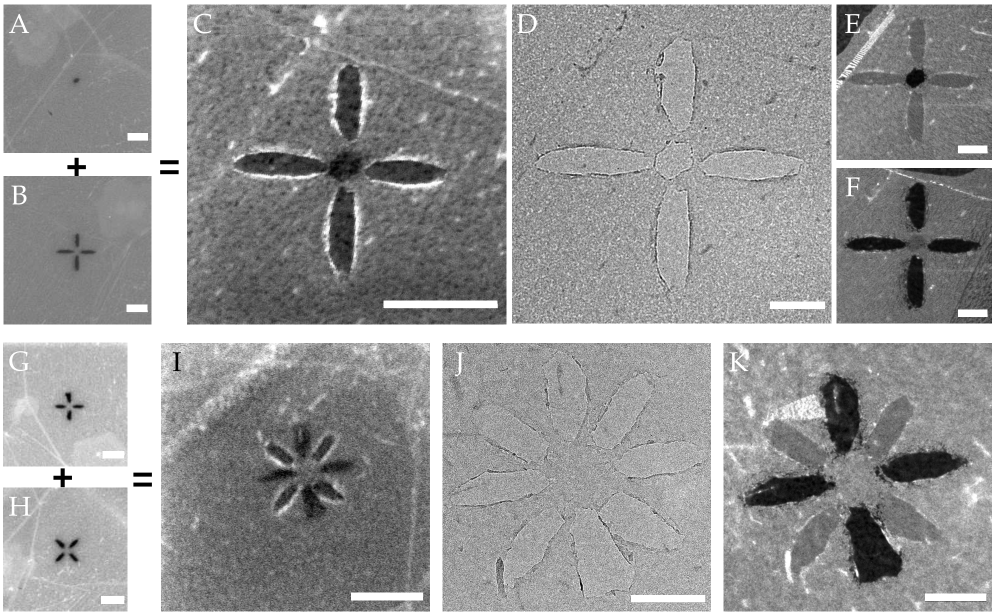

Figure 4.23: Precise stacking of two graphene layers forming crosshair-like structures. (A,B) Two freestanding graphene layers are patterned with a hole and a cross, respectively, and then precisely assembled. The resulting structure is shown as (C) SEM image, (D) TEM image and (E,F) dark-field TEM images to highlight the two twisted layers. (G-K) In another example structure, crosses are introduced into two graphene layers and subsequently stacked. Again, the assembly is investigated by (I) SEM, (J) TEM and (K) dark-field TEM. For the second structure (G-K), a video of the stacking process is published in Haas et al.[200]. Scale bars are (A–C, G–I) 500 nm, (D–F,J,K) 200 nm. Reprinted with permission from Haas et al.[200]

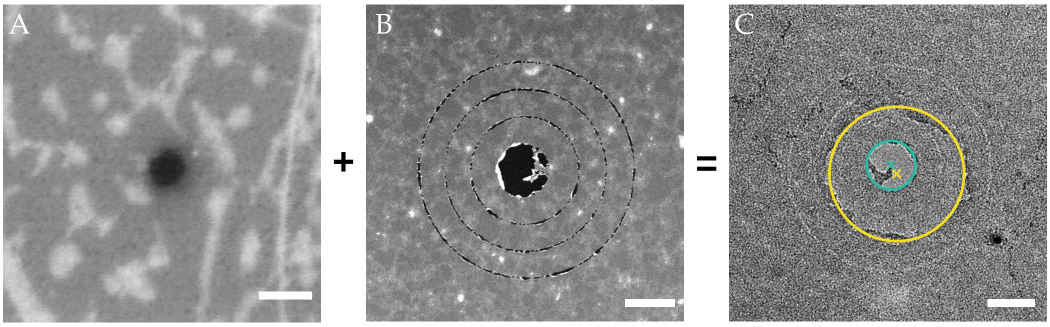

Figure 4.24: Heterostructure of (A) graphene and (B) MoS_2, both patterned with different structures. The holes in each layer are aligned during the stacking. Measuring the displacement between the holes demonstrates a stacking precision of about 10 nm. Scale bars are (A) 200 nm and (B,C) 50 nm. Reprinted with permission from Haas et al.[200]

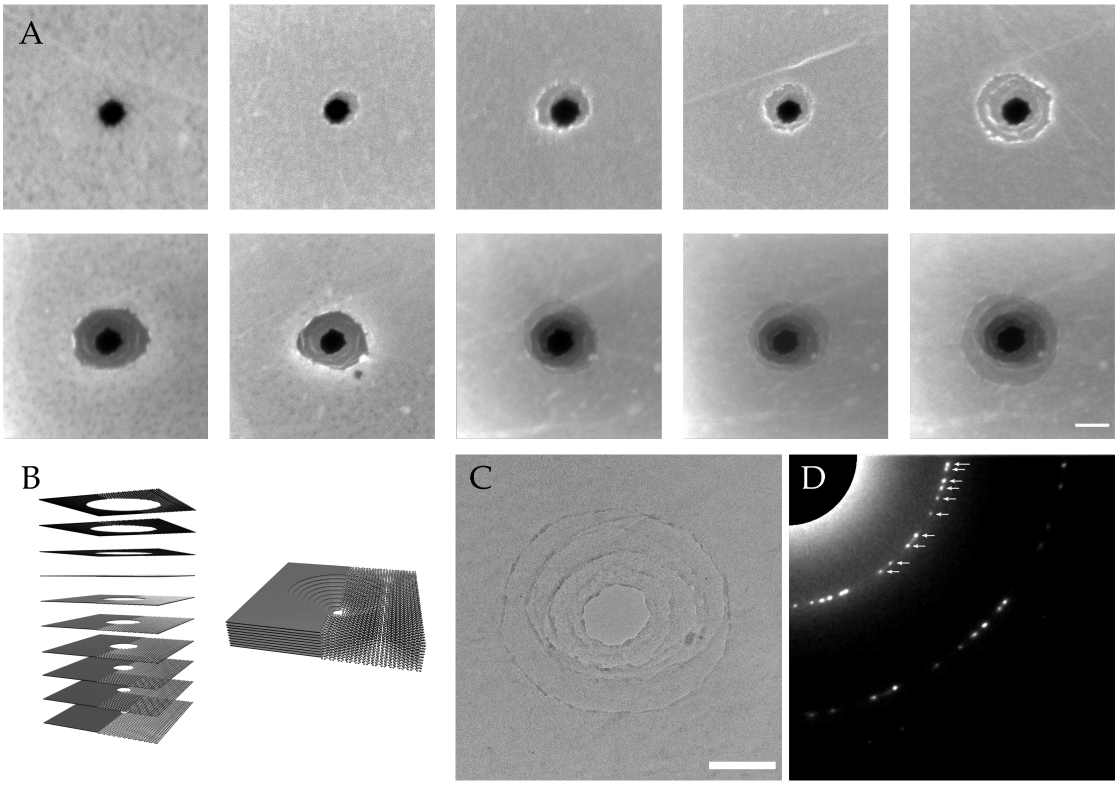

Figure 4.25: Ten layer assembly of graphene layers patterned with holes by EBIE. (A) SEM image after each assembly step. The layers are stacked in the order of increasing hole size, thus forming a funnel-like structure as illustrated in (B). (C,D) TEM image and diffraction pattern of the stack, showing ten differently orientated graphene layers. Scale bars are 200 nm. Reprinted with permission from Haas et al.[200]

Stacking of fragile structures

In the patterning chapter, the creation of a nanometer-sized, quasi freestanding TMD disc is considered. The area of the introduced ring is occupied mainly by amorphous material, presumably the deposition of contamination. These residues stabilize the structure, which is otherwise isolated from the surrounding material. With the invented stacking method, it is possible to stack these fragile structures onto another TMD membrane.

Fig. 4.26 shows a TEM image of such a stacked assembly. Due to contamination, the isolated disc is hardly visible in the image. To highlight the layers, Fourier filtering is applied to emphasize only a certain lattice orientation. The reciprocal lattice spots highlighted in yellow belong to the patterned layer, while the blue ones are associated with the pristine TMD membrane. As can be seen in Fig. 4.26 B, the fragile disc is transferred onto the second layer, with its lattice orientation and position preserved.

Variation of stacking process for improved precision

In the examples given above, the 2D material is first patterned and then stacked. Performing these steps in the reverse order allows the creation of a more precise assembly.

As an example, a structure that is similar to the ten layer stack shown above is fabricated from seven layers of graphene. For each assembly step, an SEM image is given in Fig. 4.27. Starting with a pristine graphene layer placed on the substrate (first image), a hole is subsequently introduced by means of STEM patterning. Afterwards, a second pristine graphene layer is stacked on top and then patterned with a smaller hole precisely aligned with respect to the first. These steps are repeated in this order with gradually smaller hole sizes to create the whole assembly.

TEM images of the final structure are shown in Fig. 4.28. In the FT, seven distinct reciprocal lattice spots are visible, indicating the presence of the seven layers of graphene with different orientations. The thickness gradient resulting from the decreasing hole sizes can be seen in the higher magnified image in Fig. 4.28 C.

The precision of the alternative stacking approach with the reverse order of stacking and patterning is estimated by measuring the displacements of the introduced holes. For the seven holes an average offset of 1.7 nm is determined, which can be considered as the precision of the stacking method.

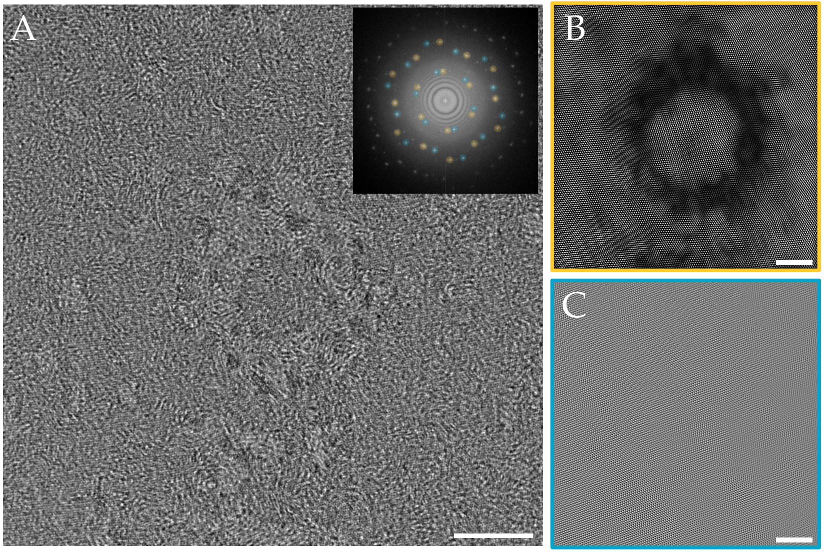

Figure 4.26: Stacking of a fragile, quasi freestanding WS_2 disc on pristine WS_2. (A) TEM image of the assembled structure. Contamination results in poor contrast, preventing the structure from being clearly visible. (B,C) Fourier filtering is used to highlight the two layers. Scale bars are (A) 10 nm and (B,C) 5 nm.

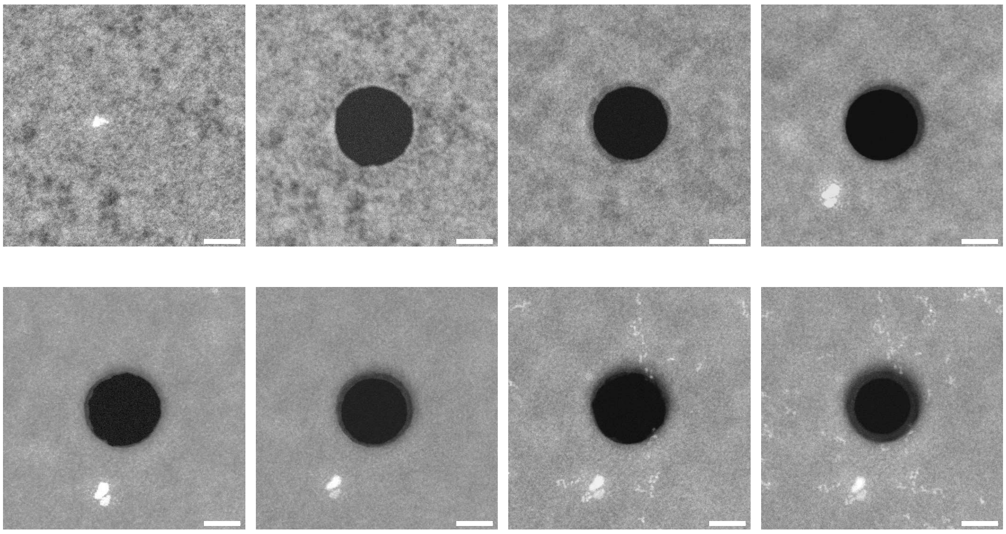

Figure 4.27: Variation of the stacking technique: Instead of assembling patterned layers, the pristine layer is placed first and subsequently the desired pattern is introduced, allowing a higher precision. This method is used to assemble seven graphene layers with varying hole sizes. The first two SEM images show the first pristine layer and the hole patterned into this layer. The following images show the introduced holes of the next layers. Scale bars are 30 nm.

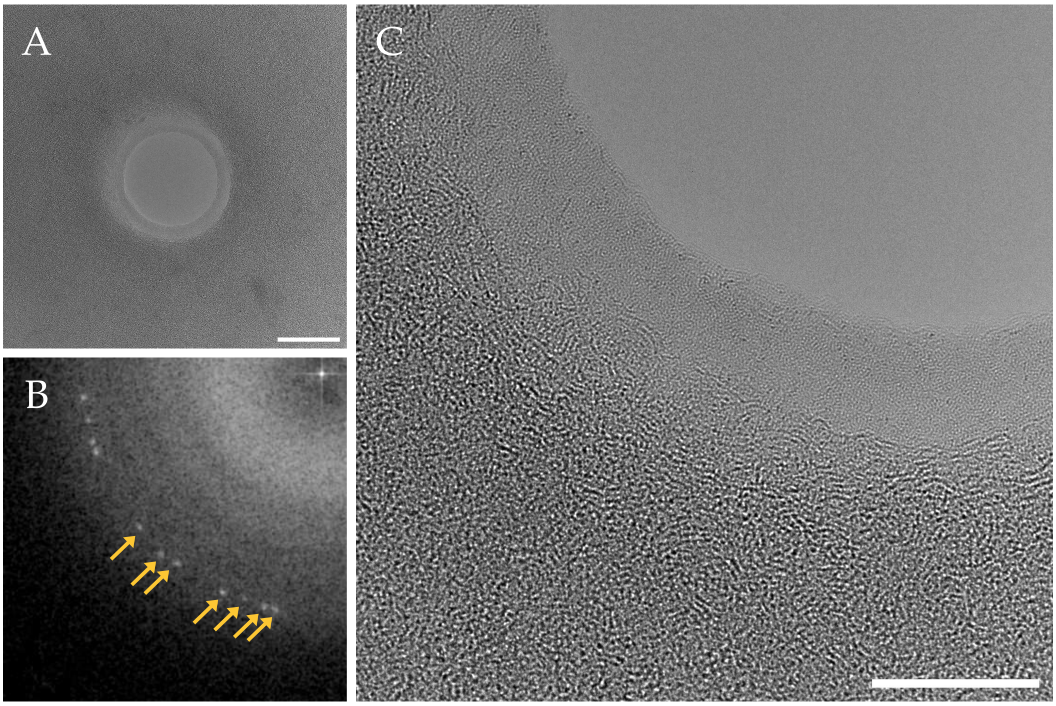

Figure 4.28: TEM images of the seven layer stack. (A) Overview image and (B) the corresponding FT of the image. From the FT, the seven different graphene layers are visible. (C) A higher magnified image indicates the resulting thickness profile of the stacked structure. Scale bars are 10 nm.

4.5 Phase Plates from Nanopatterned Graphite

The combination of patterning and stacking of 2D materials allows the creation of tiny assembled 3D structures with great flexibility in shape by adjusting the pattern in each layer as well as layer thicknesses. This enables direct fabrication of functional devices and structures on the nanometer scale. In this chapter, electron beam shaping elements are fabricated in this manner and tested for their ability to form a desired beam profile similar to thin-film phase plates in an in-line holography setup as described in the theoretical part of this work. However due to the small size of the structures that can be produced, the beam is shaped on the nanometer scale and the resulting small electron probes are formed from a parallel incoming electron wave without the need of additional electromagnetic lenses.

The beam-shaping properties of a phase plate are determined by its structure. Thus, it is crucial to have control not only over the pattern's geometry, but also over the thickness of the phase plate, which determines the amount of the applied phase shift. While most deposited materials exhibit significant roughness, exfoliated layered materials such as graphite are atomically flat and therefore offer great control over their thickness, making them well suited as material for nanometer scaled phase plates.

In this work, several phase plates with different designs are produced. The concept, however, is the same and schematically shown in Fig. 4.29. (I) At first, simulations are carried out to determine the required phase plate pattern and thickness for the desired electron beam. (II) Using optical microscopy and atomic force microscopy, a graphite flake of an appropriate size and, more importantly, the correct thickness is selected from the large number of flakes produced by mechanical exfoliation. The chosen flake is transferred onto a TEM grid to obtain a freestanding membrane. The calculated phase plate pattern is introduced by STEM according to the previously presented methods. For more complex designs of the phase plates, these steps can be repeated in order to create phase shifts with more than just two levels. (III) After fabrication, the phase plate is tested in the TEM for its beam-forming properties. In the following, these steps will be considered in more detail for three different types of phase plates.

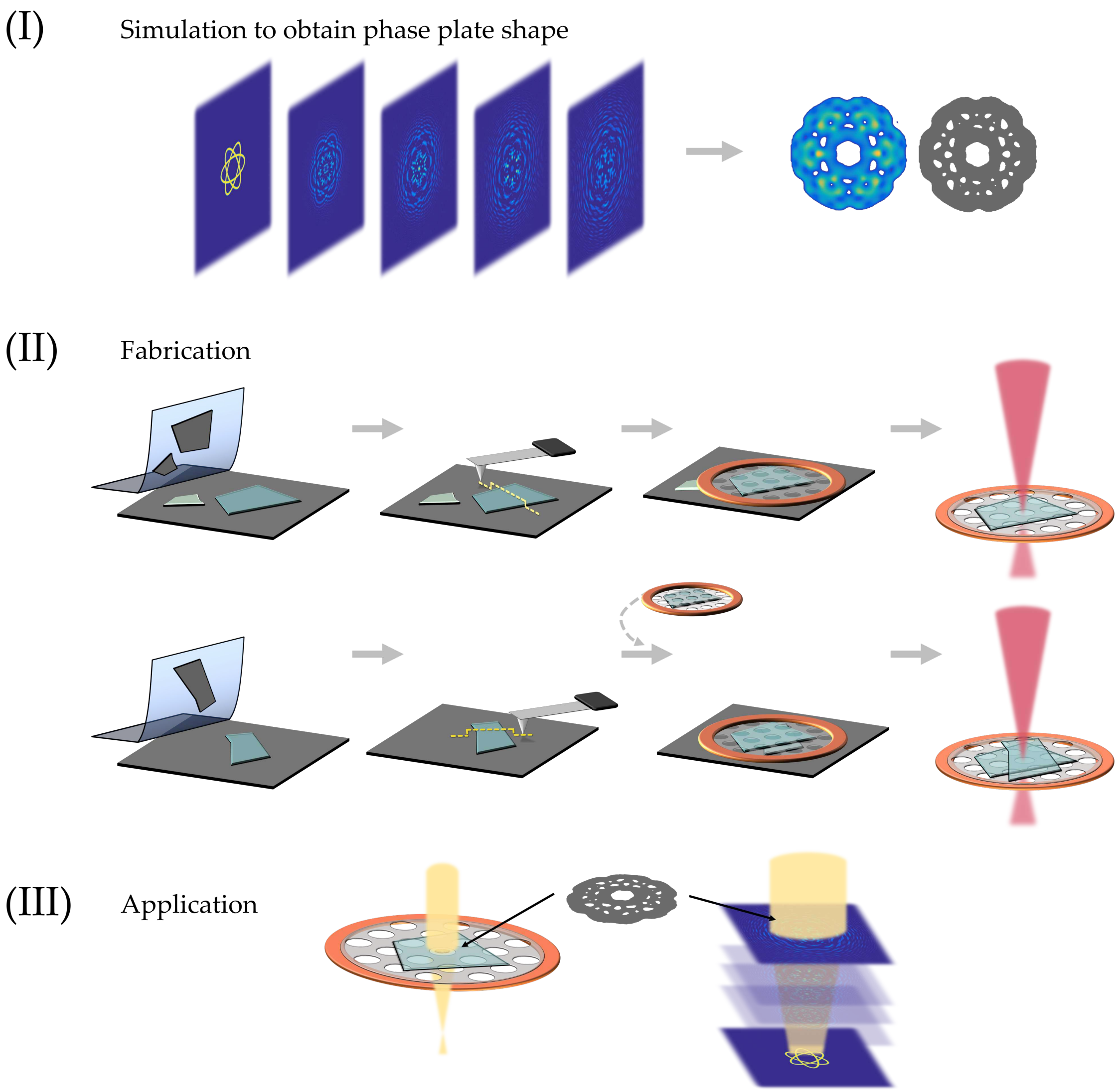

Figure 4.29: Concept of the demonstrated phase plates. (I) The phase plate shape including the required thickness is obtained by simulating wave propagation. (II) Exfoliated graphite flakes are transferred onto a TEM grid and subsequently patterned with a 200 keV electron beam. (III) The fabricated phase plate is tested for it's beam-shaping properties with a parallel 80 keV electron beam illumination.

4.5.1 Spiral Phase Plate

In the first case, a spiral phase plate is created, converting an incoming plane electron wave into a small electron vortex beam with an OAM.

The desired electron beam is used as input for the simulation of the required phase plate pattern, as shown in Fig. 4.30 A: The electron wave exhibits a doughnut-shaped intensity profile with a phase ranging from 0 to 2π. Subsequently, Fresnel propagation of the wave is performed in order to obtain the wave at the level where the phase plate will be located. Using a thin-film material, the phase plate generates only a phase shift, leaving the intensity almost unchanged. Therefore, the intensity of the wave at the phase plate position is ignored, whereas the phase corresponds to the necessary phase shift that must be applied to generate an electron wave forming the desired vortex. As can be seen from Fig. 4.30 B, the phase follows a spiral with gradients between 0 to 2π. In the next step, the phase is binarized, i.e. the regions between π and 2π are extracted up to the third turn of the spiral. These regions are indicated by the dashed line in the top image of Fig. 4.30 B and the inset. Fig. 4.30 C shows the extracted phase shift, which directly corresponds to the structure of the phase plate. To guarantee stability, the pattern is modified by adding support structures. The final pattern is given in Fig. 4.30 D.

In addition to the geometry of the pattern, the amount of the phase shift plays an important role. For the applied binarization, a phase shift of π is required for the phase plate to work as intended. The corresponding thickness of the thin-film material can be calculated from Eq. (2.9), resulting in 25 nm for graphite.

With the determined pattern and required thickness, graphite flakes are exfoliated onto a Si/SiO$_2$ wafer, which typically produces many flakes with different thicknesses. After initial screening with the OM, the flake with the correct thickness is selected by means of atomic force microscope (AFM) and afterwards transferred onto a TEM grid. The AFM measurement of the selected flake as well as an OM image after the transfer are shown in Fig. 4.31. The simulated pattern with the support structures is introduced into the freestanding graphite flake by direct-patterning in the STEM. Fig. 4.32 shows TEM images of the created phase plate. In the left image, the fragmented spiral is visible. However, the patterned sites are no trough-holes as can be seen in the higher magnified image in the center. While the crystallinity of the graphite is preserved for the non-patterned regions, the residual material inside the fragmented spiral is completely amorphous.

The beam shaping property of the fabricated phase plate is investigated in the TEM by illuminating with parallel electron irradiation and recording a focus series using the objective lens. By doing so, the propagation of the electron wave after passing the phase plate is imaged.

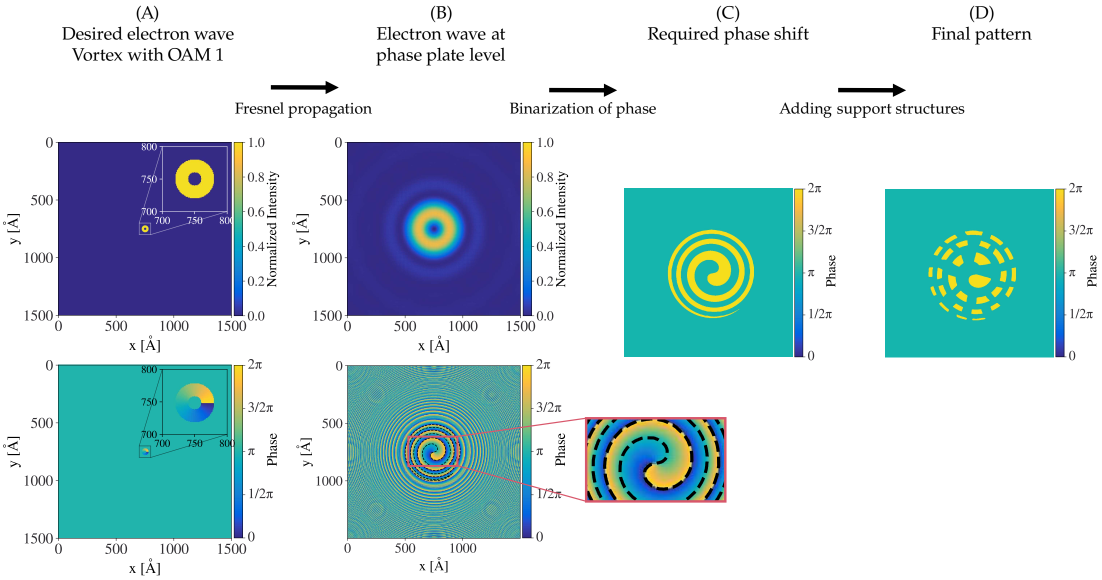

Figure 4.30: Computation of the required phase plate for generating an electron vortex beam. (A) The desired wave is taken as input for the simulation. (B) The wave is propagated to the phase plate level in order to obtain the necessary phase shift. (C) Binarizing and (D) adding support structures lead to the final pattern.

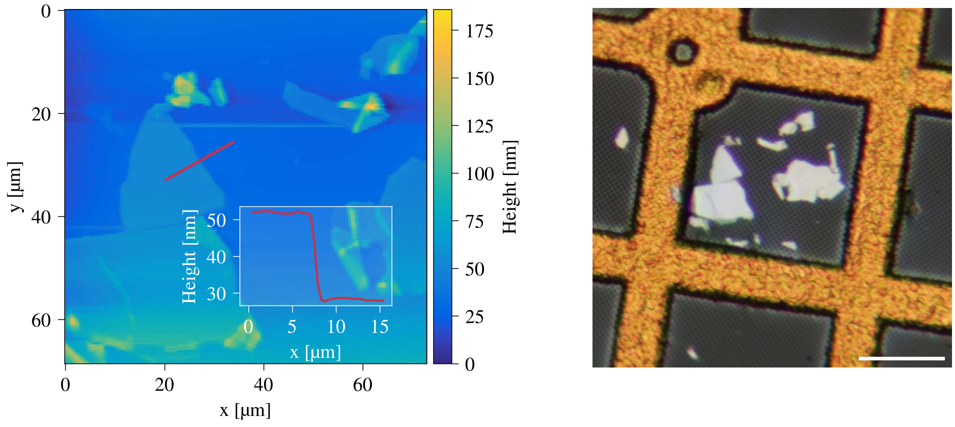

(A)

(B)

Figure 4.31: (A) AFM map of the selected flake on the Si/SiO$_2$ wafer. The inset shows an extracted line profile across the red line. (B) After verifying the thickness, the flake is transferred onto a TEM grid. Scale bar is 50 µm.

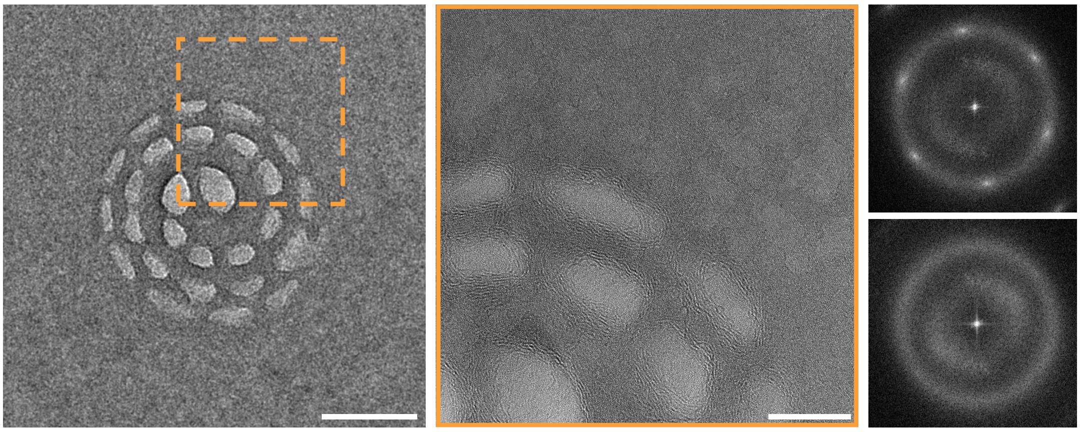
(A) (B) (C)

Figure 4.32: Spiral phase plate patterned in thickness selected graphite. (A) TEM image of the entire introduced structure and (B) HRTEM image of the top right region revealing residual material in the patterned holes. (C) The FFT of the non-patterned sites (top FFT) indicates that the crystallinity of the surrounding graphite has been preserved, while the residual material in the holes (bottom FFT) exhibits only an amorphous structure.

TEM images of the experiment for five selected focus values are given in Fig. 4.33 (A-E). To compare the change in intensity, contrast and brightness of the image series are set to the same value. (A) The in-focus image weakly shows the structure of the spiral phase plate. (B-E) As the electron wave propagates after passing the phase plate, an electron vortex is formed (Fig. 4.33 D) with an inner radius of about 1 nm and an outer radius of 2.5 nm. The vortex appears at a defocus value of 37 µm, representing the focal length of the spiral phase plate.

In addition, the propagation of the wave is simulated. Therefore, the actual patterned structure of the phase plate is extracted from Fig. 4.32 A. The simulated intensity and phase are shown in Fig. 4.33 (F-J) and (K-O), respectively. As can be seen, the experimental and the simulated intensity match very well. The experimental and, to a lesser extent, simulated intensity of the vortex exhibits an asymmetry.

The phase of the electron wave indicates the OAM of the vortex. However, the phase can not be determined from a simple TEM image. Due to the excellent agreement between experiment and simulation for the intensity, the experimental phase can be expected to match the simulated phase. For the generated vortex, the phase in the simulation runs from 0 to π, corresponding to an OAM of one.

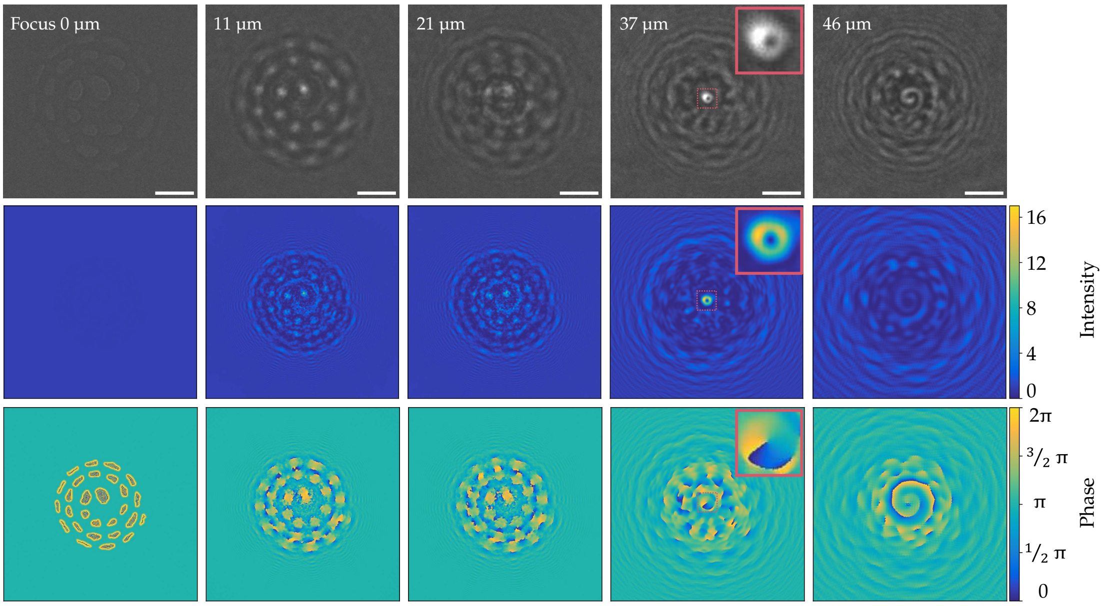

Figure 4.33: Beam-shaping behaviour of the fabricated spiral phase plate, investigated by a through-focus series. For five selected focus values, the experimental and simulated intensity is given in the top and middle row, respectively. The bottom row shows the simulated phase of the electron wave. Experimental and simulated intensities are in good agreement. An electron vortex appears for a focus value of 37 µm. From the simulated phase, an OAM of one can be expected for the vortex beam. Scale bars are 30 nm.

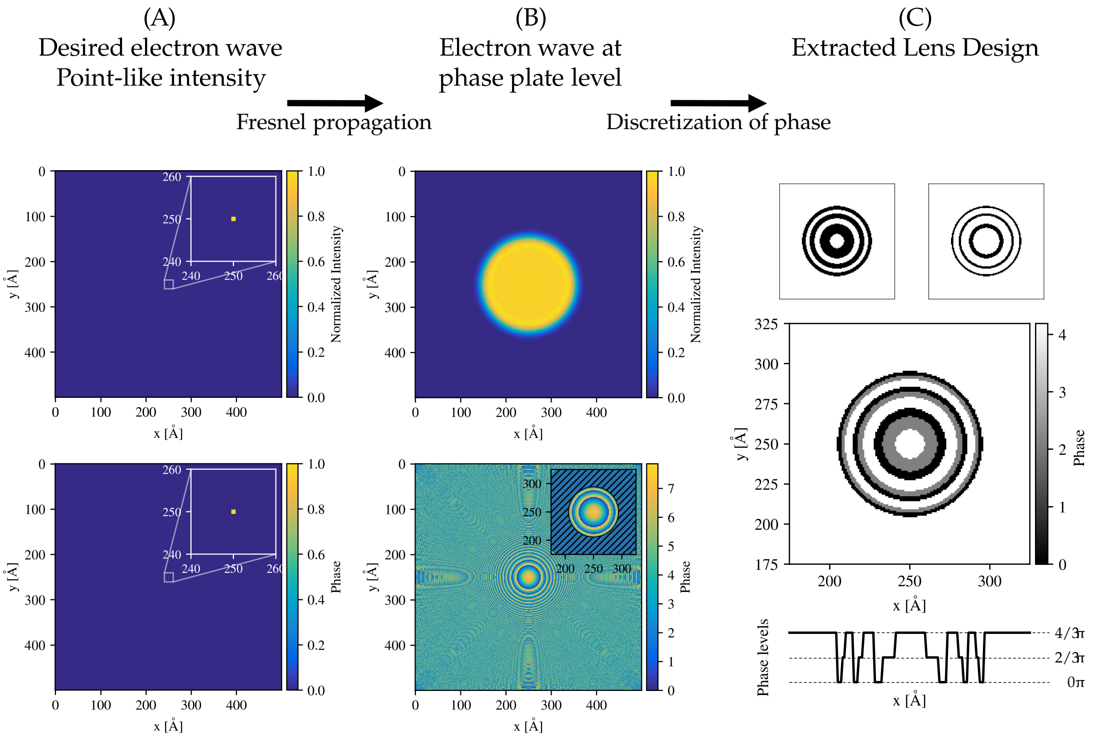

Figure 4.34: Derivation of the Fresnel lens design and required patterns obtained by simulating the wave propagation starting with the desired point-like electron wave (A). After propagating the wave (B), the required patterns are extracted from the wave's phase (C).

4.5.2 Fresnel Lens

As a second demonstration of the fabrication of nanometer sized beam-shaping elements from patterned graphite membranes, a Fresnel lens is presented. In principle, the geometry of a Fresnel lens to focus an incoming plane wave is straightforward. However, the required design is again derived from simulations using the same concept as above (see Fig. 4.34). In contrast to the vortex beam, the desired electron beam is now a single point of intensity. The shape of the phase plate is based on the propagated wave's phase, which in this case follows a wrapped parabolic profile. This profile is typical of a stepped Fresnel lens with phase jumps in multiples of 2π. The profile is discretized in three levels, as shown in Fig. 4.34 C. This design can be achieved by utilizing two layers and their appropriate patterning: Using two layers of the same thickness, the phase shifts become 0 for vacuum level, $^2/_3\,\pi$ for a single layer, and $^4/_3\,\pi$ for two layers. The subsequent phase shift level of $^6/_3\,\pi = 2\pi$ then corresponds again to the vacuum level. From Eq. (2.9), a required thickness of 16 nm can be calculated for the two graphite membranes, each applying a phase shift of $^2/_3\pi$ to 80 keV electrons.

The final design of the Fresnel lens is illustrated in Fig. 4.35. To ensure stability of the structure, the continuous rings of the design are interrupted by supporting bridges.

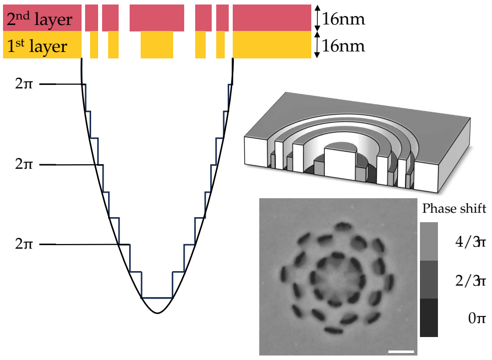

Figure 4.35: Design of the converging Fresnel lens. The ADF image shows the fabricated lens. Scale bar is 20 nm.

Graphite flakes are exfoliated and screened for the correct thickness by means of OM and AFM. The chosen flake is then transferred onto a TEM grid and patterned by using the high energy electron beam in the STEM with the first structure, which is indicated in orange in Fig. 4.35. In order to achieve the more complex phase shift profile of the Fresnel lens, however, a second layer with a different pattern is required. Therefore, another flake is selected by its thickness. The same TEM grid is placed on top of the already patterned region, aligned using a piezomanipulator under observation in the optical microscope and transferred with the procedure described in Section 3.1. Subsequently, the second structure (highlighted in red in Fig. 4.35) is introduced to finalize the lens design. Fig. 4.35 gives an ADF image of the fabricated Fresnel lens in the lower right, the three different levels can be seen from the gray shades. Here, the phase shift gray level bar displays the intended phase shifts, not a measurement. HRTEM is used to investigate the introduced pattern in more detail (see Fig. 4.36). Two regions are highlighted by colored rectangles. Fig. 4.36 (B) shows a higher-magnified image of the inner pattern. In the center, the crystal structure of the second graphite layer is visible. A brighter region can be seen above, representing the area in which both layers has been patterned. Instead of the expected through hole, weak contrast of amorphous materials is observed. Around the triangular pattern, redeposited material dominates the image. The edge of the Fresnel lens (Fig. 4.36 (C)) also reveals a significant amount of redeposited material around the patterned regions. On the left side of the image, the pristine structure of the two graphite layers is visible.

The lens's functionality is verified again by recording a through-focus series in the TEM in which the specimen is moved along the z-axis of the microscope while keeping the image plane of the objective lens fixed. Several example frames of the experiment are shown in Fig. 4.37 I-V. An orthogonal cut through the data cube of the recorded images can be seen in the middle of Fig. 4.37 A, with a line profile through the center. The positions of the example frames are indicated by the dashed colored lines. Small intensity enhancements are visible in both the underfocus

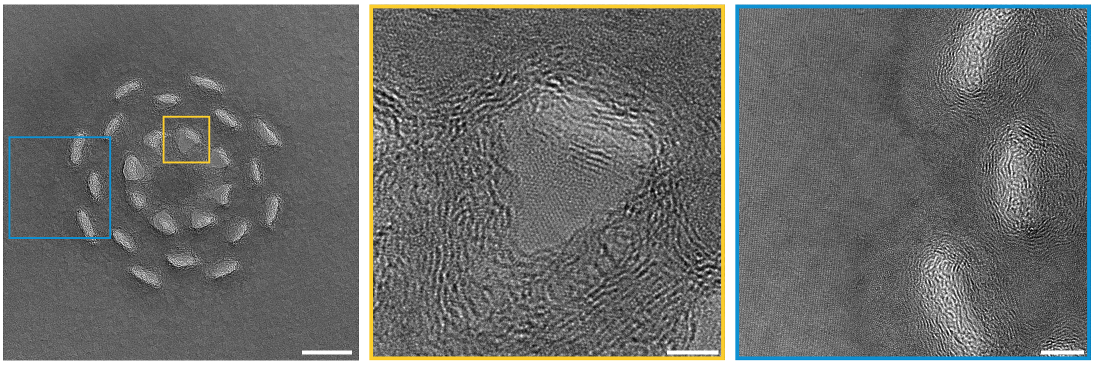

(A) **(B)** **(C)**

Figure 4.36: TEM image of the fabricated Fresnel lens with patterns in the two graphite layers. (A) Overview of the entire pattern. A close-up of the yellow and blue highlighted regions are given in (B) and (C), respectively. (B) The bright region represents an area in which both layers have been patterned. As can be seen, amorphous material is still present instead of the desired through hole. Below this area, a region in which only the first layer has been patterned occurs, thus showing the pristine lattice of the second graphite layer. (C) Redeposited material is visible around the patterned areas. Scale bars are (A) 50 nm, (B) 3 nm and (C) 5 nm.

(negative Z-position) as well as in the overfocus (positive Z-position) region. The lens exhibits a main focus at a focal length of about +80 µm, demonstrating the focusing behaviour of the created lens. The respective TEM image at the focal length is given in Fig. 4.37 V. Here, a clear intensity enhancement of a factor 15 relative to the background signal emerges with a full width at half maximum (FWHM) as small as 5.5 nm (see Fig. 4.37 B).

The central intensity as a function of the Z-position is simulated for a lens with the same dimensions, given as dotted line Fig. 4.37 B. As can be seen, the trend of the simulated and experimental intensity match very well, with small deviations in the underfocus region.

In addition to the converging Fresnel lens, the design is modified in order to obtain a diverging lens, as illustrated in Fig. 4.38 A. The manufacturing process is similar to that of the converging lens presented before. The diverging lens exhibits a focusing behavior, given in Fig. 4.38 B, with a dominant, but virtual focus in the underfocus region (i.e. at negative Z-values).

The long-term stability of the beam shaping properties of the diverging Fresnel lens is investigated by continuously exposing the lens with an 80 keV electron beam for 8 h. This simulates the application of such a graphite phase plate over an entire day. Every hour, a focus series of the underfocus region is recorded using the objective lens of the TEM. The result is shown in Fig. 4.39.

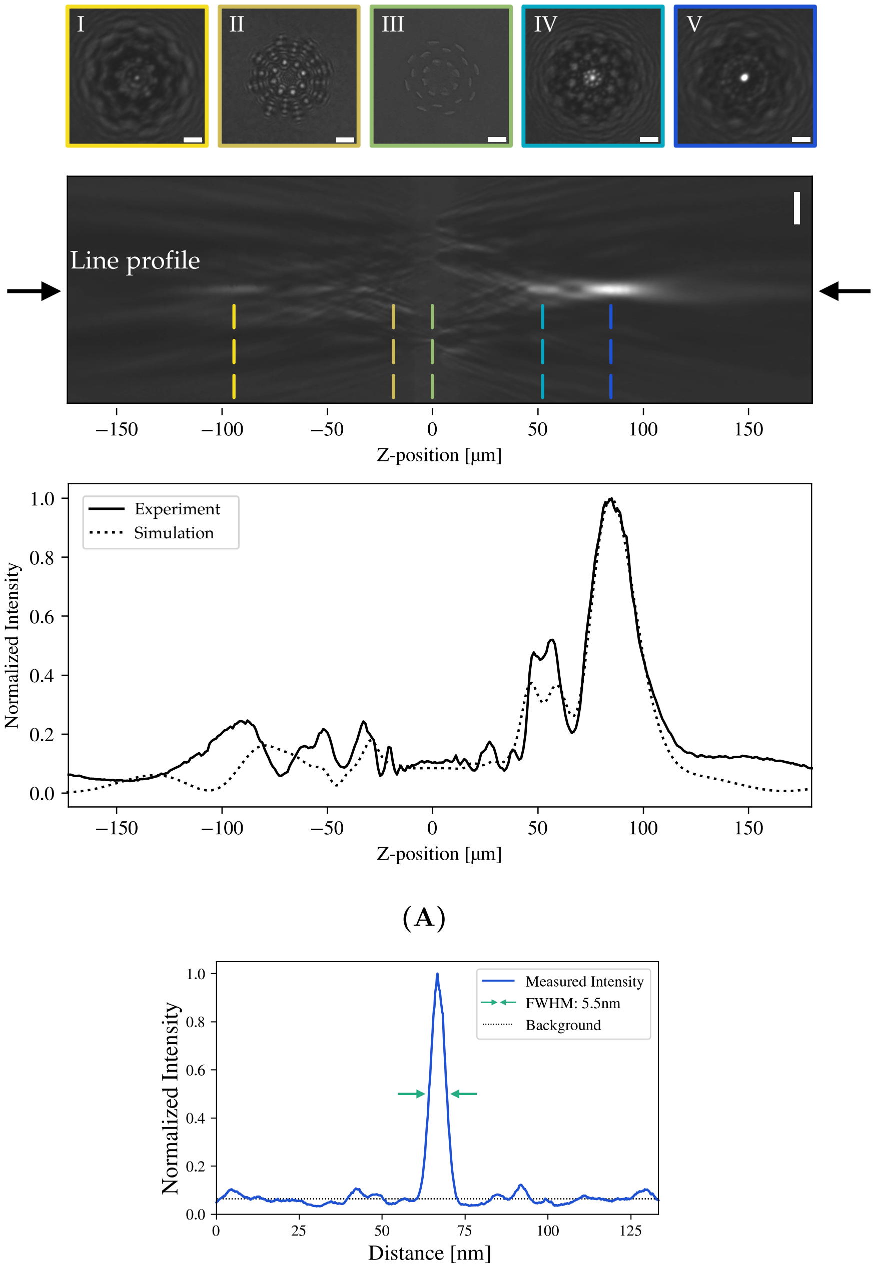

(A)

(B)

Figure 4.37: Beam forming properties of the converging Fresnel lens. (A) Through-focus series with exemplary images shown in the top row and an orthogonal cut through the data cube of the entire series given in the middle row. The position of the images are indicated by the colored lines. A line profile across the center of the lens (indicated by the arrows) demonstrating the focusing behaviour (lower part of (A)). (B) The line profile for the TEM image at the focal length (image V) exhibits a sharp intensity enhancement compared to the background signal. Scale bars are 20 nm.

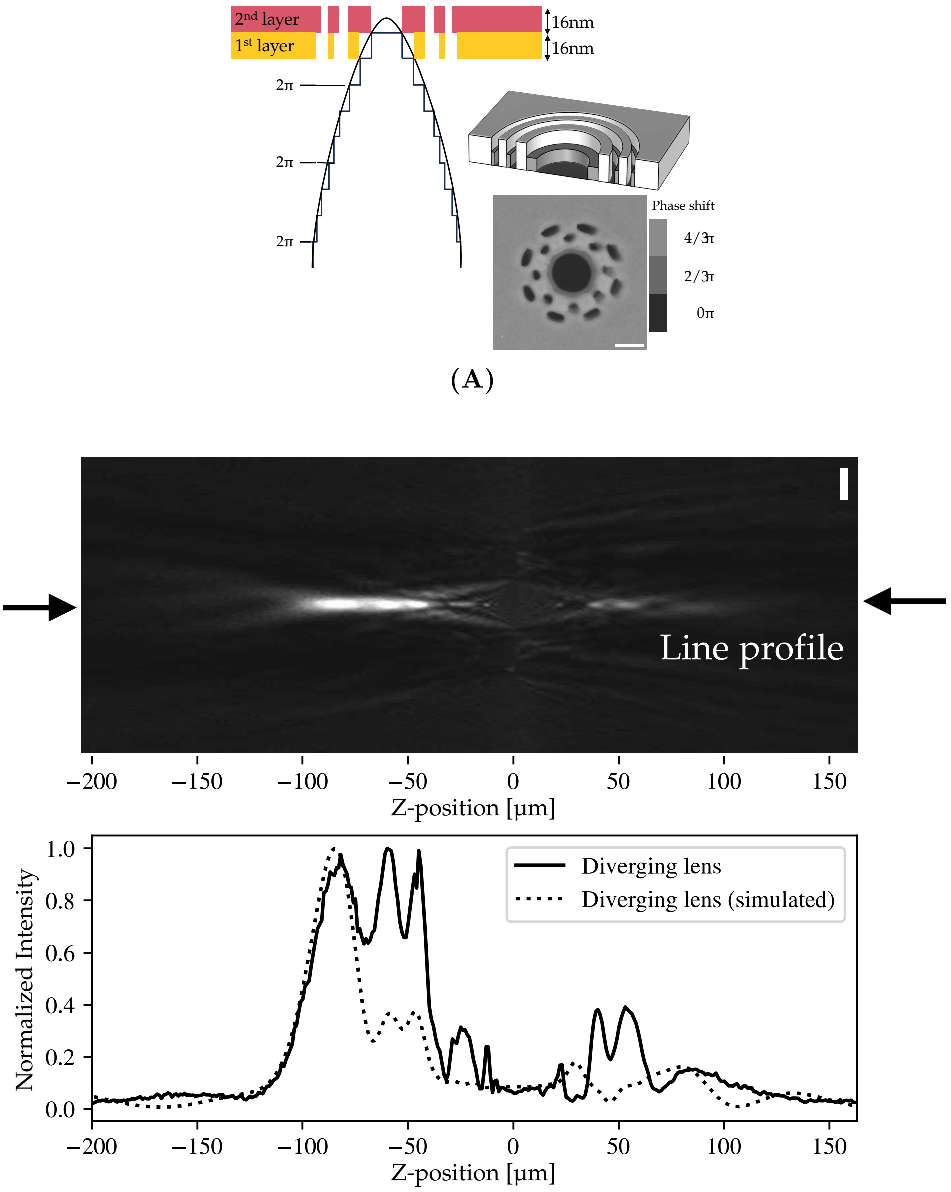

(A)

(B)

Figure 4.38: (A) Design and ADF image of the diverging Fresnel lens. Scale bar is 20 nm. (B) Beam forming properties of the diverging Fresnel lens. Orthogonal cut through the data cube for the recorded through-focus series. The central intensity is given as line profile in the lower part, showing the virtual focus at negative Z-values for the diverging lens.

TEM images are given for an irradiation duration of 0 h, 4 h and 8 h. A change of the lens structure can be observed over time: The central hole grows and the smaller structures become increasingly undefined, affecting the focusing behaviour. Orthogonal cuts through the data cubes for the three exemplary exposure times and line profiles of the focus for all the series are shown in Fig. 4.39 A and B, respectively. For better comparison, the initial trend (0 h) is plotted as dotted line. With increasing electron dose, the two maxima at lower focus values disappear, related to the increasing degradation of the introduced small patterns. The left focal maxima exhibits a continuously strong focal intensity, with a shift to longer focal lengths due to the increase of the central hole size.

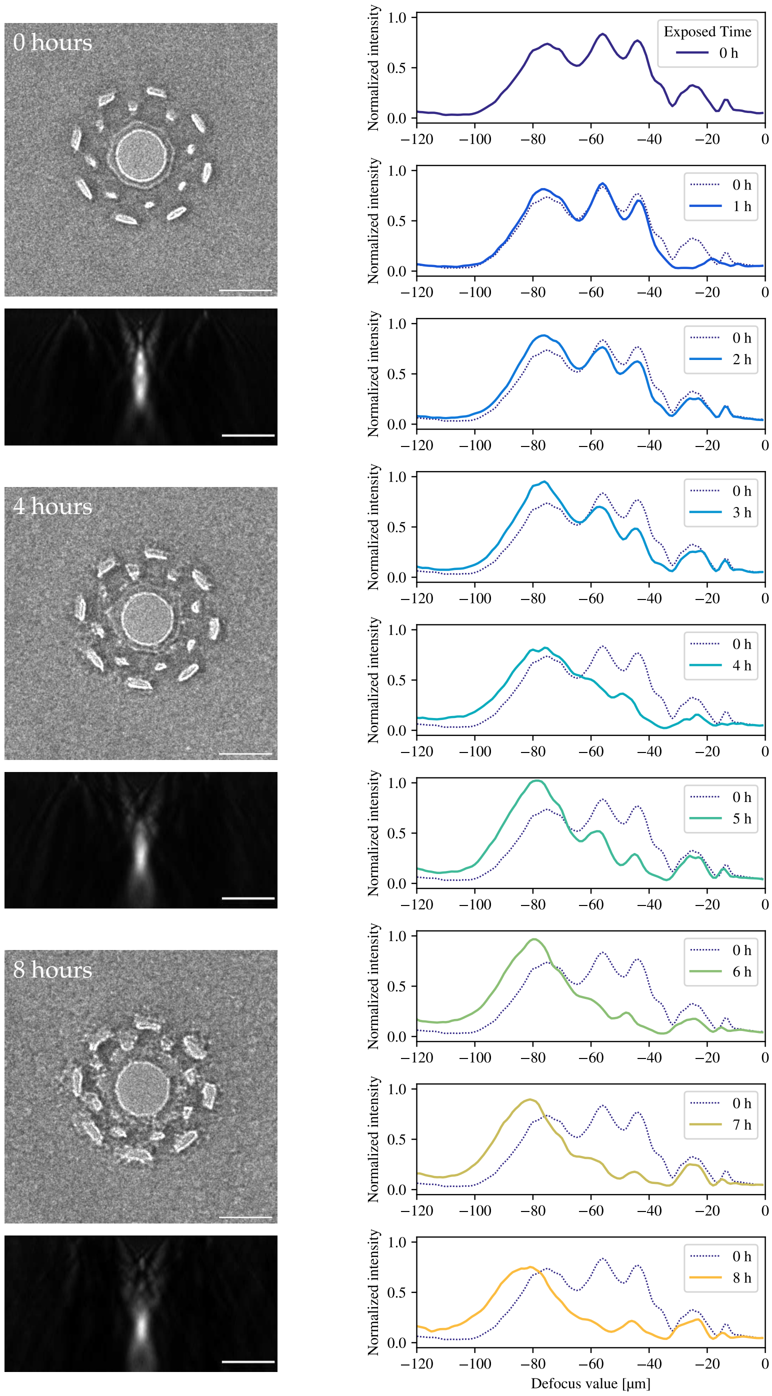

(A) **(B)**

Figure 4.39: Long-term stability of diverging Fresnel lens. (A) Structural changes occur during the electron beam irradiation, resulting in altered beam-shaping properties visible in (A) the orthogonal cuts through the data cubes and (B) the focusing line profiles. Scale bars are 30 nm.

4.5.3 Array of Electron Sieves

Patterning of thin film materials allows creating multiple beam shaping elements next to each other or arranged in an array, thus generating multiple replications of the desired beam profile. This is demonstrated in the following with another structure, which is rather easy to fabricate.

In optics, a so-called photon sieve is a modification of a Fresnel zone plate and can be used as a diffractive element to focus visible light and X-rays. It consists of pinholes arranged on the Fresnel zones, i.e. on concentric rings, which distances are described by a quadratic equation. The hole sizes correspond to the width of the respective zone.[203,204] An incoming wave is diffracted at each pinhole and interferes constructively at a certain focal length. As a result, focal points are formed on both sides of the photon sieve, in contrast to the previously presented Fresnel lens. Such a structure is fabricated in this work into graphite with a thickness of 25 nm and will be called, by analogy, an electron sieve. Pinholes are patterned into the material on three rings with radii of 18, 26 and 32 nm. The pinhole diameters range from 3 to 6 nm.

A through-focus series is recorded by illuminating the electron sieve with a parallel beam and moving the specimen along the z-axis in steps of 1 µm. The objective lens focus is kept constant at its optimum value, i.e. the electron sieve is moved relative to the fixed image plane.

Fig. 4.40 illustrates the focus series for three different specimen positions: (A) overfocus, (B) in-focus, and (C) underfocus. The diffracted beam is schematically drawn in red. At the bottom, the respective TEM images of the focus series for the three positions are shown with the same contrast and brightness settings to allow comparison of the intensities. The in-focus image shows the introduced pattern of the electron sieve. To highlight the pattern, the specimen is put slightly below the image plane resulting in a small defocus to increase the phase contrast. On both sides of the specimen, focal points with sharp intensity spots are formed. For the underfocus image, a line profile across the focus, indicated by the yellow dotted line, is given as inset in the TEM image. The focused electron beam generated by the electron sieve has a full width at half maximum of about 4 nm with an intensity enhancement by a factor of about 3.5 relative to the background. An orthogonal cut through the data cube of the entire defocus series along the axis of the yellow dotted line is shown in Fig. 4.41. As can be seen, almost no contrast is visible for the in-focus image. For small defoci, the pattern of the electron sieve, i.e. the introduced pinholes, appears with inverted contrast for the over- and underfocus, respectively. With increasing defocus, the created focal points emerge on both sides, and then fade out again.

A regular 4x4 array of the electron sieve is patterned into graphite as shown in the TEM image in Fig. 4.42. The array is used as an Hartmann-Shack detector to

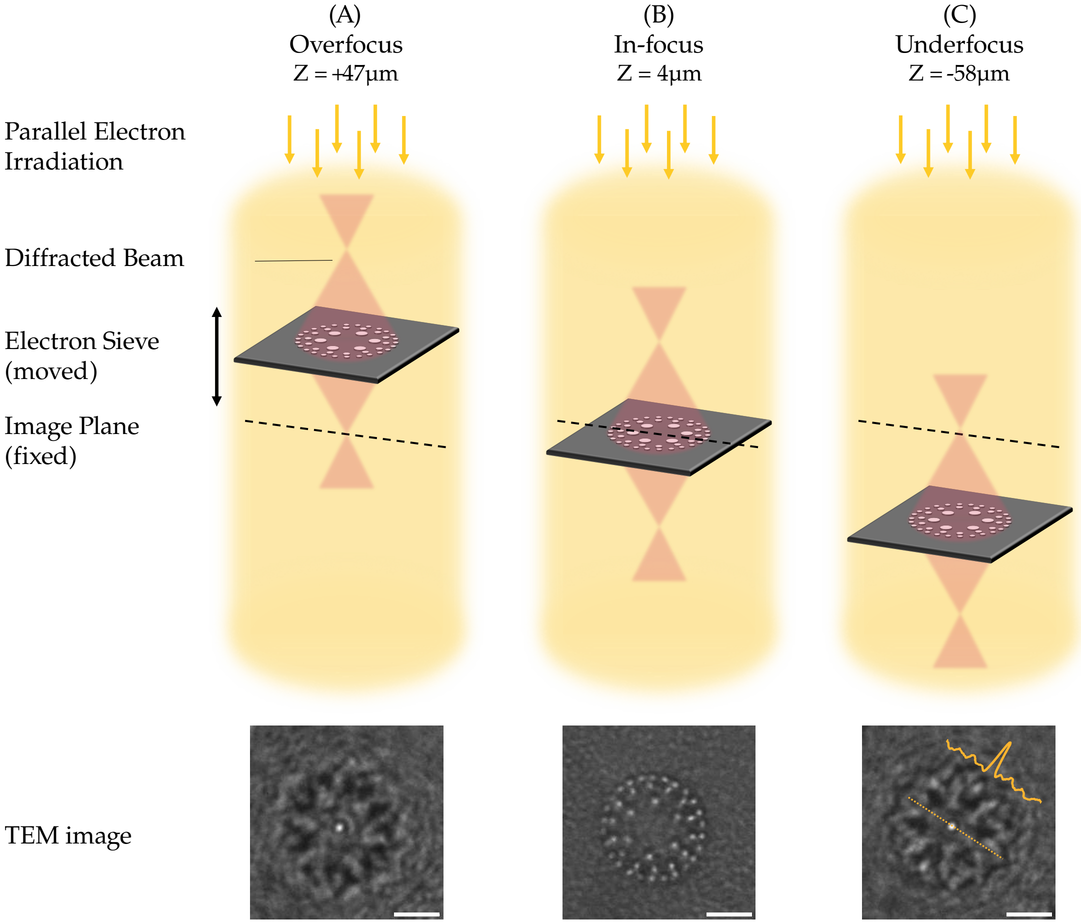

Figure 4.40: Through-focus series of a fabricated electron sieve. While keeping the image plane fixed, the lens is moved along the z-axis using the microscope stage. For the overfocus, in-focus and underfocus, TEM images are exemplarily shown in the lower part. Scale bars are 30 nm.

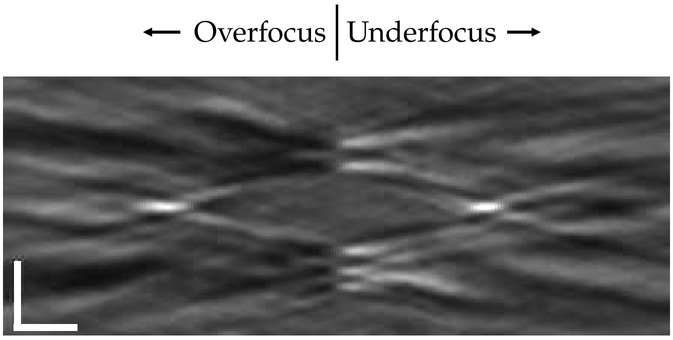

Figure 4.41: Orthogonal cut through data cube of focus series. Scale bars are (vertical) 30 nm and (horizontal) 20 µm.

examine the incoming electron beam for aberrations: A plane wave illuminating the lens array creates a regular array of focal points. In contrast, a distortion of the focal point array is observed for an aberrated illumination. The concept of an Hartmann-Shack detector is illustrated in Fig. 4.42.

In the lower part of the figure, the experimental realization for an astigmatic electron beam is shown. When imaging the introduced structures (see Fig. 4.42 B), the array can be observed as it is patterned. However, imaging the focal points of the electron sieves, see (A) and (C), reveals the aberration of the electron beam by a distortion of the array. While the positions of the as-patterned array are on a regular lattice with small deviations, clear distortions resulting in parallelograms can be seen for the under- and overfocus. The distortions occur along two axis which are rotated by about 90°.

In addition to the astigmatic beam, a pristine (i.e. aberration-free) and a convergent beam are used to illuminate the specimen and the same procedure is applied to examine the beam aberrations. The results for the three beam conditions are shown in Fig. 4.43. Here, the overfocus images are given and for each electron sieve a vector is plotted that points from the overfocus focal points towards the underfocus focal points. The amount of the distortion is indicated by the length of the vectors as well as their color. For the pristine beam, the distortion is very small, while for the astigmatic and the convergent beam, clear distortions with preferred directions can be seen.

To examine higher order aberrations, a larger array of electron sieves is required. This is simulated for an array consisting of 10x10 electron sieves. By modifying the phase of a plane wave with different Zernike polynomials, the aberrated electron beam is created. In addition, the phase shift due to the electron sieves is applied to the wave. The resulting wave is propagated to the under- and overfocus and the positions of the focal points are determined. The displacement between the points is shown as vector plot in Fig. 4.44 with the respective aberration. As can be seen, the determined distortion corresponds well to the applied geometry of the aberration. In addition, the distortions of the simulated detector for the astigmatic and defocused beam show the same orientation as for the experimental array.

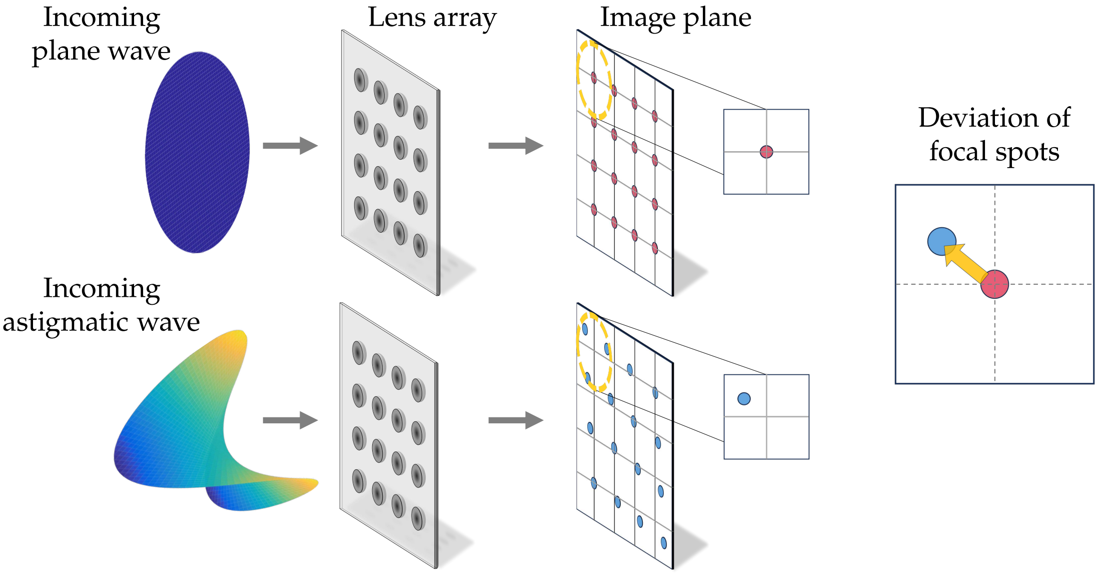

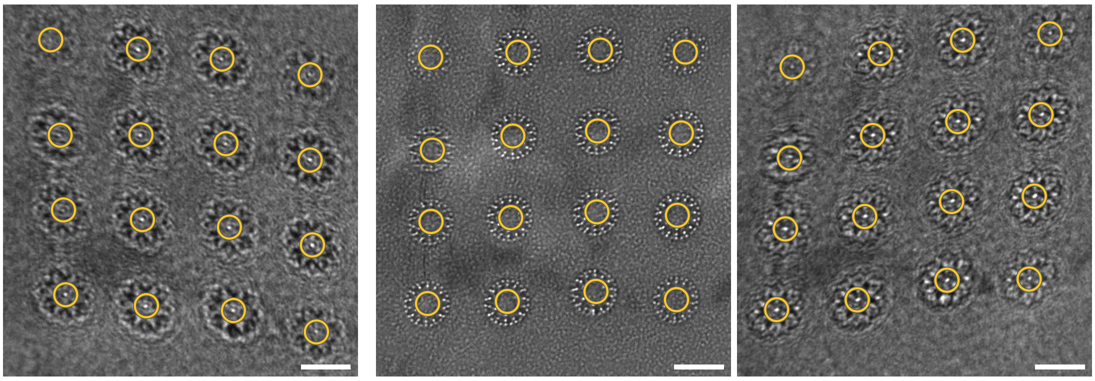
(A) Overfocus (B) In-focus (C) Underfocus

Figure 4.42: (Top) Principle of an Hartmann-Shack detector. For an incoming plane wave, the lens array creates a non-distorted array at the image plane. However, an aberrated wave leads to a distortion of the array at the image plane, which can be used to identify the wave aberration. (Bottom) Application of the patterned array of electron sieves as Hartmann-Shack detector for detecting an astigmatic illumination. The in-focus image shows the as-patterned undistorted array, but in the overfocus and underfocus images, the array appears is distorted. For better illustration, the centers of the electron sieves (for the in-focus image) and the focal points are highlighted. Scale bars are 150 nm.

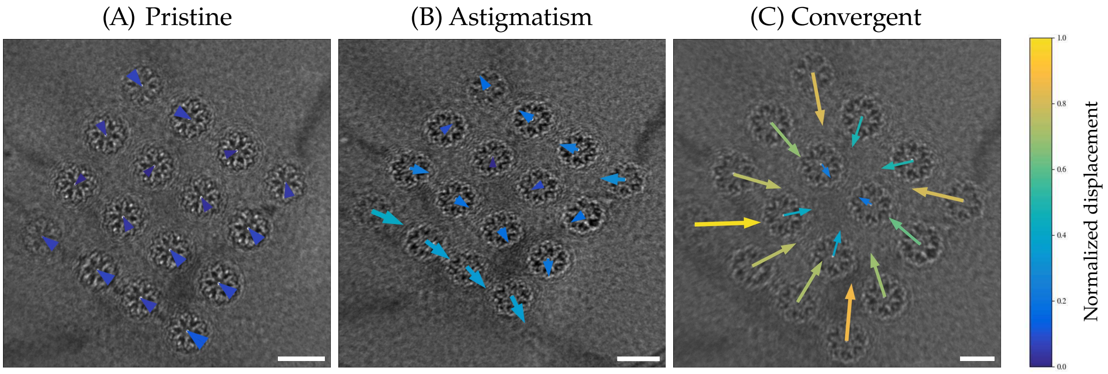

Figure 4.43: Experimental detection of different aberrations in the incoming electron beam. (B) Astigmatism and (C) a convergence angle are applied to the condenser system of the TEM. The distortions of the array are extracted and compared to the pristine beam (A). Scale bars are 100 nm.

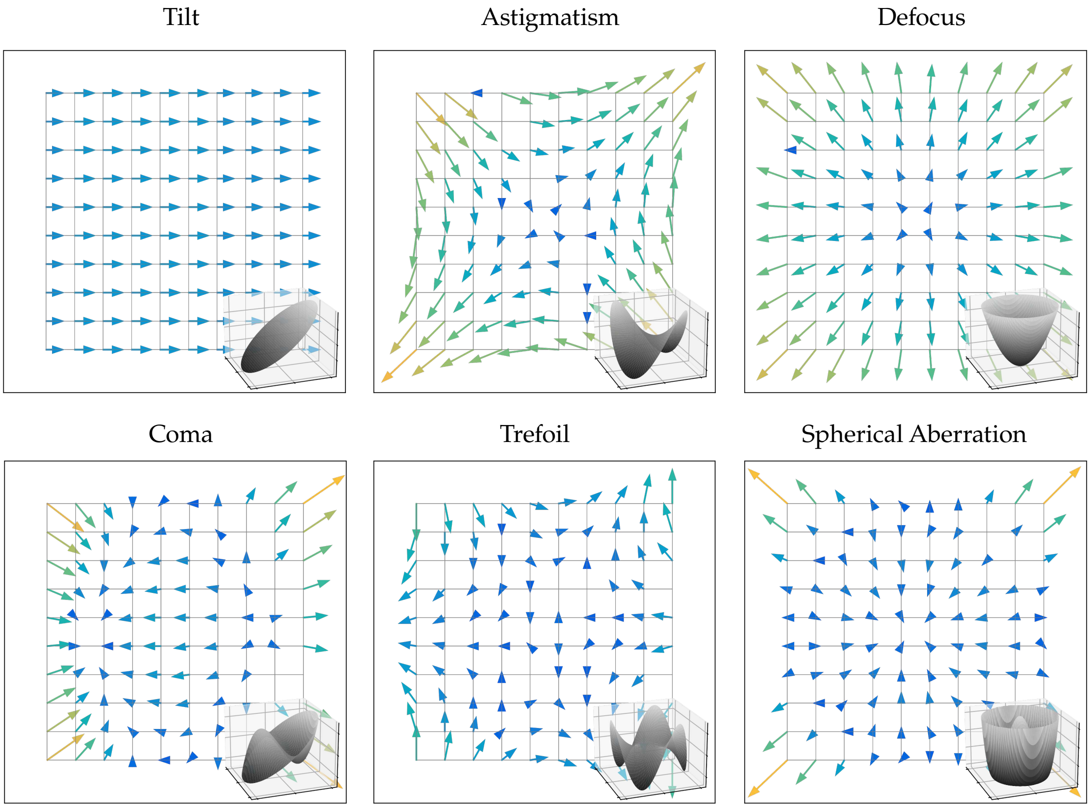

Figure 4.44: Simulated detection of different aberrations. The use of a larger array enables the identification of higher order aberrations.

Chapter 5

Discussion

5.1 Patterning 2D Materials on Nanometer Scale

Introducing patterns into materials is the key to create complex and functional structures and shapes in both the macroscopic and microscopic worlds. For example, in semiconductor manufacturing processes, circuits are built by patterning the individual layers of the semiconductor chip. Patterning methods can be evaluated based on several factors. These include minimum feature size (i.e. resolution), processing speed and therefore maximum feature size in a reasonable amount of time, reproducibility, and the ability to maintain the integrity of the rest of the material.

At the nanometer scale, there are several patterning techniques. Particularly for semiconductor manufacturing, state-of-the-art is optical lithography. In short, a photoresist is applied on the sample and subsequently exposed by short-wavelength photons through a photomask known as reticle. In a series of following process steps, the pattern of the mask is eventually transferred into the sample. Progress in the semiconductor industry, which is closely linked with progress in many other areas, is based on the improved resolution of patterning chips: In recent years, technological advances in implementing extreme ultraviolet (EUV) lithography have enabled feature sizes in the range of tens of nanometers, allowing higher transistor densities to be achieved. However, optical lithography on this scale not only requires very expensive equipment, but also a large number of process steps in order to transfer the desired pattern from the reticle into the sample.

Alternative methods exist to introduce patterns without using photomasks. For example, electron beam lithography exposes an electron sensitive resist by scanning a focused electron beam across the specimen. The patterned layer is then obtained using subsequent processes similar to those in optical lithography. While electron beam lithography can easily produce structures on the order of tens of nanometers, the resolution comes at the cost of the slow speed of being a sequential method.

2D materials have been patterned with optical lithography[205,206] and electron beam lithography[109,207] for building devices and bandgap-engineering. However, contamination and changes in the properties of the 2D material can occur due to residual photoresist or interaction with solvents.[208,209] In general, the use of wet-chemistry should be avoided as far as possible. Furthermore, the achievable resolution is limited when using a resist for introducing patterns into the 2D material.[188]

For the sake of completeness, site-selective growth of 2D materials also allows for a certain degree of patterning. Wu et al. pre-patterned a copper foil with PMMA dots, serving as nucleation seeds for the growth of graphene to create regular arrays of the 2D material.[210] Selective patterning of a 2D material by means of laser irradiation has been used by Li et al. in order spatially control the growth of vdWHs.[99]

Highest resolution down to the atomic level combined with great flexibility is only possible with so-called “direct-write” methods on the pure, freestanding 2D material. They provide an alternative to classical multi-step lithography by directly introducing the pattern in the target material without the need for a photomask or resist. As with electron beam lithography, the pattern is introduced sequentially. Therefore, patterning takes longer compared to optical lithography, but no additional process steps are required. Several direct-write methods can be applied to 2D materials. In this work, EBIE, FIB milling and STEM sputtering are used and will be discussed and compared in the following in terms of the above mentioned criteria of patterning techniques. In addition to these methods, 2D materials have been patterned by means of other direct-write techniques, such as EBID[189,211], focused laser writing[212,213] and scanning tunneling microscope (STM)-based processes.[214]

EBIE is used as a simple method to pattern graphene for the subsequent aligned stacking process. Advantageously, this can be done in the same electron microscope, avoiding a transfer between patterning and stacking. The patterns introduced are designed to allow control and later evaluation of the stacking process and are therefore not optimized to the last detail. Typical feature sizes produced are around 100 nm, e.g. the radius of the hole and linewidths of the structures in Fig. 4.1. Smaller structures in the order of a few tens of nanometers are possible, which have also been shown in the literature[215,216], but not in a reproducible manner within the scope of this work. On the one hand, this could be due to the lack of stability of the rather old electron microscope, especially of the stage: Drifting of the stage during patterning after moving to the region of interest often deformed and enlarged the introduced patterns. In newer microscopes, the stability of the stage has been greatly improved, and dedicated patterning software is available, allowing drift to be corrected. On the other hand, irregular distribution of contamination on the graphene, as can be seen in Fig. 4.1 A, can result in uneven etching. This also explains the rough edges of the introduced patterns, as shown in Fig. 4.2.

Patterns of similar sizes can be fabricated by means of FIB. The ions transfer enough kinetic energy on the atoms of the specimen to be sputtered. This process is referred to as FIB milling and is often employed to expose the region of interest in a bulk sample for further investigations. For 2D materials, FIB milling has been used to pattern the material on a support [217,218] and as a freestanding membrane [219,220], even for the fabrication of functional devices. [221,222] The interaction between the incident ion and the carbon atoms of graphene has also been studied theoretically for different ion species. [223]

Typically, the 2D material is patterned in a helium ion microscope, which is capable to generate structures in the order of 5 nm. [224] In this work, however, the gallium ion beam of a crossbeam system is used. Proper alignment of the coincidence point of the ion beam and the electron beam allows searching and selecting the region of interest purely with the electron beam to avoid damage by the gallium beam during image acquisition. Basically, both stacking and patterning can be done on the same crossbeam system. Here, however, a different microscope was used for milling, as it provides a patterning software.

Bow-tie like patterns were introduced in suspended WS_2 resulting in nanoribbons with widths of a few tens of nanometers (Fig. 4.5). However, the main application of FIB for patterning in this thesis is the creation of the predetermined breaking points for the stacking process. The lines can be introduced in a few seconds with a beam current of 10 pA, which is still a relatively low current for FIB milling, providing a powerful method for rapid structuring of the 2D material.

The third method used in this work to pattern freestanding 2D materials on the nanometer scale is sputtering by high-energy electrons in a STEM. This requires the transfer of the specimen after patterning from the STEM to the SEM for stacking, including re-mounting the specimen on different sample holders. Without special transfer equipment, this can lead to additional contamination or damaging of the specimen.

Electrons with a kinetic energy of 200 keV hit the sample as a highly focused beam. Modern microscopes, equipped with an aberration-corrector, can achieve probe sizes in the sub-ångstrom regime. [225,226] Therefore, introducing patterns and modifications with feature sizes down to the atomic level are achievable, demonstrated in the literature for example by the creation of single-atom vacancies[227,228] or the manipulation of dopant atoms in graphene or single layer hBN.[44,229]

In this work, lines and holes with sizes of about 0.5-2 nm are created using a probe-corrected STEM. The shape and exact size of the holes on this scale varies slightly due to contamination on the specimen surface: The large hole array shown in Fig. 4.7 is patterned over an area with different amount of contamination, which can be seen by the brighter and darker patches. From the resulting hole sizes, it is clear that a higher dose would be required to achieve the same size when patterning in a contaminated area. To compensate for this, the contrast in an ADF image recorded before patterning, can be used to correct the dose of each structure. However, from the comparison of holes in clean areas, it can be assumed that features with sizes of 1 - 2 nm can be reproducibly fabricated over a large area.

In Fig. 4.7 A, the agglomeration of bright atoms around the edges of the holes can be seen. These atoms are sputtered metal atoms of the TMD material (i.e. molybdenum in this case). In contrast to the lighter sulfur atoms, they are not ejected into the vacuum, but remain on the sample surface and are deposited at the energetically favourable sites around defects and introduced patterns.[227] Especially for small patterns where the electron beam is focused just on a single spot, the position of the re-deposited atoms is not controllable and can be another the reasons for the variation in hole size and shape.

In contrast, for the array in Fig. 4.7 B, the agglomeration of the metal atoms occurs in a controlled manner evenly around the hole. This is due to patterning sequence used here: Rather than focusing the beam on a single point for a given time, the beam is scanned spiralling outwards. The importance of the patterning sequence is illustrated in Fig. 4.8. Making a hole in a line-wise manner will produce an uneven agglomeration with many atoms in the patterning direction, whereas patterning spirally produces an even distribution. Introducing a disc line by line as shown in Fig. 4.8 B, result in a structure attached to the side facing the patterning direction. On the other hand, an almost freestanding disc of the 2D material can be created by spirally patterning and thus uniformly removing the material. The resulting disc remains centered and supported by only a few strings consisting of residual TMD atoms and amorphous contamination. This 2D quantum dot like structure might be interesting e.g. in nano-optics.

In Section 2.5, several beam damage mechanisms have been introduced and considered regarding nanopatterning. For high-energy electrons, knock-on damage (i.e. sputtering) is assumed to be the dominant mechanism. The required electron dose for introducing the patterns into TMDs monolayers was found to be approximately 2×10^7 electrons per nm^2. Comparing the dose with the knock-on damage cross section (see Eq. (2.13)) confirmed sputtering to be the dominant mechanism.[200]

In the present work, no significant difference of the required dose for introducing patterns in different TMD materials was observed. The threshold energy for displacing the sulfur atom in the MoS_2 and WS_2 is hardly different,[185] thus the amount of contamination on the specimen played a bigger role. For proper comparison, perfectly clean 2D materials would be necessary.

Sputtering with the high energy electron beam of the STEM allows the creation of extremely small features in a rather slow process compared to EBIE or FIB milling. Larger patterns can also be introduced with processes lasting several hours, as shown in this work for the phase plates. Here, the stability of the specimen, the microscope stage as well as the electron beam is important. Therefore, the specimen is loaded into the microscope and the necessary alignments are made the day before the patterning process. With sufficient stability, a specimen tilt can limit the maximum size of the pattern without a re-adjustment during the process to compensate for height differences. In addition, the quality of the focused electron probe decreases with very large beam shifts above ± 5 µm.

Contamination in electron microscopy is a well-known problem, and is particularly serious in the context of 2D materials. Its origins, consequences and mitigation strategies have been the subject of many works and publications, e.g. Williams & Carter[143], Hugenschmidt et al.[178], Hirsch et al.[230], Algara-Siller et al.[231].

As mentioned above, cross-linked contamination on the specimen may result in different doses being required to achieve the same patterning result in different locations. In addition, short-chain hydrocarbons diffuse over the specimen surface and play an important role during patterning. These mobile contaminants are polymerized under the electron beam and form a layer of contamination instead of introducing the desired pattern into the sample material. The resulting concentration gradient of the mobile species lead to a directed diffusion towards the electron beam, providing the supply for this undesired electron beam induced deposition. Therefore, it is important to reduce the amount of hydrocarbons on the specimen before starting the patterning process by baking-out the sample before loading into the microscope. Applying a beam shower temporarily stops the supply of mobile contamination, providing an adequate solution for patterns lasting less than one hour. In order to avoid beam induced deposition due to contamination over a longer period of time, an *in situ* method for reducing the amount of mobile contamination should be used, as for example patterning at elevated temperature,[232] laser cleaning,[233] mechanical cleaning[234] or using an UHV-TEM.[235–238]

In addition to the achievable resolution and feature size, patterning speed and reproducibility, the integrity of the surrounding material as well as material selectivity should be considered when evaluating patterning methods.

Although EBIE creates relatively rough edges, the surrounding material is still intact in terms of its crystal structure, indicated by the FFT of Fig. 4.2. However, the graphene is covered by a large amount of amorphous material, which is probably the deposition of mobile contamination during imaging in the SEM. Ultra-high vacuum and extensive heating could help to reduce this problem. Besides unwanted deposition of contamination, residual etching agent of the GIS on the sample surface can damage the specimen during electron beam irradiation. Thus, extensive imaging immediately after patterning should be avoided.

The structures introduced by means of FIB milling show an amorphous region around the edges with a width of about 30 - 40 nm. Amorphization is a common problem using the FIB, e.g. when preparing TEM lamellas. To reduce the width of the damaged region, lower beam energies or larger ion species such as for example Xe can be used.[239,240] Next to the amorphous regions, the 2D material is still crystalline, however, covered by a significant amount of contamination deposited probably by unwanted EBID during imaging. Therefore, FIB milling can be used to introduce large patterns, as long as the crystal structure and its associated properties are not relevant in the surrounding regions, such as for the predetermined breaking points used for the aligned stacking method.

In contrast, the surrounding material remains perfectly crystalline and intact when patterning with the high energy electrons in a STEM, except for the re-deposited atoms at the edges of the patterns. Some typical point defects are visible in the 2D material (e.g. in Fig. 4.7 A), originating from imaging before or after the patterning process.

Regarding the material selectivity of the different patterning techniques, both FIB milling as well as sputtering with high-energy electrons rely purely on momentum transfer, allowing to create patterns in all the 2D materials used in this thesis. EBIE, however, is a chemical etching process and thus exhibits material selectivity. Water is used as etching agent in order to pattern organic materials, i.e. graphene. In contrast, TMDs are almost not affected by water-assisted EBIE.

Since TMDs are almost not affected, water-assisted EBIE can be used to produce more complex geometries such as under-etched structures.

Other etching agents can be introduced into the chamber to enable structuring of different materials.[241] It has been shown, that a monolayer graphene can act as etch-stop when etching vdWHs with XeF_2.[242] Thus, the choice of an appropriate etching agent in combination with the spatial resolution of EBIE can enable the creation of complex structures and devices, providing a high control of the etching depth with atomically thin etch-stops as well as the possibility to under-etch certain regions.

Photoluminescence of Patterned WS_2

Effective band-gap engineering of 2D materials requires manipulation of the materials on the smallest scale down to the atomic level.[107,108,113] As described above, direct-write methods allow extremely small features to be introduced into freestanding 2D materials. Therefore, direct patterning with the high energy electron beam of the STEM has been used in this work to intentionally change the optical properties of freestanding WS_2. In fact, a massive change of the PL is observed after electron beam patterning. However, instead of causing for example a spectral shift, the electron exposure degrades the PL signal. This degradation is independent of the shape of the pattern and occurs even with a parallel illumination.

The PL signal of TMD monolayers is known to be very sensitive to structural defects, significantly more than e.g. Raman spectroscopy.[243] Besides the deterioration of the A-exciton peak, the emergence of a broad peak at higher wavelengths is observed. Similar changes in the spectrum have already been described in literature, attributing the broad peak to defects such as sulfur vacancies.[243] As described in Section 2.5, these defects are very likely to be created with 200 keV electrons. However, the comparison between the electron energies indicates that the degradation of the PL also occurs at energies well below the knock-on threshold, and becomes even worse with decreasing energy. Yagodkin et al.[244] observed spectral changes after electron beam lithography on different TMD monolayers, including the appearance of a broad peak at around 660 nm. Additional investigations indicate the relation to beam induced deposition of organic contamination: Encapsulation with hBN protects the TMDs from degradation and no low energy PL peak appears. Moreover, unprotected MoS_2 can be micromechanically cleaned with an AFM tip after electron beam exposure to locally restore the pristine PL signal.[244] Therefore, the degradation of the PL signal is attributed to a charge transfer exciton as a result of the electron beam induced deposition of contamination on the specimen.[244] Since the EBID rate increases with decreasing electron energy due to a higher amount of secondary electrons,[245] this explanation would fit well with the energy dependence found here.

In order to tailor the intrinsic properties of 2D materials by patterning with the electron beam, contamination must be avoided. Approaches such as encapsulation or high-temperature patterning[48,232] are promising methods to investigate the influence of the introduced pattern itself, e.g. spectral shifts depending on the frequency of hole lattices or confinement effects for the presented quasi freestanding disc.

5.2 Aligned Stacking

As pointed out in the introductory part of this thesis, the assembly of van der Waals heterostructures has opened up a very promising field beyond 2D materials. Mechanical stacking approaches have been developed allowing the assembly of 2D materials, comparable to Lego with atomically thin components. So-called deterministic methods control the alignment of the individual layers under an OM, achieving assemblies with a precision in the order of 1 µm. The required setup is relatively simple and stacking can even be performed in a protective atmosphere or vacuum.[246] However, these methods typically use a carrier medium for the atomically thin materials, preventing high-resolution patterning of the layers prior to assembly. Of course, freestanding membranes on perforated support films as used in this work, can also be stacked under an OM to enable the assembly of pre-patterned thin materials. This has been shown in this thesis for the fabrication of the Fresnel lens. Nevertheless, introduced patterns on the nanometer scale cannot be aligned with respect to each other due to the resolution limit of the OM.

Stacking 2D materials as freestanding membranes in an electron microscope allows the creation, observation and alignment of nanopatterns during stacking, making it an additive manufacturing method at the atomic or nanometer scale. The invented method relies entirely on the adhesion between the 2D material and the substrate (or a previously placed 2D material) and is therefore comparable to the well-established mechanical stacking methods. In other methods, temperature is used to promote the placement of the 2D material. In this thesis, several measures are used to ensure sufficient adhesion to transfer the 2D material from the perforated carrier onto the substrate.

Predetermined breaking points are introduced at the edge of the freestanding area to reduce the required force and facilitate removing from the carrier. In addition, the TEM grids are chosen to have large hole sizes in order to increase the contact area between freestanding 2D material and substrate. Holes smaller than 10 µm were tested, but they required weaker breaking points and showed a significantly lower success rate for the stacking process. The adhesion to the substrate might be improved by using a different material, e.g. gold is known to have very high adhesion to many 2D materials.[247] Another important point is the geometry of the substrate. The successful stacking process depends heavily on a good contact between substrate and 2D material, which is facilitated when the target area on the substrate is protruding and represents the highest point on the substrate. A slightly bent post from a standard lift-out grid has been found to work very well, due to its easy accessibility combined with the slightly curved surface. In addition, lift-out grids can be mounted on standard sample holders for the SEM as well as the TEM.

Any tilt of the substrate, for example during mounting in the microscope, can lead to one-sided contact, tending to trigger the breaking points on one side only and failure of the stacking as shown in Fig. 4.19. A rotational axis of the manipulator which carries the 2D material and the tilt axis of the microscope stage can compensate for any misalignment. If everything is correctly aligned, however, the invented stacking method offers a very high success rate.

The precision of any mechanical stacking method is limited by two factors: the ability to see alignment features with the observation method used, and the accuracy of the positioning system (i.e. mechanical stage, manipulator, etc.). By using an SEM, the imaging resolution can be as good as a few nanometers. The acceleration voltage can be adjusted to make the 2D materials appear semi-transparent, allowing signals to be received from both the 2D material above and the underlying substrate or 2D material. This allows features in both layers to be observed and aligned during the stacking process. An electron energy of 12 keV proved to be the most suitable.

The piezo-driven manipulator, which carries the 2D material, is used for positioning in the x-y dimension. Depending on the exact setup, the manipulator can achieve a resolution in the sub-nanometer range for these dimensions.[248] Regarding these two aspects, it should be possible to achieve a stacking precision and hence a resolution of the additive manufacturing process of a few nanometers. Implementing the technique in a TEM could even improve the precision to the angstrom range.

However, there was another aspect that limited the accuracy of the experiment as it was conducted: The microscope stage slightly moved the sample in the x-y direction as soon as the z-axis was set in motion. The stacking process was therefore carried out with a slow but continuous z-motion to avoid these displacements. Thus, the alignment of the 2D material has to be done on the fly during the movement at a relatively fast scan speed, making it impossible to obtain high quality images, accurate measurements and perfect corrections of the alignment. The achievable precision of the aligned stacking was therefore limited to about 10 nm. This problem could be overcome with a better solution for the z-motion. Finally, a stacking process that is fully automated with image recognition and automated alignment can be envisioned, which would push the stacking resolution up to that of the electron microscope and also improve reproducibility and throughput.

The majority of the time required to produce a van der Waals heterostructure with the stacking technique is due to the pumping time of the microscope, the actual time for stacking including the manual alignment is only approx. 5 min. Assuming a patterning time of 15 min, as required for example for the structure in Fig. 4.6 A, a fabrication speed of about $10\,\mathrm{nm}^3\,\mathrm{s}^{-1}$ can be reached.[200] For the achieved feature sizes, this speed is well on the trend of other additive manufacturing techniques, as can be seen in Fig. 5.1.

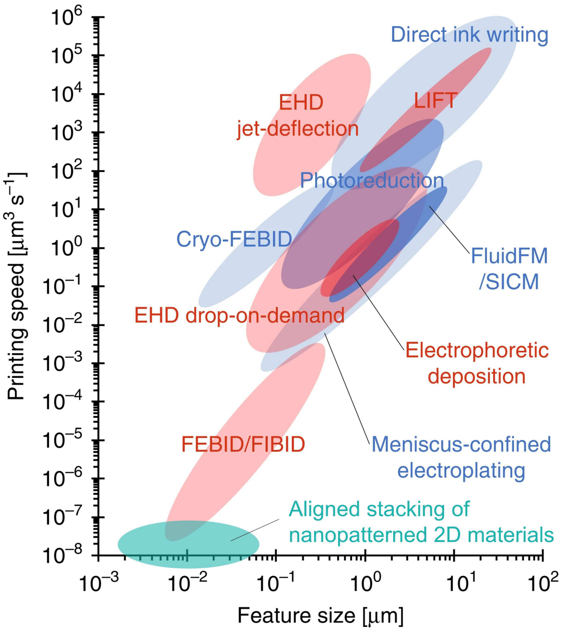

Figure 5.1: Comparison of printing speeds for different additive manufacturing techniques. The calculated speed for stacking nanopatterned 2D materials is added in green. As can be seen, for the achievable feature size, the speed matches an extrapolated linear trend. Reprinted with permission from Liashenko et al.[249]

Contamination and damage of the 2D material is another issue that cannot be ignored when considering stacking inside an electron microscope. As already discussed in the context of patterning, mobile hydrocarbon contamination is deposited under the electron beam. This is particularly critical, as the precise alignment of the layers requires extensive observation of the region of interest, leaving a significant amount of impurities on the atomically thin membranes. The result can be seen in the assembled graphene structures presented above: the crystallinity is still present, but the HRTEM images are dominated by the deposited contamination. For the TMD structures, however, no contamination can be seen on the moiré pattern. Since no precise alignment was performed in this case, a lower electron dose was applied during stacking. Moreover, contamination is less visible when imaging the relatively heavy TMD materials as opposed to graphene.

In conventional stacking methods performed in an OM, contamination accumulates in small pockets,[250] leaving most of the sample surface clean and thus making standard methods superior in this respect. In addition to the deposition of contamination, the electron beam of the SEM can cause beam damage to the specimen in terms of EBIE. This was particularly noticeable for the ten-layer stack, in which the diameter of the first hole increases by about 40% during the subsequent assembly steps. To avoid EBIE, sufficient pumping time should be allowed between patterning and stacking, preferably overnight, and a higher acceleration voltage should be selected due to the smaller electron-specimen interaction for the 2D material.

Carrying out the assembly in an ultra-high vacuum should help to prevent contamination as well as EBIE. In addition, alignment markers could be used to prevent the electron beam from altering the actual patterns. Damage to these markers is negligible.

The stacking of the quasi freestanding disc demonstrates that even fragile structures can be assembled into heterostructures. This approach can also be used to stack TMD structures which would geometrically not be stable in single layer (e.g. a truly freestanding disc). The introduced contamination stabilizes the structure and could be selectively removed after the stacking process using a chemical etching process that selectively removes the carbon contamination without destroying the TMD material, for example with an oxygen plasma.

A variation of the invented stacking technique is presented by placing the next 2D material before its pattern is introduced. This alternative approach requires the patterns to be at the same position and to be gradually smaller than in the previous layer. Therefore, not every three-dimensional structure can be realized with this method. However, the precision is then limited only by the patterning accuracy. This is demonstrated for the seven layer stack of graphene layers with successively smaller holes. In this case, the average offset between the holes is approximately 1.7 nm. This is a significant improvement in the precision compared to, for example, the ten layer stack fabricated by patterning the layers first, where the average offset was 17 nm. Moreover, for this modified method no increase of the first hole during the assembly process was observed. On the one hand, this is because less dose is applied in the SEM during stacking, as there is no need for precise alignment and observation. On the other hand, the patterns were produced by STEM instead of EBIE, so there is no residual etching agent present during stacking in the SEM.

The presented technique offers control of the x-y alignment. The twist angle between the deposited layers, however, cannot be controlled since the crystal lattice of the 2D materials is not resolvable in an SEM. Other mechanical assembly methods use the edges of the flakes to create heterostructures with a controlled twist angle, for example. In an SEM, the lattice orientation can be determined from the diffraction pattern.[251] Thus, using a camera below the sample in combination with a rotation of the stage should allow twist angle controlled assembly of nanopatterned 2D materials.

5.3 Phase Plates

The presented method for patterning, in combination with an alternative method for stacking 2D or thin materials, has been used to fabricate thin-film holographic phase plates for electrons. The ability to introduce patterns with high resolution in graphite membranes enables nanometer-scale phase plates that can generate a nanometer-sized beam profile from an incoming parallel electron wave without the need for additional demagnifying optics. In contrast to electromagnetic lenses, phase plates offer the possibility to form almost any beam shape and thus should not be dismissed from electron microscopy, despite the significant advances in modern aberration correctors.

Simulations have been used to determine the required pattern and thickness of the phase plate to achieve the desired intensity distribution and phase of the generated electron probe.

From a single exfoliation, a large number of flakes with different thicknesses are available, and the flake with the required thickness can be easily selected by rapid screening with the OM and subsequent thickness verification with the AFM. Furthermore, exfoliated graphite flakes provide atomically flat areas due to their layered structure, rather than the typical roughness of deposited thin films. The effect of roughness and the resulting thickness variation is investigated in a simulation for the demonstrated spiral phase plate. Therefore, the applied phase shift is varied locally with a gaussian distributed height variation with a maximum difference up to 3 nm.

As can be seen from Fig. 5.2, no significant change of the focusing behaviour of the phase plate occurs. Thus, using a deposited film as phase plate material would be also be possible. Similar to holography, the working principle of the phase

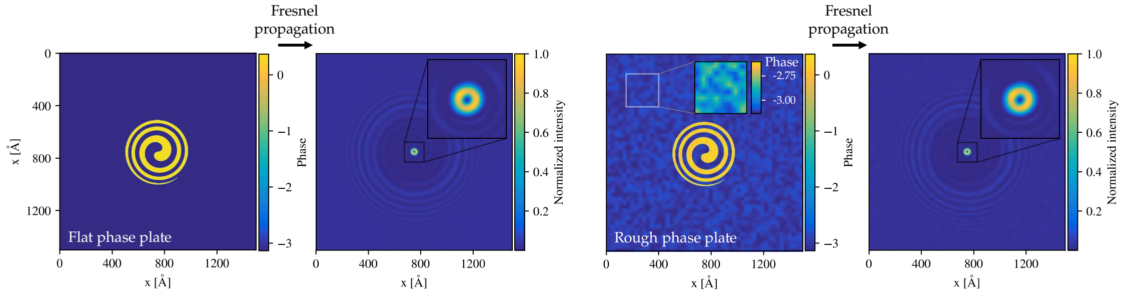

(A) (B)

Figure 5.2: Comparison of the focusing behaviour of a perfectly flat (A) and rough spiral phase plate (B). The rough phase plate is simulated by adding height variations of up to 3 nm. No difference in the intensity of the created vortex beam can be observed.

plates is relatively robust against small local variations. This is advantageous for their application as slight imperfections during the fabrication or contamination on the surface have little influence.

The demonstrated spiral phase plate creates an electron vortex beam, a beam type, which can not be generated with electromagnetic lenses. In the present case, the vortex possesses an OAM of one. However, by changing the geometry of the introduced pattern, also higher OAMs should be possible (see Fig. 5.3).

The size of the vortex is also determined by the pattern and limited by the achievable resolution. Smaller vortices can be achieved by decreasing the pattern size. Especially the outer regions of the spiral are challenging to be introduced. It is possible to reduce the number of turns of the spiral, however, at least one full turn is required for generating a proper vortex beam.

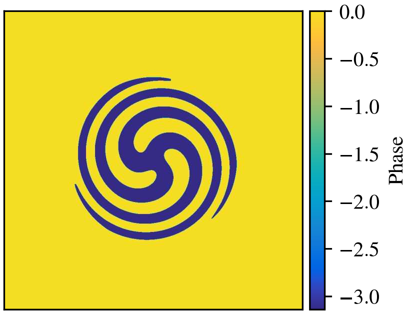

Figure 5.3: Phase plate pattern to create vortex with OAM of 3.

From the simulation, a continuous phase shift from 0 to 2π is obtained, which is then binarized and the region between π and 2π is used as the pattern of the spiral phase plate. Creating an almost continuous profile would be possible by repetitive stacking and patterning thinner layers, ultimatively by using atomically thin graphene layers. However, this approach requires many steps, is extremely time-consuming and does not significantly improve the resulting electron probe according to simulations.

Fig. 4.33 shows the generated electron vortex beam. The intensity exhibits a clear asymmetry which can be attributed to two points.

On the one hand, the asymmetry arises from the support structures, which ensure the stability of the fabricated phase plate. This is demonstrated in Fig. 5.4: The generated vortex is compared for a phase plate without supports (A) and with supports (B). The intensity of the resulting vortex shows a clear asymmetry for the latter case. While the supports cannot be omitted completely, their design might be adjusted in order to reduce the asymmetry, e.g. by making them in a more irregular manner.

Another possible reason for the occurring asymmetry is a deviation of the phase shift from the required one, which has been calculated to be π. In Fig. 5.5, the phase shift is varied from $^{1}/_{3}\pi$ to $^{5}/_{3}\pi$, demonstrating the emerging asymmetry for phase shifts that are not equal to π. Although the thickness of the graphite flake has been chosen to meet this requirement, the HRTEM image (Fig. 4.32) reveals residual amorphous material in the patterned regions, resulting in a smaller

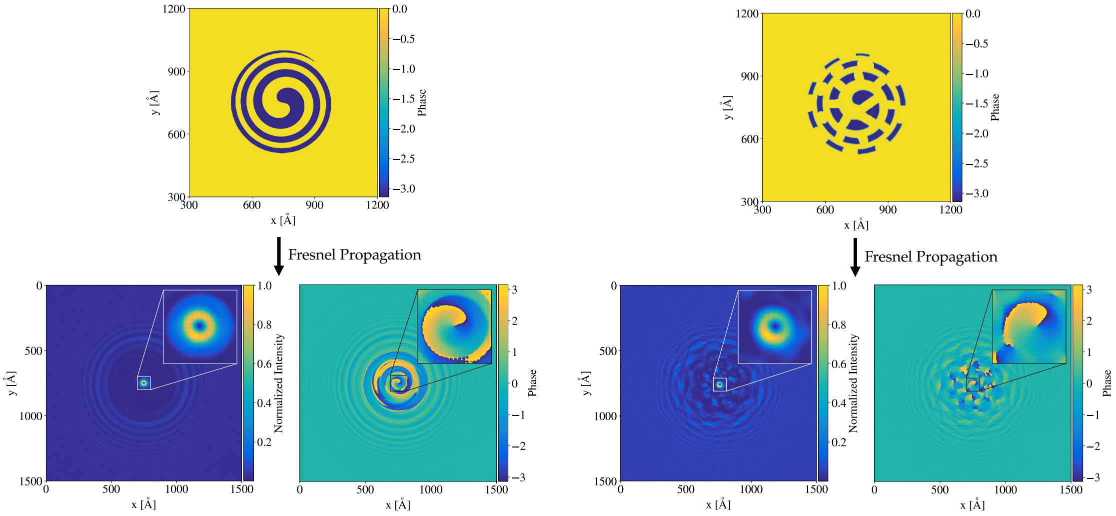

(A) **(B)**

Figure 5.4: Asymmetry in the resulting vortex beam. (A) The ideal phase plate pattern creates a symmetric intensity, while (B) adding support structures can lead to an asymmetric intensity.

applied phase shift. The residues are probably redeposited material from the patterning process. To avoid this, the patterning process should be improved, e.g. by increasing the number of repeats. Additional factors that may contribute to the deviation of the phase shift include a different mean inner potential from the one used in the calculation (as there are different methods to determine the value which give slightly different results) or a different actual height of the graphite flake (i.e. due to errors in the AFM measurement or contamination on the surface).

In previous publications, researchers have mainly used two approaches to create electron vortex beams. Y-gratings are applied as diffraction gratings, creating a set of beams with different OAMs.[163,167] An aperture can then be inserted to select the desired beam. Besides diffraction gratings, spiral phase plate have been fabricated into thin-film materials by means of optical lithography.[166] These phase plates are inserted into the condenser aperture position, thus creating a focused probe through further de-magnification by the condenser lens. The method presented in this thesis allows the formation of nanometer sized vortices without the need of additional demagnifying optics or apertures.

In the field of light optics, the Fresnel lens design was developed to minimize the amount of material required for the same focal length, allowing large but relatively lightweight lenses to be built. The design also offers advantages for making focusing electron phase plates from thin-film materials, e.g. reducing diffuse scattering which

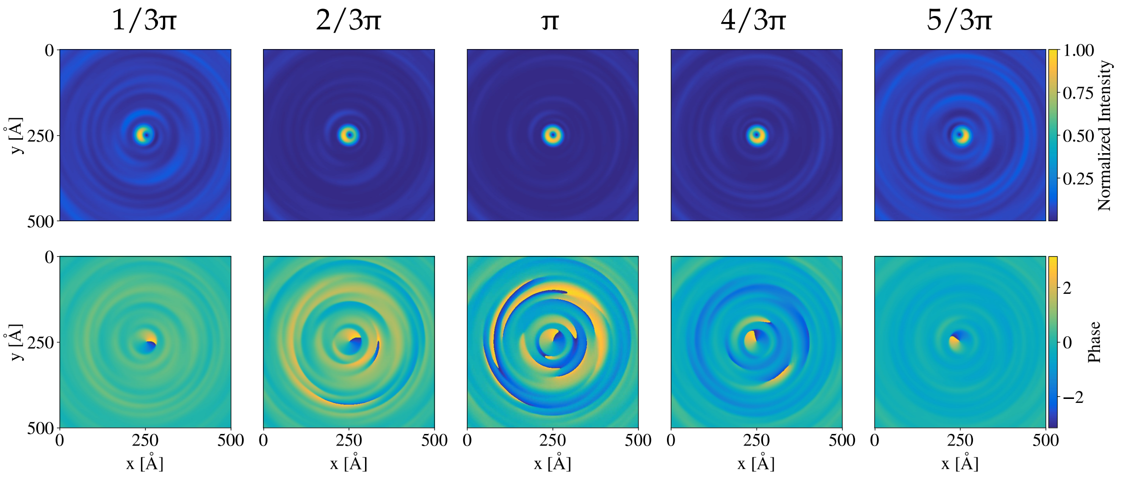

Figure 5.5: Influence of the magnitude of the phase shift on the generated vortex. For the same geometry as above, the phase shift is varied from ⅓π to ⅗π. The resulting vortex still possesses a OAM of one, however, a symmetric intensity only occurs for a shift of π.

causes a loss of intensity. In addition, patterns can be introduced with the highest resolution, enabling the fabrication of very small lenses. The size of the introduced pattern determines the focal length - for the presented Fresnel lens it is about 80 µm. In general, significantly shorter focal lengths can be achieved compared to magnetic lenses where the focal length is in the mm range. Thus, thin-film phase plates or lenses offer a unique alternative in electron optics. The combination of different phase plates allows compact and dedicated setups to be built, similar to custom optical setups in light optics.

In contrast to the above presented spiral phase plate, the Fresnel lens requires a three-dimensional structure and thus cannot be produced by a single patterning process. The pick-up technique for transferring flakes from the wafer to the TEM grid provides a simple and fast method of stacking flakes when precise alignment is not required.

The focusing behaviour of the Fresnel lens is investigated by a through-focus series in the TEM and compared with a simulated series (see Fig. 4.37). Overall, experiment and simulation match very well. However for the focus of the lens, a slightly smaller intensity enhancement compared to the background signal emerges in the experiment. Imperfect patterning may cause this deviation. Incomplete patterns, particularly at the edges, can reduce the contributing phase shifting area and therefore result in a smaller intensity. In addition, there is a slight deviation in the Z position, i.e. the focal length of the lens, which could be due to a slightly non-parallel illumination.

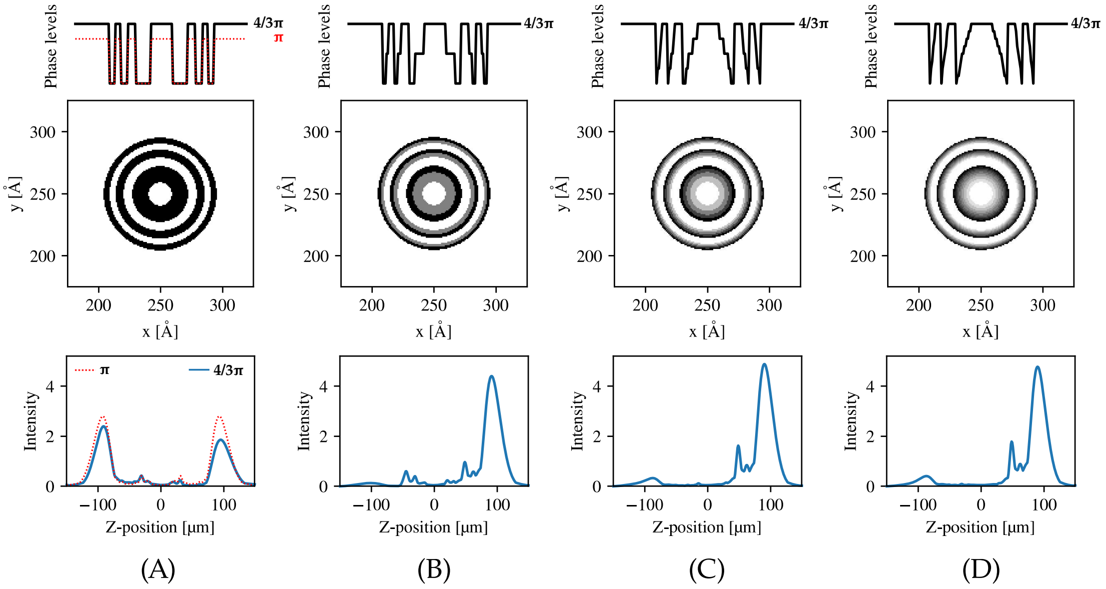

Figure 5.6: Design and focusing behaviour of the Fresnel lens for a different number of layers. (A) Using one layer results in a dominant focal point in both the underfocus and overfocus region. Depending on the magnitude of the applied beam shift, the intensity can be symmetric or asymmetric. (B-D) Additional layers allow a smoother phase profile and suppression of the underfocus focal point. However, no significant improvement can be achieved by having more than two layers.

In order to facilitate the lens fabrication, the design consists of only two layers, giving three levels of different phase shifts. Fig. 5.6 demonstrates the effect of different numbers of layers.

For a single layer, dominant foci appears in both the under- and overfocus as superposition of Fresnel fringes. The ratio of the peaks depend on the amount of the applied phase shift: Symmetric under- and overfocus occur when applying a phase shift of π. The experimental used phase shift of $^4\!/_3\pi$ result in an asymmetry. By using a second layer (Fig. 5.6 B), the underfocus intensity peak is suppressed and the focusing properties of the lens are revealed. The ideal shape of the Fresnel lens design can be approximated by using a large number of thin layers, ultimatively by stacking atomically thin graphene membranes similar to what have been shown previously in Fig. 4.25. However, as no significant improvement in the focusing behaviour can be achieved, only the simplest lens design was realized in this work.

By modifying the pattern of the second layer, the phase profile can be inverted to create a diverging Fresnel lens. As expected, the through-focus series shows a dominant focal point in the underfocus region, in contrast to the converging Fresnel lens. The ability to have both converging and diverging lenses for electrons increases the possibilities when considering the use of phase plates as optical elements in electron optics.

For the diverging Fresnel lens, the long-term stability under electron beam irradiation is investigated. The interaction between the phase plate material and the electron beam can not be avoided for this type of phase plate. In the present case, a clear degradation of the phase plate structure could be observed during the 8 h exposing time, significantly affecting also the focusing behaviour. To ensure a stable operation over a longer period of time, measures to increase the stability of the phase plate should be considered. These include heating the phase plate during application or operating the phase plate in a better vacuum, both of which reduce chemical etching and carbon deposition. Moreover, protective layers can be added, e.g. metals or 2D materials that are less prone to etching such as TMDs. In this case, the phase shift caused by the additional layer must be taken into account when simulating the wave propagation and deriving the phase plate design.

In contrast to the Fresnel lens, the electron sieve acts as a diffractive lens and creates foci in both the underfocus and the overfocus regime. Fig. 5.7 shows the line profile across the center of the orthogonal cut through the data cube of the recorded through-focus series. As it can be seen, the two focal points exhibit similar intensities. This is to be expected as the graphite flake used for the electron sieve is about 25 nm thick, producing a phase shift of π for an 80 keV electron and thus resulting in a symmetrical under- and overfocus, as demonstrated in Fig. 5.6 (red dotted curve). In addition to the intensities, the focal lengths are expected to be the same. However, in the experiment, the focal lengths are slightly different (47 µm for the overfocus, 58 µm for the underfocus), which is probably due to a non-perfect parallel illumination in the TEM.

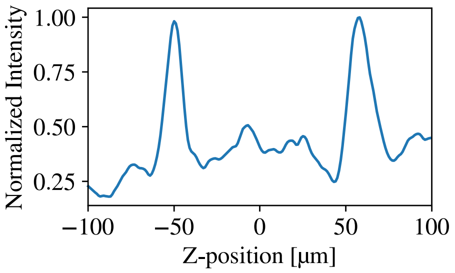

Figure 5.7: Focusing behaviour of electron sieve.

The phase plate approach presented here makes it easy to fabricate an array with multiple elements, resulting also in multiple electron probes. This allows parallelization, e.g. when investigating a magnetic sample with the electron vortex beam or during an electron beam lithography process with a set of Fresnel lenses.

In this work, a regular array of electron sieves is applied as an Hartmann-Shack detector, which reveals aberrations in the incoming wave by a distortion of the focal point array. The observed distortion of the regular array for lower-order aberrations is in principle also visible for any other structure of the specimen, but the distinct points allow a more precise examination. Indeed, the displacement could be measured in order to quantify the aberration.

Especially when considering higher orders, the observed distortion of an object can sometimes no longer be clearly assigned to a certain aberration. For example, defocus and spherical aberration might result in a similar distortion of a simple object. The same applies to a small 4x4 array as used in the experimental Hartmann-Shack detector. However, by increasing the number of elements, higher-order aberrations can be distinguished due the higher number of markers, as demonstrated in the simulation (see Fig. 4.44).

In reality, several different aberrations are present in the beam. Therefore, the resulting superposition of all the distortions must be separated to obtain the individual aberrations.

Chapter 6

Summary & Outlook

In this thesis, a novel method for the fabrication of van der Waals heterostructures has been developed which allows for the aligned mechanical assembly of individual 2D layers with nanometer precision. Based on stacking inside a scanning electron microscope, the method overcomes the limitations of previous techniques and thus enables 3D structures to be assembled from nanopatterned 2D materials.

Several methods for nanopatterning of freestanding 2D materials were initially considered, particularly with regard to the stacking process. Three direct-write methods have been applied, introducing the structure sequentially without the need of additional process steps. These methods were examined and evaluated in terms of resolution, processing speed, reproducibility, the ability to preserve the integrity of the surrounding material, and material selectivity. EBIE and FIB milling allow large patterns to be created from the nanometer to the micrometer scale in a relatively short period of time. Thus, they are suitable for introducing marker structures or the predetermined breaking points required for the stacking technique. For more accurate patterns, such as the functional structures of a device, sputtering with a focused high-energy electron beam should be used. The small probe size of a STEM allows the manipulation of 2D materials on the atomic scale.

High-resolution patterning is necessary to tailor the properties of 2D materials, such as band-gap engineering. Direct patterning of freestanding WS_2 monolayer is conducted and investigated for changes in the PL. The PL spectrum showed a degradation, which was dependent on both the electron dose and energy. The degradation is likely due to electron beam induced deposition of hydrocarbons on the specimen. Thus, to tailor the optical properties of 2D materials in future work, methods such as encapsulation or in-situ heating will be required to avoid contamination. This would allow for the customization of the single-layer assembly units for the newly developed mechanical stacking technique.

The assembly of the nanostructured, freestanding 2D materials is performed in an SEM, allowing for a precise observation of the alignment of the layers. Movements for the alignment are carried out using a piezo manipulator. Deposition of the 2D material on the substrate or onto other 2D layers is purely based on adhesion, thus no additional measures such as temperature changes or sacrificial polymer films are necessary. Only the 2D membrane without the carrier film is placed on the substrate, allowing the stacking process to be repeated to apply additional layers. The method is universally applicable to all 2D materials, as demonstrated in the fabrication of various material combinations. The precision of the assembled structures was examined by measuring the offset of marker structures. A precision of approximately 10 nm could be realized. With a small modification of the method, applicable only to some 3D geometries, a precision of less than 2 nm was achieved for the resulting assembly.

The developed assembly technique enables the creation of tiny 3D structures. This is utilized to manufacture thin-film nanometer sized holographic phase plates from patterned graphite membranes. Their ability to generate the desired electron probe is investigated in the TEM. Due to the flexibility of the method, a variety of different beam shapes can be generated. The phase plate design is derived by simulating the electron wave propagation. The small size of the phase plates allows the generation of nanometer sized focused electron probes from a parallel illumination without the need for additional demagnifying optics, as demonstrated with the presented Fresnel lens. The phase plates offer control of both the resulting intensity and phase of the electron beam. This allows creating complex beam profiles, as shown for a nanometer sized vortex beam with a defined orbital angular momentum. Furthermore, multiple phase shaping elements can be introduced on a small area, potentially opening up the possibility of parallelization e.g. in lithographic methods. In the present work, an array of focusing elements is manufactured and applied as a Hartmann-Shack detector for electrons. The possibility of detecting low order aberrations in the electron illumination has been demonstrated experimentally and has been simulation for higher order aberrations.

In summary, the novel stacking method enables the layer-by-layer assembly of nanometer sized 3D structures from individually patterned 2D materials. It can be considered as a method of additive manufacturing with nanometer precision, and another step towards the dream of creating objects with atomic precision.

Outlook

The invented assembly method expands the possibilities in the field of van der Waals heterostructures. However, the method itself has the potential for further improvement. One key challenge in the fabrication of functional structures is the minimization of electron beam induced deposition, particularly in the stacking process. Various *in situ* methods, such as mechanical and laser cleaning as well as specimen heating, should be investigated and used in conjunction with ultra-high vacuum systems. Appropriate sample treatment and vacuum transfers between different systems can minimize the presence of mobile hydrocarbons. Additionally, gaining control over the twist angle between the individual layers during the assembly would connect the nanofabrication to the field of twistronics. Recording the electron diffraction pattern with a camera below the specimen should allow for the determination of the lattice orientation of the individual 2D materials.

The precision achieved is not a physical limit of the method, but rather instrumentally constrained. Thus, the precision could be improved by enhancing the stage stability and using software-assisted image recognition for the alignment. Indeed, even the resolution of the scanning electron microscope may not be inherently limiting, as the centers of structures can be determined with greater precision than the resolution, similar to the principles employed in many optical superresolution techniques.

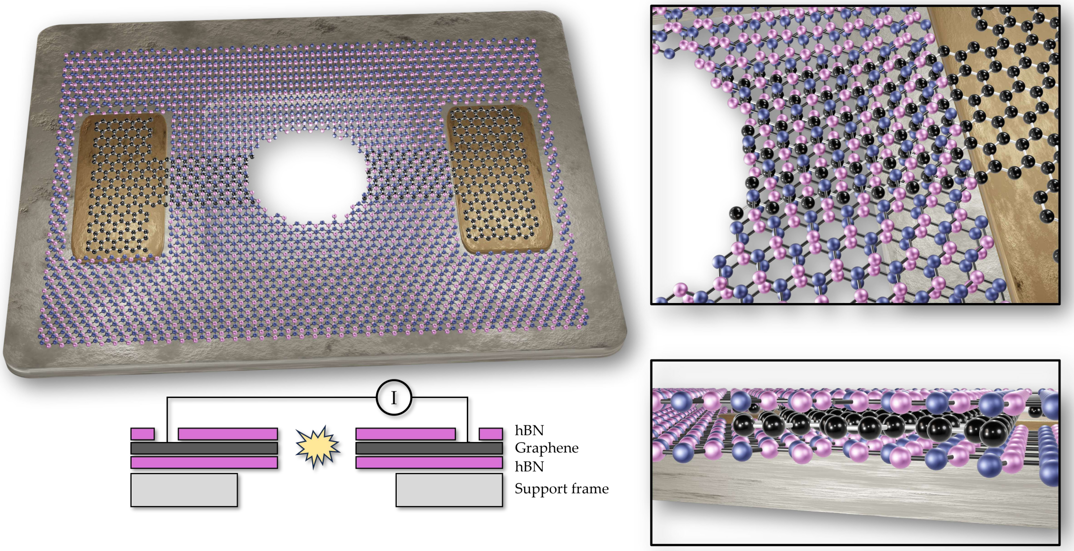

Figure 6.1: Hypothetical tunneling nanopore fabricated by stacking nanopatterned graphene on hBN. A top hBN layer is applied to ensure electrical isolation between the two contacts. The nanopore can be patterned after the assembly, splitting the graphene nanoribbon and thus creating the tunneling contacts.

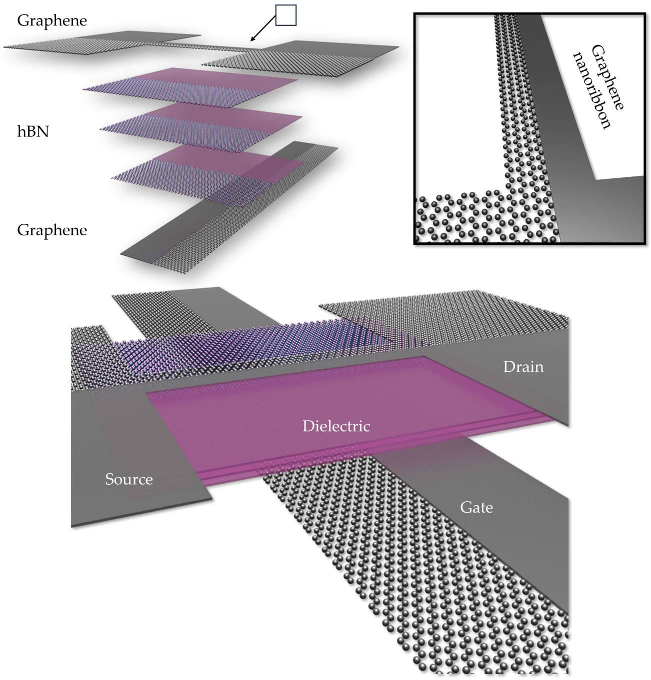

Figure 6.2: Illustration of a transistor structure consisting of stacked and patterned 2D materials. A nanoribbon is introduced into graphene, creating a single atom layer that serves as the source, drain as well as active element of the transistor. Another graphene layer can be used as gate electrode, separated by hBN layers as dielectric. Reprinted with permission from Haas et al.[200]

The method enables the creation of functional structures from patterned 2D materials on a very small scale. The flexibility in the possible 3D structures could enable the realization of solid state tunneling nanopores for molecular sensing. The idea is illustrated in Fig. 6.1. A graphene nanoribbon is encapsulated between hBN layers. Subsequently, the nanopore is patterned into the hBN and the graphene. The divided nanoribbon then acts as tunneling contacts for a translocation measurement, providing additional and low-noise signals.

The different properties offered by the family of 2D materials in combination with the precise assembly of these nanopatterned atomically thin films allow novel electronic and optoelectronic device geometries. A theoretical transistor structure is given in Fig. 6.2. A graphene nanoribbon is patterned to open a band gap and thus allowing graphene to serve as active element in the transistor. In addition, drain and source electrodes can be realized in the same graphene layer. A comparable device could be made by patterning an antidot lattice. By modifying the pattern and employing different 2D materials, the device properties can be tailored to specific requirements.

LIST OF ABBREVIATIONS

vdWH	Van Der Waals Heterostructure
0D	Zero-dimensional
1D	One-dimensional
2D	Two-dimensional
2D material	Two-dimensional Material
3D	Three-dimensional
ADF	Annular Dark-field
AFM	Atomic Force Microscope
BF	Bright-field
CCD	Charge Coupled Device
CMOS	Complementary Metal Oxide Semiconductor
CTEM	Conventional Transmission Electron Microscopy
CVD	Chemical Vapor Deposition
DFT	Density-functional Theory
EBID	Electron Beam Induced Deposition
EBIE	Electron Beam Induced Etching
EDS	Energy-dispersive X-ray Spectroscopy
EELS	Electron Energy Loss Spectroscopy
EM	Electron Microscopy
FEG	Field Emission Gun
FET	Field-effect Transistor
FIB	Focused Ion Beam
FT	Fourier Transform
FWHM	Full Width At Half Maximum
GaAs	Gallium Arsenide
hBN	Hexagonal Boron Nitride
HRTEM	High-resolution Transmission Electron Microscopy
$\mathbf{LaB_6}$	Lanthanum Hexaboride
$\mathbf{MoS_2}$	Molybdenum Disulfide

$MoSe_2$	Molybdenum Diselenide
$NbSe_2$	Niobium Diselenide
OAM	Orbital Angular Momentum
OM	Optical Microscopy
PCTF	Phase Contrast Transfer Function
PL	Photoluminescence
PP	Phase Plate
SEM	Scanning Electron Microscope
SiO_2	Silicon Dioxide
STEM	Scanning Transmission Electron Microscopy
STM	Scanning Tunneling Microscope
TEM	Transmission Electron Microscope
TMD	Transition Metal Dichalcogenide
vdW	Van Der Waals
WS_2	Tungsten Disulfide
WSe_2	Tungsten Diselenide
WTe_2	Tungsten Ditelluride
ZnS	Zinc Sulphide
ZrO_2	Zirconium Oxide

BIBLIOGRAPHY

[1] **Duhem, P.** *The Aim and Structure of Physical Theory.* Princeton University Press (2021)

[2] **Peierls, R.** Quelques propriétés typiques des corps solides. *Annales de l'I.H.P.*, 5(3), (1935) 177–222

[3] **Müller, U.** Zur theorie der phasenumwandlungen. *Symmetriebeziehungen zwischen Kristallstrukturen*, 11(545), (2023) 325–335

[4] **Mermin, N.D.** Crystalline order in two dimensions. *Physical Review*, 176(1), (1968) 250–254

[5] **Novoselov, K.S.**, **Geim, A.K.**, **Morozov, S.V.**, **et al.** Electric field in atomically thin carbon films. *Science*, 306(5696), (2004) 666–669

[6] **Novoselov, K.S.**, **Geim, A.K.**, **Morozov, S.V.**, **et al.** Two-dimensional gas of massless dirac fermions in graphene. *Nature*, 438(7065), (2005) 197–200

[7] **Zhang, Y.**, **Tan, Y.W.**, **Stormer, H.L.**, **et al.** Experimental observation of the quantum hall effect and berry's phase in graphene. *Nature*, 438(7065), (2005) 201–204

[8] **Boehm, H.P.**, **Setton, R.**, & **Stumpp, E.** Nomenclature and terminology of graphite intercalation compounds. *Carbon*, 24(2), (1986) 241–245

[9] **Geim, A.K.** Random walk to graphene (nobel lecture). *Angewandte Chemie - International Edition*, 50(31), (2011) 6966–6985

[10] **Ruess, G.** & **Vogt, F.** Höchstlamellarer kohlenstoff aus graphitoxyhydroxyd. - Über den ort der aktiven eigenschaften am kohlenstoffkristall. *Monatshefte für Chemie*, 78(3-4), (1948) 222–242

[11] **Boehm, H.P.**, **Clauss, A.**, **Fischer, G.O.**, **et al.** Das adsorptionsverhalten sehr dünner kohlenstoff-folien. *ZAAC - Journal of Inorganic and General Chemistry*, 316(3-4), (1962) 119–127

[12] **Land, T.A.**, **Michely, T.**, **Behm, R.J.**, **et al.** Stm investigation of single layer graphite structures produced on pt(111) by hydrocarbon decomposition. *Surface Science*, 264(3), (1992) 261–270

[13] **Shioyama, H.** Cleavage of graphite to graphene. *Journal of Materials Science Letters*, 20(6), (2001) 499–500

[14] **Gan, Y.**, **Chu, W.**, & **Qiao, L.** Stm investigation on interaction between superstructure and grain boundary in graphite. *Surface Science*, 539(1-3), (2003) 120–128

[15] **Viculis, L.H.**, **Mack, J.J.**, & **Kaner, R.B.** A chemical route to carbon nanoscrolls. *Science*, 299(5611), (2003) 1361

[16] **Geim, A.K.** Graphene prehistory. *Physica Scripta*, T146(T146), (2012) 014003

[17] **Meyer, J.C.**, **Geim, A.K.**, **Katsnelson, M.I.**, **et al.** The structure of suspended graphene sheets. *Nature*, 446(7131), (2007) 60–63

[18] **Novoselov, K.S.**, **Jiang, D.**, **Schedin, F.**, **et al.** Two-dimensional atomic crystals. *Proceedings of the National Academy of Sciences of the United States of America*, 102(30),

(2005) 10451–10453

[19] **Mounet, N.**, **Gibertini, M.**, **Schwaller, P.**, **et al.** Two-dimensional materials from high-throughput computational exfoliation of experimentally known compounds. *Nature Nanotechnology*, 13(3), (2018) 246–252

[20] **Xu, M.**, **Liang, T.**, **Shi, M.**, **et al.** Graphene-like two-dimensional materials. *Chemical Reviews*, 113(5), (2013) 3766–3798

[21] **Gorbachev, R.V.**, **Riaz, I.**, **Nair, R.R.**, **et al.** Hunting for monolayer boron nitride: Optical and raman signatures. *Small*, 7(4), (2011) 465–468

[22] **Li, L.H.**, **Cervenka, J.**, **Watanabe, K.**, **et al.** Strong oxidation resistance of atomically thin boron nitride nanosheets. *ACS Nano*, 8(2), (2014) 1457–1462

[23] **Ares, P.**, **Cea, T.**, **Holwill, M.**, **et al.** Piezoelectricity in monolayer hexagonal boron nitride. *Advanced Materials*, 32(1)

[24] **Bertolazzi, S.**, **Brivio, J.**, & **Kis, A.** Stretching and breaking of ultrathin mos 2. *ACS Nano*, 5(12), (2011) 9703–9709

[25] **Fuhrer, M.S.** & **Hone, J.** Measurement of mobility in dual-gated mos2 transistors. *Nature Nanotechnology*, 8(3), (2013) 146–147

[26] **Ares, P.** & **Novoselov, K.S.** Recent advances in graphene and other 2d materials. *Nano Materials Science*, 4(1), (2022) 3–9

[27] **Wang, H.**, **Yu, L.**, **Lee, Y.H.**, **et al.** Integrated circuits based on bilayer mos 2 transistors. *Nano Letters*, 12(9), (2012) 4674–4680

[28] **Lin, Y.M.**, **Dimitrakopoulos, C.**, **Jenkins, K.A.**, **et al.** 100-ghz transistors from wafer-scale epitaxial graphene. *Science*, 327(5966), (2010) 662

[29] **Radisavljevic, B.**, **Radenovic, A.**, **Brivio, J.**, **et al.** Single-layer mos2 transistors. *Nature Nanotechnology*, 6(3), (2011) 147–150

[30] **Xia, F.**, **Mueller, T.**, **Lin, Y.M.**, **et al.** Ultrafast graphene photodetector. *Nature Nanotechnology*, 4(12), (2009) 839–843

[31] **Liu, M.**, **Yin, X.**, **Ulin-Avila, E.**, **et al.** A graphene-based broadband optical modulator. *Nature*, 474(7349), (2011) 64–67

[32] **Kuila, T.**, **Bose, S.**, **Khanra, P.**, **et al.** Recent advances in graphene-based biosensors. *Biosensors and Bioelectronics*, 26(12), (2011) 4637–4648

[33] **Garaj, S.**, **Hubbard, W.**, **Reina, A.**, **et al.** Graphene as a subnanometre trans-electrode membrane. *Nature*, 467(7312), (2010) 190–193

[34] **Novoselov, K.S.** & **Castro Neto, A.H.** Two-dimensional crystals-based heterostructures: Materials with tailored properties. *Physica Scripta*, (T146)

[35] **Guo, H.W.**, **Hu, Z.**, **Liu, Z.B.**, **et al.** Stacking of 2d materials. *Advanced Functional Materials*, 31(4), (2021) 2007810

[36] **Cao, Y.**, **Fatemi, V.**, **Fang, S.**, **et al.** Unconventional superconductivity in magic-angle graphene superlattices. *Nature*, 556(7699), (2018) 43–50

[37] **Dean, C.R.**, **Young, A.F.**, **Meric, I.**, **et al.** Boron nitride substrates for high-quality graphene electronics. *Nature Nanotechnology*, 5(10), (2010) 722–726

[38] **Mayorov, A.S.**, **Gorbachev, R.V.**, **Morozov, S.V.**, **et al.** Micrometer-scale ballistic transport in encapsulated graphene at room temperature. *Nano Letters*, 11(6), (2011) 2396–2399

[39] **Kretinin, A.V.**, **Cao, Y.**, **Tu, J.S.**, **et al.** Electronic properties of graphene encapsulated with different two-dimensional atomic crystals. *Nano Letters*, 14(6), (2014) 3270–3276

[40] **Wang, L.**, **Meric, I.**, **Huang, P.Y.**, **et al.** One-dimensional electrical contact to a two-dimensional material. *Science*, 342(6158), (2013) 614–617

[41] **Roy, N.K.**, **Behera, D.**, **Dibua, O.G.**, **et al.** A novel microscale selective laser sintering (μ-sls) process for the fabrication of microelectronic parts. *Microsystems and Nanoengineering*, 5(1), (2019) 64

[42] **Faraji Rad, Z.**, **Prewett, P.D.**, & **Davies, G.J.** High-resolution two-photon polymerization: the most versatile technique for the fabrication of microneedle arrays. *Microsystems and Nanoengineering*, 7(1), (2021) 71

[43] **Susi, T.**, **Meyer, J.C.**, & **Kotakoski, J.** Manipulating low-dimensional materials down to the level of single atoms with electron irradiation. *Ultramicroscopy*, 180, (2017) 163–172

[44] **Tripathi, M.**, **Mittelberger, A.**, **Pike, N.A.**, **et al.** Electron-beam manipulation of silicon dopants in graphene. *Nano Letters*, 18(8), (2018) 5319–5323

[45] **Dyck, O.**, **Kim, S.**, **Kalinin, S.V.**, **et al.** Placing single atoms in graphene with a scanning transmission electron microscope. *Applied Physics Letters*, 111(11)

[46] **Liu, X.**, **Xu, T.**, **Wu, X.**, **et al.** Top-down fabrication of sub-nanometre semiconducting nanoribbons derived from molybdenum disulfide sheets. *Nature Communications*, 4

[47] **Masih Das, P.**, **Danda, G.**, **Cupo, A.**, **et al.** Controlled sculpture of black phosphorus nanoribbons. *ACS Nano*, 10(6), (2016) 5687–5695

[48] **Chen, J.**, **Ryu, G.H.**, **Zhang, Q.**, **et al.** Spatially controlled fabrication and mechanisms of atomically thin nanowell patterns in bilayer ws2 using in situ high temperature electron microscopy. *ACS Nano*, 13(12), (2019) 14486–14499

[49] **Zsigmondy, R.** Die keimmethode zur herstellung kolloider metallösungen bestimmter eigenschaften. *Zeitschrift für anorganische und allgemeine Chemie*, 99(1), (1917) 105–117

[50] **Sharma, V.**, **Park, K.**, & **Srinivasarao, M.** Colloidal dispersion of gold nanorods: Historical background, optical properties, seed-mediated synthesis, shape separation and self-assembly. *Materials Science and Engineering: R: Reports*, 65(1-3), (2009) 1–38

[51] **James Singh, K.**, **Ahmed, T.**, **Gautam, P.**, **et al.** Recent advances in two-dimensional quantum dots and their applications. *Nanomaterials*, 11(6), (2021) 1549

[52] **Geim, A.K.** & **Novoselov, K.S.** The rise of graphene. *Nature Materials*, 6(3), (2007) 183–191

[53] **Mas-Ballesté, R.**, **Gómez-Navarro, C.**, **Gómez-Herrero, J.**, **et al.** 2d materials: To graphene and beyond. *Nanoscale*, 3(1), (2011) 20–30

[54] **Du, X.**, **Skachko, I.**, **Barker, A.**, **et al.** Approaching ballistic transport in suspended graphene. *Nature Nanotechnology*, 3(8), (2008) 491–495

[55] **Lee, C.**, **Wei, X.**, **Kysar, J.W.**, **et al.** Measurement of the elastic properties and intrinsic strength of monolayer graphene. *Science*, 321(5887), (2008) 385–388

[56] **Lau, C.N.**, **Bao, W.**, & **Velasco, J.** Properties of suspended graphene membranes. *Materials Today*, 15(6), (2012) 238–245

[57] **Roldán, R.**, **Chirolli, L.**, **Prada, E.**, **et al.** Theory of 2d crystals: Graphene and beyond. *Chemical Society Reviews*, 46(15), (2017) 4387–4399

[58] **Xia, F.**, **Wang, H.**, **Xiao, D.**, **et al.** Two-dimensional material nanophotonics. *Nature Photonics*, 8(12), (2014) 899–907

[59] **University of Vienna**. Sounds of matter. `https://sounds-of-matter.univie.ac.at/research-projects/2d-materials/`, Accessed: 2024-01-22

[60] **Woods, C.R.**, **Britnell, L.**, **Eckmann, A.**, **et al.** Commensurate-incommensurate transition in graphene on hexagonal boron nitride. *Nature Physics*, 10(6), (2014) 451–456

[61] **Knobloch, T.**, **Illarionov, Y.Y.**, **Ducry, F.**, **et al.** The performance limits of hexagonal boron nitride as an insulator for scaled cmos devices based on two-dimensional materials. *Nature Electronics*, 4(2), (2021) 98–108

[62] **Zhao, Y.** & **Ouyang, G.** Thickness-dependent photoelectric properties of mos2/si heterostructure solar cells. *Scientific Reports*, 9(1), (2019) 17381

[63] **Xi, X.**, **Wang, Z.**, **Zhao, W.**, **et al.** Ising pairing in superconducting nbse2 atomic layers. *Nature Physics*, 12(2), (2016) 139–143

[64] **Shi, Y.**, **Li, H.**, & **Li, L.J.** Recent advances in controlled synthesis of two-dimensional transition metal dichalcogenides via vapour deposition techniques. *Chemical Society Reviews*, 44(9), (2015) 2744–2756

[65] **Manzeli, S.**, **Ovchinnikov, D.**, **Pasquier, D.**, **et al.** 2d transition metal dichalcogenides. *Nature Reviews Materials*, 2(8), (2017) 17033

[66] **Peimyoo, N.**, **Shang, J.**, **Cong, C.**, **et al.** Nonblinking, intense two-dimensional light emitter: Monolayer ws 2 triangles. *ACS Nano*, 7(12), (2013) 10985–10994

[67] **Gusakova, J.**, **Wang, X.**, **Shiau, L.L.**, **et al.** Electronic properties of bulk and monolayer tmds: Theoretical study within dft framework (gvj-2e method). *Physica Status Solidi (A) Applications and Materials Science*, 214(12)

[68] **Yang, X.** & **Li, B.** Monolayer mos 2 for nanoscale photonics. *Nanophotonics*, 9(7), (2020) 1557–1577

[69] **Cadiz, F.**, **Courtade, E.**, **Robert, C.**, **et al.** Excitonic linewidth approaching the homogeneous limit in mos2-based van der waals heterostructures. *Physical Review X*, 7(2)

[70] **Zhou, M.**, **Wang, W.**, **Lu, J.**, **et al.** How defects influence the photoluminescence of tmdcs. *Nano Research*, 14(1), (2021) 29–39

[71] **Zhang, X.**, **Nan, H.**, **Xiao, S.**, **et al.** Transition metal dichalcogenides bilayer single crystals by reverse-flow chemical vapor epitaxy. *Nature Communications*, 10(1), (2019) 598

[72] **Ando, T.** Screening effect and impurity scattering in monolayer graphene. *Journal of the Physical Society of Japan*, 75(7)

[73] **Fratini, S.** & **Guinea, F.** Substrate-limited electron dynamics in graphene. *Physical Review B - Condensed Matter and Materials Physics*, 77(19)

[74] **Chen, J.H.**, **Jang, C.**, **Xiao, S.**, **et al.** Intrinsic and extrinsic performance limits of graphene devices on sio 2. *Nature Nanotechnology*, 3(4), (2008) 206–209

[75] **Bolotin, K.I.**, **Sikes, K.J.**, **Hone, J.**, **et al.** Temperature-dependent transport in suspended graphene. *Physical Review Letters*, 101(9)

[76] **Dean, C.**, **Young, A.F.**, **Wang, L.**, **et al.** Graphene based heterostructures. *Solid State Communications*, 152(15), (2012) 1275–1282

[77] **Novoselov, K.S.**, **Mishchenko, A.**, **Carvalho, A.**, **et al.** 2d materials and van der waals heterostructures. *Science*, 353(6298)

[78] **Liu, Y.**, **Weiss, N.O.**, **Duan, X.**, **et al.** Van der waals heterostructures and devices. *Nature Reviews Materials*, 1(9), (2016) 16042

[79] **Liu, L.**, **Liu, C.**, **Jiang, L.**, **et al.** Ultrafast non-volatile flash memory based on van der waals heterostructures. *Nature Nanotechnology*, 16(8), (2021) 874–881

[80] **Frisenda, R.**, **Navarro-Moratalla, E.**, **Gant, P.**, **et al.** Recent progress in the assembly of nanodevices and van der waals heterostructures by deterministic placement of 2d materials. *Chemical Society Reviews*, 47(1), (2018) 53–68

[81] **Zan, R.**, **Ramasse, Q.M.**, **Jalil, R.**, **et al.** Control of radiation damage in mos2 by graphene encapsulation. *ACS Nano*, 7(11), (2013) 10167–10174

[82] **Hunt, B.**, **Sanchez-Yamagishi, J.D.**, **Young, A.F.**, **et al.** Massive dirac fermions and hofstadter butterfly in a van der waals heterostructure. *Science*, 340(6139), (2013) 1427–1430

[83] **Terrones, H.**, **López-Urías, F.**, & **Terrones, M.** Novel hetero-layered materials with tunable direct band gaps by sandwiching different metal disulfides and diselenides. *Scientific Reports*, 3(1), (2013) 1549

[84] **Cao, Y.**, **Fatemi, V.**, **Demir, A.**, **et al.** Correlated insulator behaviour at half-filling in magic-angle graphene superlattices. *Nature*, 556(7699), (2018) 80–84

[85] **Yankowitz, M.**, **Chen, S.**, **Polshyn, H.**, **et al.** Tuning superconductivity in twisted bilayer graphene. *Science*, 363(6431), (2019) 1059–1064

[86] **Tien, D.H.**, **Park, J.Y.**, **Kim, K.B.**, **et al.** Characterization of graphene-based fet fabricated using a shadow mask. *Scientific Reports*, 6

[87] **Zomer, P.J.**, **Dash, S.P.**, **Tombros, N.**, **et al.** A transfer technique for high mobility graphene devices on commercially available hexagonal boron nitride. *Applied Physics Letters*, 99(23)

[88] **Schneider, G.F.**, **Calado, V.E.**, **Zandbergen, H.**, **et al.** Wedging transfer of nanostructures. *Nano Letters*, 10(5), (2010) 1912–1916

[89] **Castellanos-Gomez, A.**, **Buscema, M.**, **Molenaar, R.**, **et al.** Deterministic transfer of two-dimensional materials by all-dry viscoelastic stamping. *2D Materials*, 1(1)

[90] **Ponomarenko, L.A.**, **Gorbachev, R.V.**, **Yu, G.L.**, **et al.** Cloning of dirac fermions in graphene superlattices. *Nature*, 497(7451), (2013) 594–597

[91] **Wang, S.**, **Cui, X.**, **Jian, C.**, **et al.** Stacking-engineered heterostructures in transition metal dichalcogenides. *Advanced Materials*, 33(16), (2021) 2005735

[92] **Kim, K.**, **Yankowitz, M.**, **Fallahazad, B.**, **et al.** Van der waals heterostructures with high accuracy rotational alignment. *Nano Letters*, 16(3), (2016) 1989–1995

[93] **Wang, S.**, **Wang, X.**, & **Warner, J.H.** All chemical vapor deposition growth of MoS2:h-

BN vertical van der Waals heterostructures. *ACS Nano*, 9(5), (2015) 5246–5254

[94] **Gannett, W.**, **Regan, W.**, **Watanabe, K.**, **et al.** Boron nitride substrates for high mobility chemical vapor deposited graphene. *Applied Physics Letters*, 98(24)

[95] **Gong, Y.**, **Lin, J.**, **Wang, X.**, **et al.** Vertical and in-plane heterostructures from ws 2 /mos 2 monolayers. *Nature Materials*, 13(12), (2014) 1135–1142

[96] **Zhang, C.**, **Zhao, S.**, **Jin, C.**, **et al.** Direct growth of large-area graphene and boron nitride heterostructures by a co-segregation method. *Nature Communications*, 6

[97] **Alahmadi, M.**, **Mahvash, F.**, **Szkopek, T.**, **et al.** A two-step chemical vapor deposition process for the growth of continuous vertical heterostructure wse2/h-bn and its optical properties. *RSC Advances*, 11(28), (2021) 16962–16969

[98] **Ai, R.**, **Guan, X.**, **Li, J.**, **et al.** Growth of single-crystalline cadmium iodide nanoplates, cdi2/mos2 (ws2, wse2) van der waals heterostructures, and patterned arrays. *ACS Nano*, 11(3), (2017) 3413–3419

[99] **Li, J.**, **Yang, X.**, **Liu, Y.**, **et al.** General synthesis of two-dimensional van der waals heterostructure arrays. *Nature*, 579(7799), (2020) 368–374

[100] **Dumcenco, D.**, **Ovchinnikov, D.**, **Marinov, K.**, **et al.** Large-area epitaxial monolayer mos2. *ACS Nano*, 9(4), (2015) 4611–4620

[101] **Sun, L.**, **Wang, Z.**, **Wang, Y.**, **et al.** Hetero-site nucleation for growing twisted bilayer graphene with a wide range of twist angles. *Nature Communications*, 12(1)

[102] **Pedersen, T.G.** Exciton stark shift and electroabsorption in monolayer transition-metal dichalcogenides. *Physical Review B*, 94(12), (2016) 125424

[103] **Liu, F.**, **Zhou, J.**, **Zhu, C.**, **et al.** Electric field effect in two-dimensional transition metal dichalcogenides. *Advanced Functional Materials*, 27(19)

[104] **Yutomo, E.B.**, **Noor, F.A.**, & **Winata, T.** Effect of the number of nitrogen dopants on the electronic and magnetic properties of graphitic and pyridinic n-doped graphene-a density-functional study. *RSC Advances*, 11(30), (2021) 18371–18380

[105] **Nigge, P.**, **Qu, A.C.**, **Lantagne-Hurtubise**, **et al.** Room temperature strain-induced landau levels in graphene on a wafer-scale platform. *Science Advances*, 5(11), (2019) 1–7

[106] **Peng, Z.**, **Chen, X.**, **Fan, Y.**, **et al.** Strain engineering of 2d semiconductors and graphene: from strain fields to band-structure tuning and photonic applications. *Light: Science and Applications*, 9(1), (2020) 190

[107] **Pedersen, T.G.**, **Flindt, C.**, **Pedersen, J.**, **et al.** Graphene antidot lattices: Designed defects and spin qubits. *Physical Review Letters*, 100(13), (2008) 136804

[108] **Barone, V.**, **Hod, O.**, & **Scuseria, G.E.** Electronic structure and stability of semiconducting graphene nanoribbons. *Nano Letters*, 6(12), (2006) 2748–2754

[109] **Jessen, B.S.**, **Gammelgaard, L.**, **Thomsen, M.R.**, **et al.** Lithographic band structure engineering of graphene. *Nature Nanotechnology*, 14(4), (2019) 340–346

[110] **Bai, J.**, **Zhong, X.**, **Jiang, S.**, **et al.** Graphene nanomesh. *Nature Nanotechnology*, 5(3), (2010) 190–194

[111] **Kim, M.**, **Safron, N.S.**, **Han, E.**, **et al.** Fabrication and characterization of large-area, semiconducting nanoperforated graphene materials. *Nano Letters*, 10(4), (2010) 1125–1131

[112] **Kim, Y.H.**, **Kim, S.J.**, **Kim, Y.J.**, **et al.** Self-activated transparent all-graphene gas sensor with endurance to humidity and mechanical bending. *ACS Nano*, 9(10), (2015) 10453–10460

[113] **Shao, L.**, **Chen, G.**, **Ye, H.**, **et al.** Theoretical study on electronic properties of mos2 antidot lattices. *Journal of Applied Physics*, 116(11)

[114] **Stanev, T.K.**, **Liu, P.**, **Zeng, H.**, **et al.** Direct patterning of optoelectronic nanostructures using encapsulated layered transition metal dichalcogenides. *ACS Applied Materials and Interfaces*, 14(20), (2022) 23775–23784

[115] **Chowdhury, T.**, **Kim, J.**, **Sadler, E.C.**, **et al.** Substrate-directed synthesis of mos2 nanocrystals with tunable dimensionality and optical properties. *Nature Nanotechnology*, 15(1), (2020) 29–34

[116] **Munkhbat, B.**, **Küçüköz, B.**, **Baranov, D.G.**, **et al.** Nanostructured transition metal dichalcogenide multilayers for advanced nanophotonics. *Laser and Photonics Reviews*, 17(1), (2023) 1–11

[117] **Löchner, F.J.F.**, **Mupparapu, R.**, **Steinert, M.**, **et al.** Controlling second-harmonic diffraction by nano-patterning MoS2 monolayers. *Optics Express*, 27(24), (2019) 35475

[118] **Alexeev, E.M.**, **Ruiz-Tijerina, D.A.**, **Danovich, M.**, **et al.** Resonantly hybridized excitons in moiré superlattices in van der waals heterostructures. *Nature*, 567(7746), (2019) 81–86

[119] **Dean, C.R.**, **Wang, L.**, **Maher, P.**, **et al.** Hofstadter's butterfly and the fractal quantum hall effect in moiré superlattices. *Nature*, 497(7451), (2013) 598–602

[120] **Liu, Y.**, **Wu, H.**, **Cheng, H.C.**, **et al.** Toward barrier free contact to molybdenum disulfide using graphene electrodes. *Nano Letters*, 15(5), (2015) 3030–3034

[121] **Yu, L.**, **Lee, Y.H.**, **Ling, X.**, **et al.** Graphene/mos2 hybrid technology for large-scale two-dimensional electronics. *Nano Letters*, 14(6), (2014) 3055–3063

[122] **Cui, X.**, **Lee, G.H.**, **Kim, Y.D.**, **et al.** Multi-terminal transport measurements of mos2 using a van der waals heterostructure device platform. *Nature Nanotechnology*, 10(6), (2015) 534–540

[123] **Furchi, M.M.**, **Zechmeister, A.A.**, **Hoeller, F.**, **et al.** Photovoltaics in van der waals heterostructures. *IEEE Journal of Selected Topics in Quantum Electronics*, 23(1), (2017) 106–116

[124] **Massicotte, M.**, **Schmidt, P.**, **Vialla, F.**, **et al.** Picosecond photoresponse in van der waals heterostructures. *Nature Nanotechnology*, 11(1), (2016) 42–46

[125] **Davidson, M.W.** Pioneers in optics: Zacharias janssen and johannes kepler. *Microscopy Today*, 17(6), (2009) 44–47

[126] **Huang, B.** Super-resolution optical microscopy: multiple choices. *Current Opinion in Chemical Biology*, 14(1), (2010) 10–14

[127] **de Broglie, L.** Xxxv. a tentative theory of light quanta. *The London, Edinburgh, and Dublin Philosophical Magazine and Journal of Science*, 47(278), (1924) 446–458

[128] **Busch, H.** Über die wirkungsweise der konzentrierungsspule bei der braunschen röhre. *Archiv für Elektrotechnik*, 18(6), (1927) 583–594

[129] **Van Gorkomm, J.** The early electron microscopes: A critical study. *Advances in Imaging*

and Electron Physics, 205, (2018) 1–137

[130] **Knoll, M.** & **Ruska, E.** Das elektronenmikroskop. *Zeitschrift für Physik*, 78(5-6), (1932) 318–339

[131] **Ruska, E.** Das elektronenmikroskop als Übermikroskop. *Forschungen und Fortschritte*, 10(1), (1934) 8

[132] **Fitzgerald, R.**, **Keil, K.**, & **Heinrich, K.F.** Solid-state energy-dispersion spectrometer for electron-microprobe x-ray analysis. *Science*, 159(814), (1968) 528–530

[133] **Krivanek, O.L.** & **Swann, P.R.** An advanced electron energy loss spectrometer. *Quantitative microanalysis with high spatial resolution*, pages 136–140

[134] **Cosslett, V.E.**, **Camps, R.A.**, **Saxton, W.O.**, **et al.** Atomic resolution with a 600-kv electron microscope [3]. *Nature*, 281(5726), (1979) 49–51

[135] **Hirabayashi, M.**, **Hiraga, K.**, & **Shindo, D.** High resolution imaging by 1 mv electron microscopy. *Ultramicroscopy*, 9(3), (1982) 197–202

[136] **Phillipp, F.**, **Höschen, R.**, **Osaki, M.**, **et al.** New high-voltage atomic resolution microscope approaching 1 åpoint resolution installed in stuttgart. *Ultramicroscopy*, 56(1-3), (1994) 1–10

[137] **O'Keefe, M.A.**, **Hetherington, C.J.**, **Wang, Y.C.**, **et al.** Sub-angstrom high-resolution transmission electron microscopy at 300kev. *Ultramicroscopy*, 89(4), (2001) 215–241

[138] **Scherzer, O.** Über einige fehler von elektronenlinsen. *Zeitschrift für Physik*, 101(9-10), (1936) 593–603

[139] **Scherzer, O.** The theoretical resolution limit of the electron microscope. *Journal of Applied Physics*, 20(1), (1949) 20–29

[140] **Rose, H.** Correction of aberrations, a promising means for improving the spatial and energy resolution of energy-filtering electron microscopes. *Ultramicroscopy*, 56(1-3), (1994) 11–25

[141] **Haider, M.**, **Rose, H.**, **Uhlemann, S.**, **et al.** A spherical-aberration-corrected 200 kv transmission electron microscope. *Ultramicroscopy*, 75(1), (1998) 53–60

[142] **Krivanek, O.L.**, **Dellby, N.**, & **Lupini, A.R.** Towards sub-åelectron beams. *Ultramicroscopy*, 78(1-4), (1999) 1–11

[143] **Williams, D.B.** & **Carter, C.B.** *Transmission electron microscopy: A textbook for materials science.* Springer US, Boston, MA (2009)

[144] **Reimer, L.** *Transmission Electron Microscopy: Physics of Image Formation and Microanalysis (Springer Series in Optical Sciences,)*, volume 36 of *Springer Series in Optical Sciences.* Springer New York, New York, NY (1997)

[145] **Central Microscopy Research Facility, University of Iowa**. Transmission electron microscopy. `https://cmrf.research.uiowa.edu/transmission-electron-microscopy`, Accessed: 2024-04-17

[146] **Thomas, J.** & **Gemming, T.** *Analytical transmission electron microscopy: An introduction for operators.* Springer Netherlands, Dordrecht (2014)

[147] **Lee, Z.**, **Lehnert, T.**, **Kaiser, U.**, **et al.** Comparison of different imaging models

handling partial coherence for aberration-corrected hrtem at 40–80 kv. *Ultramicroscopy*, 203(February), (2019) 68–75

[148] **von Ardenne, M.** Das elektronen-rastermikroskop - theoretische grundlagen. *Zeitschrift für Physik*, 109(9-10), (1938) 553–572

[149] **Verbeeck, J.**, **Béché, A.**, **Müller-Caspary, K.**, **et al.** Demonstration of a 2x2 programmable phase plate for electrons. *Ultramicroscopy*, 190, (2018) 58–65

[150] **Danev, R.** & **Nagayama, K.** Transmission electron microscopy with zernike phase plate. *Ultramicroscopy*, 88(4), (2001) 243–252

[151] **Malac, M.**, **Hettler, S.**, **Hayashida, M.**, **et al.** Phase plates in the transmission electron microscope: operating principles and applications. *Microscopy*, 70(1), (2021) 75–115

[152] **Danev, R.** & **Nagayama, K.** Optimizing the phase shift and the cut-on periodicity of phase plates for tem. *Ultramicroscopy*, 111(8), (2011) 1305–1315

[153] **Kishchenko, G.P.**, **Danev, R.**, **Fisher, R.**, **et al.** Effect of fringe-artifact correction on sub-tomogram averaging from zernike phase-plate cryo-tem. *Journal of Structural Biology*, 191(3), (2015) 299–305

[154] **Marko, M.**, **Leith, A.D.**, **Hsieh, C.**, **et al.** Retrofit implementation of zernike phase plate imaging for cryo-tem. *Journal of Structural Biology*, 174(2), (2011) 400–412

[155] **Schultheiß, K.**, **Párez-Willard, F.**, **Barton, B.**, **et al.** Fabrication of a boersch phase plate for phase contrast imaging in a transmission electron microscope. *Review of Scientific Instruments*, 77(3), (2006) 033701

[156] **Hell, S.W.** & **Wichmann, J.** Breaking the diffraction resolution limit by stimulated emission: stimulated-emission-depletion fluorescence microscopy. *Optics Letters*, 19(11), (1994) 780

[157] **Lichte, H.** & **Lehmann, M.** Electron holography - basics and applications. *Reports on Progress in Physics*, 71(1), (2008) 016102

[158] **Poon, T.C.** & **Liu, J.P.** *Introduction to Modern Digital Holography*, pages 59–78. Cambridge University Press, Cambridge (2014)

[159] **Shiloh, R.**, **Lereah, Y.**, **Lilach, Y.**, **et al.** Sculpturing the electron wave function using nanoscale phase masks. *Ultramicroscopy*, 144, (2014) 26–31

[160] **Pohl, D.**, **Schneider, S.**, **Zeiger, P.**, **et al.** Atom size electron vortex beams with selectable orbital angular momentum. *Scientific Reports*, 7(1)

[161] **Padgett, M.**, **Courtial, J.**, & **Allen, L.** Light's orbital angular momentum. *Physics Today*, 57(5), (2004) 35–40

[162] **Zhong, X.**, **Lin, J.**, **Kao, S.**, **et al.** Atomistic defect makes a phase plate for the generation and high-angular splitting of electron vortex beams. *ACS Nano*, 13(4), (2019) 3964–3970

[163] **Verbeeck, J.**, **Tian, H.**, & **Schattschneider, P.** Production and application of electron vortex beams. *Nature*, 467(7313), (2010) 301–304

[164] **McMorran, B.J.**, **Agrawal, A.**, **Anderson, I.M.**, **et al.** Electron vortex beams with high quanta of orbital angular momentum. *Science*, 331(6014), (2011) 192–195

[165] **McMorran, B.J.**, **Agrawal, A.**, **Ercius, P.A.**, **et al.** Origins and demonstrations of

electrons with orbital angular momentum. *Philosophical Transactions of the Royal Society A: Mathematical, Physical and Engineering Sciences*, 375(2087)

[166] **Verbeeck, J.**, **Tian, H.**, & **Béché, A.** A new way of producing electron vortex probes for stem. *Ultramicroscopy*, 113, (2012) 83–87

[167] **Uchida, M.** & **Tonomura, A.** Generation of electron beams carrying orbital angular momentum. *Nature*, 464(7289), (2010) 737–739

[168] **Tavabi, A.H.**, **Rosi, P.**, **Rotunno, E.**, **et al.** Experimental demonstration of an electrostatic orbital angular momentum sorter for electron beams. *Physical Review Letters*, 126(9)

[169] **Grillo, V.**, **Harvey, T.R.**, **Venturi, F.**, **et al.** Observation of nanoscale magnetic fields using twisted electron beams. *Nature Communications*, 8(1), (2017) 8–13

[170] **Pohl, D.**, **Schneider, S.**, **Rusz, J.**, **et al.** Electron vortex beams prepared by a spiral aperture with the goal to measure emcd on ferromagnetic films via stem. *Ultramicroscopy*, 150, (2015) 16–22

[171] **Thirunavukkarasu, G.**, **G Thirunavukkarasu, J.Y.**, & **Babiker, M.** Observation of gold nanoparticles movements under sub-10 nm vortex electron beams in an aberration corrected tem. In **D.J. Stokes** & **J. Hutchison**, editors, *Royal Microscopical Society* (2012)

[172] **Verbeeck, J.**, **Tian, H.**, & **Van Tendeloo, G.** How to manipulate nanoparticles with an electron beam? *Advanced Materials*, 25(8), (2013) 1114–1117

[173] **Liu, M.**, **Xu, L.**, & **Lin, X.** Heating effect of electron beam bombardment. *Scanning*, 16(1), (1994) 1–5

[174] **Bouscaud, D.**, **Pesci, R.**, **Berveiller, S.**, **et al.** Estimation of the electron beam-induced specimen heating and the emitted x-rays spatial resolution by kossel microdiffraction in a scanning electron microscope. *Ultramicroscopy*, 115, (2012) 115–119

[175] **Egerton, R.F.**, **Li, P.**, & **Malac, M.** Radiation damage in the tem and sem. *Micron*, 35(6), (2004) 399–409

[176] **McCartney, M.**, **Crozier, P.**, **Weiss, J.**, **et al.** Electron-beam-induced reactions at transition-metal oxide surfaces. *Vacuum*, 42(4), (1991) 301–308

[177] **Egerton, R.F.** Control of radiation damage in the tem. *Ultramicroscopy*, 127, (2013) 100–108

[178] **Hugenschmidt, M.**, **Adrion, K.**, **Marx, A.**, **et al.** Electron-beam-induced carbon contamination in stem-in-sem: Quantification and mitigation. *Microscopy and Microanalysis*, 29(1), (2023) 219–234

[179] **Zobelli, A.**, **Gloter, A.**, **Ewels, C.P.**, **et al.** Electron knock-on cross section of carbon and boron nitride nanotubes. *Physical Review B - Condensed Matter and Materials Physics*, 75(24)

[180] **Meyer, J.C.**, **Eder, F.**, **Kurasch, S.**, **et al.** Accurate measurement of electron beam induced displacement cross sections for single-layer graphene. *Physical Review Letters*, 108(19)

[181] **McKenna, A.J.**, **Trevethan, T.**, **Latham, C.D.**, **et al.** Threshold displacement energy and damage function in graphite from molecular dynamics. *Carbon*, 99, (2016) 71–78

[182] **Mott, N.** The scattering of fast electrons by atomic nuclei. *Proceedings of the Royal Society of London. Series A, Containing Papers of a Mathematical and Physical Character*, 124(794), (1929) 425–442

[183] **McKinley, W.A.** & **Feshbach, H.** The coulomb scattering of relativistic electrons by nuclei. *Physical Review*, 74(12), (1948) 1759–1763

[184] **Meyer, J.C.**, **Eder, F.**, **Kurasch, S.**, **et al.** Erratum: Accurate measurement of electron beam induced displacement cross sections for single-layer graphene. *Physical Review Letters*, 110(23)

[185] **Komsa, H.P.**, **Kotakoski, J.**, **Kurasch, S.**, **et al.** Two-dimensional transition metal dichalcogenides under electron irradiation: Defect production and doping. *Physical Review Letters*, 109(3), (2012) 035503

[186] **Lin, J.**, **Zhang, Y.**, **Zhou, W.**, **et al.** Structural flexibility and alloying in ultrathin transition-metal chalcogenide nanowires. *ACS Nano*, 10(2), (2016) 2782–2790

[187] **Kalinin, S.V.**, **Borisevich, A.**, & **Jesse, S.** Fire up the atom forge. *Nature*, 539(7630), (2016) 485–487

[188] **Liddle, J.A.**, **Gallatin, G.M.**, & **Ocola, L.E.** Resist requirements and limitations for nanoscale electron-beam patterning. *Materials Research Society Symposium - Proceedings*, 739, (2002) 19–30

[189] **Meyer, J.C.**, **Girit, C.O.**, **Crommie, M.F.**, **et al.** Hydrocarbon lithography on graphene membranes. *Applied Physics Letters*, 92(12)

[190] **Van Dorp, W.F.**, **Van Someren, B.**, **Hagen, C.W.**, **et al.** Approaching the resolution limit of nanometer-scale electron beam-induced deposition. *Nano Letters*, 5(7), (2005) 1303–1307

[191] **Plank, H.**, **Winkler, R.**, **Schwalb, C.H.**, **et al.** Focused electron beam-based 3d nanoprinting for scanning probe microscopy: A review. *Micromachines*, 11(1), (2019) 48

[192] **Utke, I.**, **Hoffmann, P.**, & **Melngailis, J.** Gas-assisted focused electron beam and ion beam processing and fabrication. *Journal of Vacuum Science & Technology B: Microelectronics and Nanometer Structures Processing, Measurement, and Phenomena*, 26(4), (2008) 1197–1276

[193] **Spinney, P.S.**, **Howitt, D.G.**, **Collins, S.D.**, **et al.** Electron beam stimulated oxidation of carbon. *Nanotechnology*, 20(46)

[194] **Coburn, J.W.** & **Winters, H.F.** Ion- and electron-assisted gas-surface chemistry - an important effect in plasma etching. *Journal of Applied Physics*, 50(5), (1979) 3189–3196

[195] **Urbanos, F.J.**, **Black, A.**, **Bernardo-Gavito, R.**, **et al.** Electrical and geometrical tuning of mos2 field effect transistors: Via direct nanopatterning. *Nanoscale*, 11(23), (2019) 11152–11158

[196] **Fischbein, M.D.** & **Drndić, M.** Electron beam nanosculpting of suspended graphene sheets. *Applied Physics Letters*, 93(11)

[197] **Song, B.**, **Schneider, G.F.**, **Xu, Q.**, **et al.** Atomic-scale electron-beam sculpting of near-defect-free graphene nanostructures. *Nano Letters*, 11(6), (2011) 2247–2250

[198] **Liu, K.**, **Feng, J.**, **Kis, A.**, **et al.** Atomically thin molybdenum disulfide nanopores with high sensitivity for dna translocation. *ACS Nano*, 8(3), (2014) 2504–2511

[199] **Graphenea**. Manufacturer homepage. `https://eu.graphenea.com/products/easy-transfer-monolayer-graphene-on-polymer-film-1-cm-x-1-cm`, Accessed: 2024-01-22

[200] **Haas, J.**, **Ulrich, F.**, **Hofer, C.**, **et al.** Aligned stacking of nanopatterned 2d materials for high-resolution 3d device fabrication. *ACS Nano*, 16(2), (2022) 1836–1846

[201] **Quantifoil**. Manufacturer homepage. `https://www.quantifoil.com/products/quantifoil`, Accessed: 2024-01-24

[202] **Haas, J.** Published stacking video. `https://pubs.acs.org/doi/suppl/10.1021/acsnano.1c09122/suppl_file/nn1c09122_si_002.avi`, Accessed: 2024-01-29

[203] **Kipp, L.**, **Skibowski, M.**, **Johnson, R.L.**, **et al.** Sharper images by focusing soft x-rays with photon sieves. *Nature*, 414(6860), (2001) 184–188

[204] **Andersen, G.** Large optical photon sieve. *Optics Letters*, 30(22), (2005) 2976

[205] **Shi, R.**, **Xu, H.**, **Chen, B.**, **et al.** Scalable fabrication of graphene devices through photolithography. *Applied Physics Letters*, 102(11)

[206] **Zhang, R.**, **Chen, T.**, **Bunting, A.**, **et al.** Optical lithography technique for the fabrication of devices from mechanically exfoliated two-dimensional materials. *Microelectronic Engineering*, 154, (2016) 62–68

[207] **Hwang, W.S.**, **Tahy, K.**, **Li, X.**, **et al.** Transport properties of graphene nanoribbon transistors on chemical-vapor-deposition grown wafer-scale graphene. *Applied Physics Letters*, 100(20)

[208] **Wei, T.**, **Hauke, F.**, & **Hirsch, A.** Evolution of graphene patterning: From dimension regulation to molecular engineering. *Advanced Materials*, 33(45)

[209] **Choi, J.**, **Zhang, H.**, **Du, H.**, **et al.** Understanding solvent effects on the properties of two-dimensional transition metal dichalcogenides. *ACS Applied Materials and Interfaces*, 8(14), (2016) 8864–8869

[210] **Wu, W.**, **Jauregui, L.A.**, **Su, Z.**, **et al.** Growth of single crystal graphene arrays by locally controlling nucleation on polycrystalline cu using chemical vapor deposition. *Advanced Materials*, 23(42), (2011) 4898–4903

[211] **Thissen, N.F.**, **Vervuurt, R.H.**, **Mackus, A.J.**, **et al.** Graphene devices with bottom-up contacts by area-selective atomic layer deposition. *2D Materials*, 4(2)

[212] **Zhang, W.**, **Li, L.**, **Wang, Z.B.**, **et al.** Ti:sapphire femtosecond laser direct micro-cutting and profiling of graphene. *Applied Physics A: Materials Science and Processing*, 109(2), (2012) 291–297

[213] **Ye, X.**, **Qi, M.**, **Yang, Y.**, **et al.** Pattern directive sensing selectivity of graphene for wearable multifunctional sensors via femtosecond laser fabrication. *Advanced Materials Technologies*, 5(11)

[214] **Huang, P.C.**, **Sun, H.**, **Sarker, M.**, **et al.** Sub-5 nm contacts and induced p-n junction formation in individual atomically precise graphene nanoribbons. *ACS Nano*, 17(18), (2023) 17771–17778

[215] **Thiele, C.**, **Felten, A.**, **Echtermeyer, T.J.**, **et al.** Electron-beam-induced direct etching of graphene. *Carbon*, 64, (2013) 84–91

[216] **Sommer, B.**, **Sonntag, J.**, **Ganczarczyk, A.**, **et al.** Electron-beam induced nano-

etching of suspended graphene. *Scientific Reports*, 5

[217] **Prével, B.**, **Benoit, J.M.**, **Bardotti, L.**, **et al.** Nanostructuring graphene on sic by focused ion beam: Effect of the ion fluence. *Applied Physics Letters*, 99(8)

[218] **Andersen, A.B.**, **Shivayogimath, A.**, **Booth, T.**, **et al.** Limiting damage to 2d materials during focused ion beam processing. *Physica Status Solidi (B) Basic Research*, 257(12)

[219] **Lemme, M.C.**, **Bell, D.C.**, **Williams, J.R.**, **et al.** Etching of graphene devices with a helium ion beam. *ACS Nano*, 3(9), (2009) 2674–2676

[220] **Buchheim, J.**, **Wyss, R.M.**, **Shorubalko, I.**, **et al.** Understanding the interaction between energetic ions and freestanding graphene towards practical 2d perforation. *Nanoscale*, 8(15), (2016) 8345–8354

[221] **Zhang, Y.**, **Hui, C.**, **Sun, R.**, **et al.** A large-area 15 nm graphene nanoribbon array patterned by a focused ion beam. *Nanotechnology*, 25(13), (2014) 135301

[222] **Liu, Y.**, **Qu, Y.**, **Liu, Y.**, **et al.** Direct-writing of 2d diodes by focused ion beams. *Advanced Functional Materials*, 31(34)

[223] **Lehtinen, O.**, **Kotakoski, J.**, **Krasheninnikov, A.V.**, **et al.** Cutting and controlled modification of graphene with ion beams. *Nanotechnology*, 22(17), (2011) 175306

[224] **Emmrich, D.**, **Beyer, A.**, **Nadzeyka, A.**, **et al.** Nanopore fabrication and characterization by helium ion microscopy. *Applied Physics Letters*, 108(16)

[225] **Batson, P.E.**, **Dellby, N.**, & **Krivanek, O.L.** Sub-angstrom resolution using aberration corrected electron optics. *Nature*, 418(6898), (2002) 617–620

[226] **Kirkland, E.J.** On the optimum probe in aberration corrected adf-stem. *Ultramicroscopy*, 111(11), (2011) 1523–1530

[227] **Wang, S.**, **Li, H.**, **Sawada, H.**, **et al.** Atomic structure and formation mechanism of sub-nanometer pores in 2d monolayer mos2. *Nanoscale*, 9(19), (2017) 6417–6426

[228] **Bui, T.A.**, **Leuthner, G.T.**, **Madsen, J.**, **et al.** Creation of single vacancies in hbn with electron irradiation. *Small*, 19(39)

[229] **Park, H.**, **Wen, Y.**, **Li, S.X.**, **et al.** Atomically precise control of carbon insertion into hbn monolayer point vacancies using a focused electron beam guide. *Small*, 17(23)

[230] **Hirsch, P.**, **Kässens, M.**, **Püttmann, M.**, **et al.** Contamination in a scanning electron microscope and the influence of specimen cooling. *Scanning*, 16(2), (1994) 101–110

[231] **Algara-Siller, G.**, **Lehtinen, O.**, **Turchanin, A.**, **et al.** Dry-cleaning of graphene. *Applied Physics Letters*, 104(15)

[232] **Xu, Q.**, **Wu, M.Y.**, **Schneider, G.F.**, **et al.** Controllable atomic scale patterning of freestanding monolayer graphene at elevated temperature. *ACS Nano*, 7(2), (2013) 1566–1572

[233] **Tripathi, M.**, **Mittelberger, A.**, **Mustonen, K.**, **et al.** Cleaning graphene: Comparing heat treatments in air and in vacuum. *Physica Status Solidi - Rapid Research Letters*, 11(8)

[234] **Schweizer, P.**, **Dolle, C.**, **Dasler, D.**, **et al.** Mechanical cleaning of graphene using in situ electron microscopy. *Nature Communications*, 11(1)

[235] **Métois, J.**, **Nitsche, S.**, & **Heyraud, J.** An ultra-high-vacuum transmission and scan-

ning electron microscope for crystal growth experiments. *Ultramicroscopy*, 27(4), (1989) 349–357

[236] **Tromp, R.M.** & **Ross, F.M.** Advances in in situ ultra-high vacuum electron microscopy: Growth of sige on si. *Annual Review of Materials Science*, 30(1), (2000) 431–449

[237] **Mangler, C.**, **Meyer, J.**, **Mittelberger, A.**, **et al.** A materials scientist's canvas: A system for controlled alteration of nanomaterials in vacuum down to the atomic scale. *Microscopy and Microanalysis*, 28(S1), (2022) 2940–2942

[238] **Reidy, K.**, **Thomsen, J.D.**, & **Ross, F.M.** Perspectives on ultra-high vacuum transmission electron microscopy of dynamic crystal growth phenomena. *Progress in Materials Science*, 139, (2023) 101163

[239] **Pastewka, L.**, **Salzer, R.**, **Graff, A.**, **et al.** Surface amorphization, sputter rate, and intrinsic stresses of silicon during low energy ga+ focused-ion beam milling. *Nuclear Instruments and Methods in Physics Research, Section B: Beam Interactions with Materials and Atoms*, 267(18), (2009) 3072–3075

[240] **Turner, E.M.**, **Sapkota, K.R.**, **Hatem, C.**, **et al.** Wet-chemical etching of fib lift-out tem lamellae for damage-free analysis of 3-d nanostructures. *Ultramicroscopy*, 216, (2020) 113049

[241] **Toth, M.** Advances in gas-mediated electron beam-induced etching and related material processing techniques. *Applied Physics A: Materials Science and Processing*, 117(4), (2014) 1623–1629

[242] **Son, J.**, **Kwon, J.**, **Kim, S.P.**, **et al.** Atomically precise graphene etch stops for three dimensional integrated systems from two dimensional material heterostructures. *Nature Communications*, 9(1)

[243] **Chow, P.K.**, **Jacobs-Gedrim, R.B.**, **Gao, J.**, **et al.** Defect-induced photoluminescence in monolayer semiconducting transition metal dichalcogenides. *ACS Nano*, 9(2), (2015) 1520–1527

[244] **Yagodkin, D.**, **Greben, K.**, **Eljarrat, A.**, **et al.** Extrinsic localized excitons in patterned 2d semiconductors. *Advanced Functional Materials*, 32(31), (2022) 2203060

[245] **Wanzenboeck, H.**, **Fischer, M.**, **Gottsbachner, J.**, **et al.** Focused electron beam induced deposition of silicon oxide. *ECS Meeting Abstracts*, Ma2005-02(19), (2006) 730–730

[246] **Gant, P.**, **Carrascoso, F.**, **Zhao, Q.**, **et al.** A system for the deterministic transfer of 2d materials under inert environmental conditions. *2D Materials*, 7(2), (2020) 025034

[247] **Huang, Y.**, **Pan, Y.H.**, **Yang, R.**, **et al.** Universal mechanical exfoliation of large-area 2d crystals. *Nature Communications*, 11(1), (2020) 2453

[248] **Graphenea**. Specifications from manufacturer homepage. `www.nanotechnik.com/mm3a-em.html`, Accessed: 2024-02-03

[249] **Liashenko, I.**, **Rosell-Llompart, J.**, & **Cabot, A.** Ultrafast 3d printing with submicrometer features using electrostatic jet deflection. *Nature Communications*, 11(1), (2020) 753

[250] **Haigh, S.J.**, **Gholinia, A.**, **Jalil, R.**, **et al.** Cross-sectional imaging of individual layers and buried interfaces of graphene-based heterostructures and superlattices. *Nature Materials*, 11(9), (2012) 764–767

[251] **Caplins, B.W.**, **Holm, J.D.**, & **Keller, R.R.** Orientation mapping of graphene in a scanning electron microscope. *Carbon*, 149, (2019) 400–406

DANKSAGUNG

An dieser Stelle möchte ich mich bei all denjenigen bedanken, die mir - vor allem im Rahmen meiner Dissertation - geholfen haben, neue Dinge zu lernen, mich weiter zu entwickeln und die Erfahrungen zu sammeln, die ich in dieser Zeit gemacht habe.

Zuerst gebührt mein aufrichtiger Dank Prof. Dr. Jannik Meyer für die Chance, meine Dissertation in seiner Gruppe anzufertigen und für seine hervorragende Betreuung. Die stetige Unterstützung und die einfallsreichen Lösungsansätze bei auftretenden Herausforderungen waren von unschätzbarem Wert während meiner Forschungsreise. Vielen Dank für die vielen Freiheiten und Möglichkeiten, meine eigenen Ideen umzusetzen.

Ebenso bedanken möchte ich mich bei Prof. Dr. Reinhold Kleiner für seine Bereitschaft, das Zweitgutachten dieser Arbeit zu übernehmen. Ein besonderes Dankeschön geht auch an Prof. Dr. Monika Fleischer für die Zweitbetreuung und Unterstützung während meiner Dissertation.

Außerdem möchte ich mich bei der kompletten Forschungsgruppe Advanced Materials für die gute Arbeitsatmosphäre und die vielen interessanten Gespräche und Diskussionen bedanken. Insbesondere danke ich Dr. Christoph Hofer für die Hilfe am TEM, Nils Rieger für die optischen Messungen im Rahmen seiner Masterarbeit sowie Kevin Strobel für den gewinnbringenden Ideenaustausch und sein Skript zur automatisierten Bildaufnahme am TEM.

Für die unkomplizierte Bereitstellung der TMD-Materialien danke ich Prof. Dr. Xiao Wang und Dr. Kai Braun, der auch für die optischen Messungen jederzeit zur Verfügung stand.

Mein Dank gebührt natürlich auch allen Kollegen am NanoZ. Ihr seid ein tolles Team und es war mir eine große Freude ein Teil davon gewesen zu sein. Vor allem Dr. Claus Burkhardt und Dr. Birgit Schröppel danke ich für die vielen, hilfreichen Gespräche und Tipps sowie jegliche Unterstützung, die Ihr mir nicht nur an den Mikroskopen gegeben habt.

Ein herzliches Dankeschön geht auch an alle anderen Kollegen am NMI, die mich so gut aufgenommen haben und unter denen ich so gute Freunde gefunden habe. Vielen Dank für die zahlreichen unvergesslichen Momente, die wir auch außerhalb der Arbeit erlebt haben.

Abschließend gebührt mein Dank meinen Freunden, meiner Familie und insbesondere Hannah. Ihr hattet immer ein offenes Ohr für meine Gedanken und Probleme und habt mir mit viel Liebe und Geduld geholfen, meine Ziele zu erreichen. Dafür bin ich Euch unendlich dankbar!